MIOCENE TO RECENT EVOLUTION OF THE CILICIA BASIN WITH EMPHASIS ON THE PLIOCENE-QUATERNARY SEDIMENTARY RELATIONSHIP BETWEEN THE GÖKSU RIVER AND THE CILICIA BASIN:

A Quantitative study of volumetrics, subsidence in the Cilicia Basin and concomitant uplift in the Mut basin, Taurus Mountains

SUSAN KENNEDY

MIOCENE TO RECENT EVOLUTION OF THE CILICIA BASIN WITH EMPHASIS ON THE PLIOCENE-QUATERNARY SEDIMENTARY RELATIONSHIP BETWEEN THE GÖKSU RIVER AND THE CILICIA BASIN:

A quantitative study of volumetrics, subsidence in the Cilicia Basin and concomitant uplift in the Mut basin, Taurus Mountains

by

Susan Kennedy

A thesis submitted to the

School of Graduate Studies

in partial fulfillment of the

requirements for the degree of

Master of Science

Department of Earth Sciences

Memorial University of Newfoundland and Labrador

September, 2012

St. John's Newfoundland and Labrador

TABLE OF CONTENTS

ACKNOWLEDGEMENTS

I would like to take this opportunity to extend my appreciation to those people who supported me during my graduate program. Without you this thesis would not have been possible.

My sincerest thank you goes to Drs. Ali Aksu and Jeremy Hall for their tireless efforts and guidance in my personal evolution and growth as a geophysicist. Dr. Ali Aksu, your dedication to your career and your students is unrivaled. Thank you for imparting some of your expertise in marine geology and for always being there to help. Dr. Hall, your knowledge of geophysical techniques, seismic data processing and rock physics has been invaluable. I have been very fortunate to have you both as supervisors.

Thank you to the faculty, staff and fellow graduate students of the Earth Sciences Department at Memorial University of Newfoundland. In particular, Dr. Jeremy Hall and Sharon Deemer for their help in navigating the world of seismic data processing and to Peter Bruce for his friendly banter and his technical support with Petrosys and Seisworks. Thank you to Dr. Rick Hiscott for helpful scientific discussions and advice on the sedimentological aspects of the thesis and to Dr. Cenk Yaltırık for providing the estimates of the volume of the Göksu gorge.

Thank you to the School of Graduate Studies and NSERC Discovery Grants for the financial support required for this thesis and to the Landmark Graphics Corporation for donating the seismic processing software used for data processing.

To the Officers and crew of the research vessel *K. Piri Reis* and our Turkish colleagues: without you the fieldwork would not have been possible. I will always remember with fondness my summer in Turkey with you.

I would like to say a very sincere thank you to my parents, who have supported my educational career from the start. Without your dedication I would not have gotten to this point in my life. In particular, a special thank you goes to my mother, who put in a few late nights to help with the compiling and printing of the thesis and to my father for his assistance in sizing the seismic reflection profiles included in the back panels. As well, thank you to my dear friends for their continued support and encouragement. Finally, I would like to thank my loving husband who has taken this journey with me - your continued encouragement, support and dedication have meant the world to me.

ABSTRACT

Mountain building occurs at convergent plate margins once oceanic lithosphere has been subducted and continental lithosphere from one plate collides with continental lithosphere from the other. Intermontane plateaux develop during orogenesis and their uplift is accompanied by erosion and the transport of sediments within the plateau and out beyond their margins into adjacent seas. The histories of uplift, erosion and deposition shed light on the geodynamic processes involved. The Central Anatolian Plateau results from the active collision of the African and Eurasian plates, with the Aegean-Anatolian microplate caught in between. An international research program is currently studying the uplift and erosion history of the plateau and surrounding mountains. The research in this thesis complements the terrestrial research with estimates of the sediment deposited from the plateau and adjacent Taurus Mountains into the 'sink' of the Cilicia Basin in the eastern Mediterranean. The research is based on the interpretation of seismic reflection profiles run across marine sediments that are contributed by the Göksu River — the main distributary at the southern side of the Taurus Mountains.

On the western shelf-edge of the Inner Cilicia Basin, immediately seaward of the Göksu River, the Pliocene-Quaternary sedimentary successions are composed of a number of stacked, prograded delta successions which overlie Messinian evaporites and pre-Miocene basement. The architecture of these deltas shows clear east- and south-east prograded clinoform reflections and this strongly suggests that they were sourced from the Göksu River. Further examination of seismic reflection profiles from the Cilicia Basin confirms the presence of additional vertically stacked and prograded delta packages with southwest-directed clinoform reflections along the northeastern edge of the basin, immediately seaward of the larger Seyhan, Ceyhan and Tarsus Rivers. The particular architecture of these packages strongly suggests a northern source. The main focus of this study has been to examine the nature of the sedimentary by-products of the Göksu River and the rates and modes of deposition through time, particularly during the Pliocene and Quaternary. Two chronostratigraphic boundaries are defined corresponding to dated horizons observed in exploration wells: (i) the M-reflector (defining the top of the Messinian i.e. 5.3 Ma) and (ii) the A-reflector (Early-Late Pliocene boundary i.e. 3.6 Ma). A third boundary, the P-reflector, occurs within the Quaternary successions and was also used in the analysis. The age of this boundary is tentatively assigned to be 1.9 Ma. The volumetrics of these three intervals (i.e. M- to A-reflector, A- to P-reflector and P-reflector to seabed) were calculated to determine the differential rates of sedimentation into the Cilicia Basin throughout the Pliocene-Quaternary. To conduct the analysis, the

sedimentary volumes were separated into contributions from the Göksu River in the west versus the Seyhan, Ceyhan and Tarsus Rivers to the north. The total resultant volume of sediment assumed to arrive into the Cilicia Basin during the Pliocene and Quaternary from the Göksu River was found to be ~6305 km^3, somewhat in excess of the volume of sediments eroded from the Göksu gorge of ~5789 km^3, i.e. 92% of the sediments are accounted for. The remainder must come from the Taurus Mountains and the Central Anatolian Plateau to the north. The volume of sediments contained in each interval was converted into an average sedimentation rate and compared with the present-day sedimentation rate of the Göksu River. The sedimentation rates of the three intervals were found to be: (i) 6.45 x 10^6 tonnes/yr for the interval bound by the M- and A-reflectors, (ii) 2.67 x 10^6 tonnes/yr for the interval bound by the A- and P-reflectors and (iii) 8.33 x 10^5 tonnes/yr for the interval bound by the P-reflector and the seabed. The present-day rate of sedimentation by the Göksu River is reported to be 2.16 x 10^6 tonnes/yr. These results show that sedimentation in the Early Pliocene interval was significantly greater than it is today, suggesting a more rapid period of uplift along the adjacent landmass, with sedimentation rates likely slowing in the Late-Pliocene-Quaternary as uplift rates fell.

The analysis of the sedimentary volumes arriving into the Cilicia Basin contained in each interval brought out two additional conclusions. Firstly, the temporal offset toward the southwest of the locus of progressively younger delta lobes known to be sourced by the Göksu River allowed for a conservative estimate of sinistral slip along the offshore component of the Kozan Fault Zone between 0.6-1.0 cm/yr. This fault is a splay of the sinistral East Anatolian Transform Fault that forms the eastern boundary of the Aegean-Anatolian Plate. There are no slip rate estimates available for the Kozan Fault onland; however, the slip rate estimated is compatible with estimates for the adjacent Ecemiş Fault Zone. Secondly, the buried topset-to-foreset transitions of the dated deltas allowed for some estimates of subsidence along the western shelf-edge of the Inner Cilicia Basin. Subsidence rates in this region were found to decrease from ~0.6-0.8 mm yr^{-1} in the Early Pliocene interval to ~0.10-0.20 mm yr^{-1} in the Late Pliocene-Quaternary interval. The subsidence is concomitant with the uplift of the plateau and Taurus Mountains and it is suggested that the subsidence results from the thrust load of the adjacent and thickened Taurus Mountains. The suggestion of others that the plateau uplift is caused by the collision of seamounts with the subduction zone south of Cyprus is incompatible with the observed subsidence of the Cilicia Basin in the Pliocene and Quaternary.

LIST OF FIGURES

LIST OF TABLES

CHAPTER 1: INTRODUCTION

Mountains generally form when two plates collide at convergent plate margins and the continental lithosphere of one plate is thrust over the continental lithosphere of the other (Moores and Twiss, 1995). In this process, intermontane plateaux may develop and their uplift is inevitably accompanied by erosion and transport of sediments from within the plateaux out into the adjacent seas. Through the study of the histories of uplift, erosion and deposition, a greater understanding can be found of the geodynamic processes involved. The Central Anatolian Plateau is a very large uplift structure that is the result of the present collision of the African and Eurasian Plates, with the Aegean-Anatolian Microplate caught in between (Şengör et al., 1985; Dewey et al., 1986); the Central Taurus Mountains comprise the southern margin of this massive uplift structure (Figure 1.1). This system is still in the early stages of collision, making it an ideal area to study the development of orogenic plateaux as the majority of its sedimentary record remains intact. Ten to fifteen million years of development are recorded in onland basins (Bassant et al., 2005; Eriş et al., 2005; Cosentino et al., 2012; Schildgen et al., 2012) and the complementary subsidence is recorded in offshore basins and in the deltas which are forming along the continental-oceanic margin (Aksu et al., 2005a, 2009; Hall et al., 2005a, 2009). The study of these prominent deltas should provide a stratigraphic record of uplift. The Vertical Anatolian Movements Project (VAMP) comprises an international research program that is currently studying the uplift and erosion history of the Central Anatolian Plateau and surrounding mountains (Cosentino et al., 2012 and Schildgen et al., 2012). The research in this thesis complements the terrestrial research of the 'source'

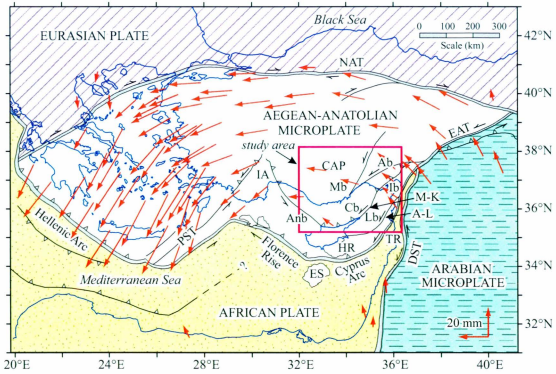

Figure 1.1 Simplified tectonic map of the eastern Mediterranean Sea showing major structural elements; complied from Şengör and Yılmaz (1981), Dewey et al. (1986) and ten Veen et al. (2004) (map is modified from Aksu et al., 2009). A-L = Amanos-Larnaka culmination, Ab= Adana Basin, AnB = Antalya Basin, Cb= Cilicia Basin, CAP = Central Anatolian Plateau, DST = Dead Sea Transform Fault, EAT = East Anatolian Transform Fault, ES = Eratosthenes Seamount, IA = Isparta Angle, Ib = Iskenderun Basin, Lb= Latakia Basin, M-K = Misis-Kyrenia lineament, Mb= Mut Basin, NAT = North Anatolian Transform Fault, PST = Pliny-Strabo Trenches, TR = Tartus Ridge and YF = Yumurtalık Fault. Sense of motion is indicated on major faults. GPS vectors from McClusky et al., 2000. The study area is outlined in pink.

by analyzing the processes of sedimentation from the adjacent Taurus Mountains into the 'sink' of the Cilicia Basin in the eastern Mediterranean Sea.

The focus of this thesis is on the processing and interpretation of high-resolution multichannel seismic reflection profiles that were collected in 2008 from the Cilicia Basin in the northeastern Mediterranean and run across marine sediments that are contributed by the Göksu River — the main distributary at the southern side of the Taurus Mountains. These data will be combined with previously collected seismic reflection data, with the scientific objectives of:

- delineating the Pliocene-Quaternary structural architecture of the Cilicia Basin, and its link to the development of the Central Taurus Mountains in the north and northwest and the Kyrenia Range and Misis Mountains in the south and east, respectively,

- determining the development and evolution of major basin-bounding fault systems and the partitioning of strain into extension, contraction and strike-slip during the Pliocene-Quaternary development of the Cilicia Basin,

- determining the relative importance of sea-level changes, variations in sediment supply and local tectonics in controlling the creation of accommodation space and the distribution and sequence stratigraphy of the Pliocene-Quaternary delta successions in the Cilicia Basin,

- determining the volume of sediment contained in various Pliocene-Quaternary delta sequences, and relating these estimates to variations in the rates of sediment

discharge from their sole source, the Göksu River, and rates of uplift and denudation of its drainage area in the Central Tauride Mountains, and

- determining the amount of basin subsidence that has occurred during the Pliocene-Quaternary and to make some broad statements about the variation of subsidence in various Pliocene-Quaternary sequences.

The following focuses on the key elements necessary for the understanding and discussion of the objectives stated above.

1.1 Present-day tectonic framework of the eastern Mediterranean

The present-day tectonic framework of the eastern Mediterranean Sea is controlled by the collision between the African and Eurasian Plates and the subsequent displacements of the smaller Arabian and Anatolian-Aegean Microplates (Şengör et al., 1985; Dewey et al., 1986; Fig. 1.1). The Aegean-Anatolian Microplate is currently moving west along the dextral North Anatolian Transform Fault and the sinistral East Anatolian Transform Fault. To the south in the eastern Mediterranean Sea, the Hellenic Arc, Pliny and Strabo Trenches define the zone of convergence between the African Plate and the Aegean-Anatolian Microplates in the west, and the Florence Rise, Cyprus Arc and the Tartus Ridge in the east (Şengör and Yılmaz, 1985; Robertson, 1998; Vidal et al. 2000a,b; Hall et al., 2005 a,b). These structures form two distinct, arcuate zones of deformation, which are the primary carriers of the strain resulting from this collision (Fig. 1.1). The regions of the Hellenic and Cyprus Arcs that are perpendicular to the relative motion of the African Plate and Aegean-Anatolian Microplate delineate subduction zones. The Pliny and Strabo Trenches and the Tartus Ridge trend sub-parallel to the slip

vector that defines the relative motion between these plates and mainly carry a transform motion. To the east, the boundary between the African Plate and the Arabian Microplate is delineated by the dextral Dead Sea-East Anatolian Transform Fault (e.g., Dewey and Şengör, 1979; Şengör et al., 1985, 2005; Fig. 1.1).

Recent studies have showed that subduction has ceased along the Florence Rise-Cyprus Arc, but is continuing along the Hellenic Arc (Woodside et al., 2002; Govers and Wortel, 2005). In this region, the relative motion between the African Plate and the Aegean-Anatolian Microplate has nearly come to a halt and the subduction of the African Plate along the Hellenic Arc is accompanied by slab roll-back (Govers and Wortel, 2005). In such land-locked basins the overriding plate shows back-arc extension in response to the movement of the trench, such as the north-south extension seen in the western segment of the Aegean-Anatolian Microplate (Robertson 1998). Another consequence of subduction along the Hellenic Arc and a lack of subduction along the Cyprus Arc is the tearing of the lithosphere along transform-parallel zones. The tearing transform segment along the present-day Pliny-Strabo Trenches is referred to as the Subduction-Transform Edge Propagator, or STEP fault (Fig. 1.1; Govers and Wortel, 2005).

The Florence Rise-Cyprus Arc-Tartus Ridge defines the eastern segment of the oblique convergent boundary between the African Plate and the Arabian and Aegean-Anatolian Microplates (Fig. 1.1). The arc initiated in the Late Cretaceous as an ophiolitic suture comprising the Hatay, Kızıldağ, Baër-Bassit, and Troodos complexes (Biju-Duval et al., 1978). Subsequent events in the Eocene and late Miocene shaped an arcuate fold-thrust belt with major culminations centered on re-imbricated elements of the ophiolitic suture (Yılmaz, 1993; Hall et al., 2005a,b). Presently, the east-trending southern segment

of the margin is characterized by contraction in a fore-arc setting, related to northward subduction of the African Plate with ensuing collision of the Eratosthenes Seamount (Fig. 1.1; Ben Avraham et al., 1995; Robertson, 1998). The northeast-trending eastern segment is in sinistral transtension along strands of the East Anatolian Transform Fault, facilitating the westward escape of the Anatolian microplate (Şengör et al., 1985; Kempler and Garfunkel, 1994). The Neogene Adana-Cilicia and Iskenderun-Latakia-Mesaoria Basin complexes are situated inboard of the Cyprus Arc and follow the arcuate trend of the African-Anatolian plate boundary (Fig. 1.1). During the Miocene, these basins developed as a broad foredeep south and east of the evolving Tauride thrust front. In the late Miocene, they became two separate parallel depocentres which evolved on the back limbs of two large thrust culminations (Fig. 1.1): the Misis–Kyrenia lineament in the north (Kelling et al., 1987; Aksu, 2005a) and the Amanos-Larnaka culmination in the south (Hall et al., 2005a,b).

Thus, the Cilicia Basin is situated north of this broad convergence zone, which delineates the boundary between the African Plate and the Aegean-Anatolian Microplate (Fig. 1.1). In fact, the zone of deformation associated with the convergence is very wide, extending from the Florence Rise-Cyprus Arc-Tartus Ridge approximately 300 km toward the north (e.g., Hall et al., 2005a,b; Calon et al., 2005a,b; Aksu et al., 2005a,b). This broad deformation zone is characterized by three prominent south-convex arcuate zones, which parallel the trend of the Florence Rise-Cyprus Arc-Tartus Ridge: the Amanos-Larnaka zone, the Misis-Kyrenia zone and the Central Taurus Mountains (Fig. 1.1). Within this backdrop, the Cilicia Basin and its onland segment, the Adana Basin,

emerge as an arcuate intermontane depocentre nestled between the Misis-Kyrenia orogen in the south and southeast and the Taurus orogen in the northwest.

1.2 Bathymetry of the northeastern Mediterranean Sea

In the northeastern Mediterranean Sea, the seafloor morphology is largely controlled by (i) large-scale tectonic features, such as the Misis–Kyrenia zone, the Florence Rise, the Cyprus Arc, and (ii) by sediment input from the major rivers that flow into the region (Fig. 1.2). In the Cilicia Basin, the continental shelf is generally less than 5 km wide, except to the north where it widens considerably to over 45 km off the mouths of present-day deltas (Aksu et al., 2005a; Fig. 1.2). The major bathymetric feature in the study area is the Misis-Kyrenia fold/thrust belt, which defines a NE–SW trending zone of deformation with relatively shallow water depths that can be traced from the northeastern tip of Cyprus toward the Misis Mountains of southern Turkey. This zone creates a physiographic divide between the Cilicia Basin in the northwest from the Latakia Basin in the southeast (Fig. 1.2). The shelf-slope break generally occurs at ~125 m water depth and steeper slopes lead toward the deeper basin floor (Aksu et al., 2005a). The water depth gradually increases from the Inner to the Outer Cilicia Basin, reaching depths over 1000 m in the central Outer Cilicia Basin. The Cilicia Basin is separated from the Antalya Basin by a broadly arcuate zone which extends from the northwestern tip of Cyprus toward mainland Turkey, referred to as the Anamur-Kormakiti zone (Fig. 1.2). West of the Anamur-Kormakiti zone, the water depth sharply increases to ~2500 m into the Antalya Basin (Fig. 1.2).

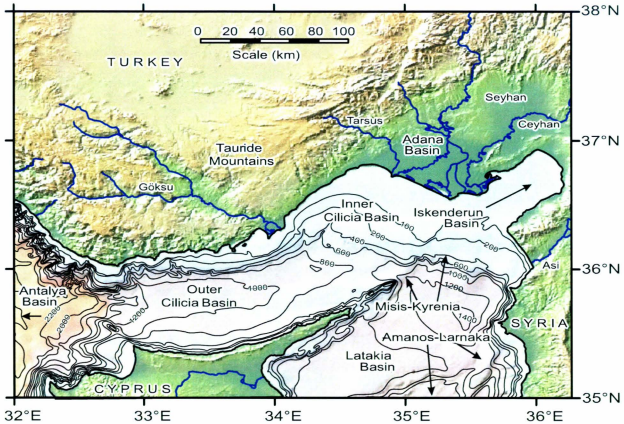

Figure 1.2 Detailed bathymetry of the Cilicia Basin and environs, compiled using the echo sounder data collected during R/V Piri Reis cruises 1991 and 1992, and the International Bathymetric Chart of the Mediterranean (Intergovernmental Oceanographic Commission, 1981). Also shown are major bathymetric features and the Göksu, Seyhan, Ceyhan Tarsus and Asi Rivers.

1.3 Marine Miocene basins in the northeastern Mediterranean

In southern Turkey, there are several predominantly marine Miocene basins that are presently perched on the Central and Western Tauride Mountains, such as the Kasaba, Aksu, Köprüçay, Manavgat, Mut, Ecemiş and Adana Basins (Fig. 1.3). In these basins, the Early-Late Miocene deposits unconformably overlie Cretaceous to Oligocene basement rocks (Burton-Ferguson et al., 2005; Monod et al., 2006). This depositional architecture suggests that the basement was exhumed and eroding prior to the Miocene transgression (Eriş et al., 2005). In the Mut, Ecemiş and Adana Basins, the first marine inundation is dated as Early Miocene (Ilgar and Nemec, 2005; Eriş et al., 2005; Bassant et al., 2005). Sediments occupying the paleo-river valleys also date as Early Miocene in the Mut Basin (Eriş et al., 2005), Adana Basin (Ocakoğlu et al., 2002) and the Aksu, Köprüçay, and Manavgat Basins (Deynoux et al., 2005; Karabıyıkoğlu et al., 2005). In the offshore, immediately south of the Central and Western Taurus Mountains, there are several deep basins (e.g., Rhodes, Finike, Antalya, Cilicia, Iskenderun Basins), which contain significant thicknesses of Miocene deposits, in addition to near-complete Pliocene-Quaternary successions (Aksu et al., 2005a,b; Bridge et al., 2005; Işler et al., 2005; Hall et al., 2005a,b). These offshore basins often are directly paired with an onshore basin, only separated by the narrow continental shelf and the adjacent steep continental slope, such as the onland Kasaba Basin and its offshore continuation into Finike Basin, or the onland Mut and Adana Basins and their offshore continuations into the Cilicia and Iskenderun Basins (Fig. 1.3).

The evolution of the Miocene basins in the eastern Mediterranean is controlled by the development of a large, nearly east-west-trending foredeep in front of the Tauride

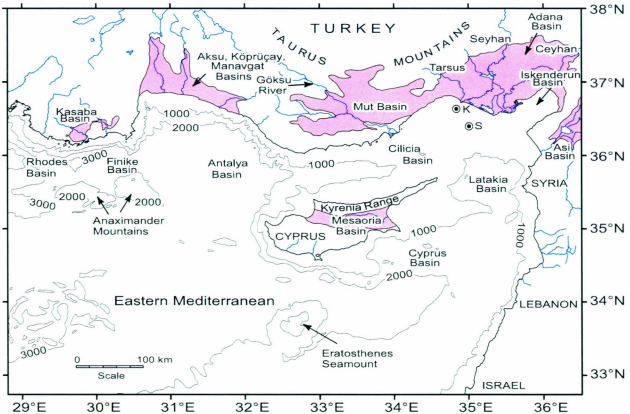

Figure 1.3 Index map of the eastern Mediterranean showing the locations of marine Miocene basins onland as well as their conjugate marine basins in the eastern Mediterranean Sea. Also shown is the present-day Göksu River in Cilicia Basin. Isobaths from the International Bathymetric Charts of the Mediterranean. Exploration wells used for this study, Karatas-1 (K) and Seyhan-1 (S) are marked by bulls-eyes.

fold-thrust belt (Williams et al., 1995). The Tauride culmination was characterized by an arcuate thrust front that delineated a broad syntaxis, comprising several smaller thrust culminations which developed in the foredeep itself. Recent studies in the Antalya Basin (e.g., Heather King, unpublished work) suggest that the base of the present-day continental slope is the expression of the northern trailing thrust that carries the Taurus Mountains, whereas the Misis-Kyrenia fault-thrust belt is the leading thrust that carries the Kyrenia Mountains of Cyprus (Calon et al., 2005a,b). There are very similar marine Aquitanian-Tortonian successions in the Mut and Adana Basins (Şafak et al., 2005; Eriş et al., 2005), in the fold-thrust panels in the Misis Mountains (i.e., proto-Misis Basin; Gökçen et al., 1988) and in the Kyrenia Range (i.e., proto-Kyrenia Basin; Calon et al., 2005a,b), in the Cilicia and Iskenderun Basins (Uffenorde et al., 1990) and in the Mesaoria Basin of Cyprus (Robertson and Woodcock, 1986). These similarities suggest that during the Early Miocene there was a single large basin that encompassed what are now seemingly isolated basins in the eastern Mediterranean (Fig. 1.4). This large ancestral foredeep basin probably extended into the Karsantı and Maraş Basins in the east (Hall et al., 2005a; Calon et al. 2005a) and the Antalya Basin in the west (Işler et al., 2005). The development of northern and southern crustal-scale thrust culminations, together with onset of escape tectonics associated with the final collision of the Arabian Microplate with the Aegean-Anatolian Microplate in the latest Miocene and Pliocene-Quaternary (Şengör et al., 1985) essentially split the foredeep into several large piggy-back basins: the Mut-Adana-Cilicia Basin Complex and the Iskenderun-Latakia-Mesaoria Basin Complex (Hall et al., 2005a; Calon et al., 2005 a).

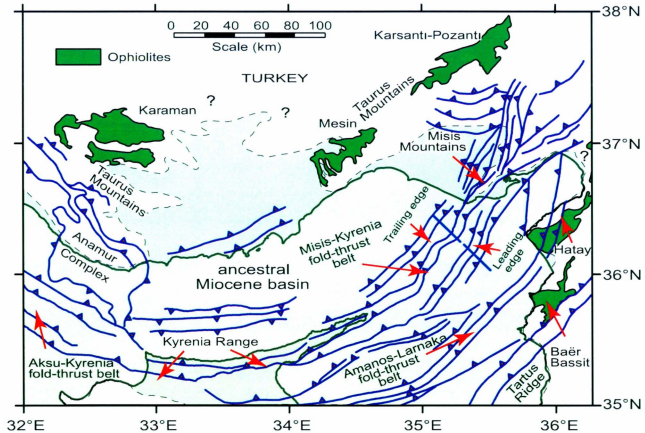

Figure 1.4 Map showing the approximate position of the ancestral basin that occupied the northeastern Mediterranean during the Early-Middle Miocene. The Miocene structures are from Aksu et al. (2005), Hall et al. (2005) and Aksu and Hall unpublished maps. The Miocene shoreline is compiled from Robertson and Woodcock (1986), Williams et al. (1995), Bassant et al. (2005), Eriş et al. (2005), Şafak et al. (2005). Also shown are the major ophiolite successions.

An examination of the elevation of various Miocene successions within the onland-offshore linked basins shows that correlative shallow-marine units are routinely vertically separated by 3000 – 5000 m across short distances of 5-10 km. There must have been primary seabed gradients within these basins, so that some of the observed vertical stratigraphic offset can be attributed to variations in the water depth in the ancestral Miocene basin. However, a significant proportion of this large offset must be the result of rapid subsidence in the offshore basins coupled with dramatic tectonic uplift of the onshore basins associated with the rise of the Taurus Mountains (Satur et al., 2005; Eriş et al., 2005; Karabıyıkoğlu et al., 2005; Schildgen et al., 2011; Cosentino et al., 2012).

1.4 The study area: Source to Sink

The onland Mut Basin is a predominantly marine Miocene depocentre, presently perched over the Central Taurus Mountains at elevations between 1000 and 3000 m (Ilgar and Nemec, 2005; Eriş et al., 2005; Bassant et al., 2005). The offshore Cilicia Basin also contains significant thicknesses of Miocene deposits, which are presently situated at ~2000 to 4000 m below sea-level (Aksu et al. 2005a, 2009). Thus, the Miocene successions within the onland-offshore linked basins show that correlative shallow-marine units are vertically separated by 3000 - 5000 m across short distances of 5-10 km. While some of this elevation can be explained by the seabed gradients within these basins, there still remains a significant proportion of this large offset that must be explained by the result of rapid subsidence in the offshore basins coupled with dramatic tectonic uplift of the onshore basins associated with the rise of the Taurus Mountains. This is further elaborated in Chapters 6 and 7.

The Göksu River cuts a deep canyon across the Central Taurus Mountains and drains through the onland Mut Basin to construct a large delta within the Inner Cilicia Basin (Fig. 1.2). Therefore, the study area provides a unique opportunity to carry out a detailed study of a source to sink relationship. In the Cilicia Basin, the amount and rate of basin subsidence can be calculated provided that the elevation of relative sea-level during the deposition of various sedimentary units can be determined and a secure chronostratigraphic framework can be established for the seismic sequences. The rate of Late Miocene to Recent erosion and denudation of the Mut Basin can also be estimated provided that the volume of sediment contained within successive delta lobes deposited in the Cilicia Basin by the Göksu River during the Pliocene-Quaternary can be accurately determined. The topset-to-foreset transitions in seismic reflection profiles provide the elevation of relative sea-level. The tight grid of high-resolution seismic profiles allows the mapping of temporal and spatial variations of various delta lobes; the resolution of existing industry lines is far too low for this purpose. The chronology of the seismic sequences is established using biostratigraphic data from two offshore exploration wells (Turkish Petroleum Corporation, unpublished data). Both wells penetrated the entire Pliocene-Quaternary succession (~2100 m), encountered the Messinian unconformity and tested an additional ~2000 m of upper-middle Miocene strata, terminating within Middle Miocene sediments at 4053 m in the Seyhan-1 well and 4142 m in the Karataş-1 well. Sedimentological and geochemical data (Schildgen et al., 2011; Cosentino et al., 2012) provide a much needed anchoring point for the successions observed in the Mut Basin so that orogeneic evolution of the Taurus Mountains and the adjacent depocentres can be clearly developed. These are further discussed in Chapters 6 and 7.

CHAPTER 2: METHODS

In this thesis, high-resolution multichannel seismic reflection data are used to investigate the geohistory of the Cilicia Basin, with special emphasis on the structural development of the Inner Cilicia Basin and the analysis of the sedimentary by-products of the Göksu River contained within various delta sequences. The following discussion will: (i) describe the seismic reflection method, (ii) outline the survey acquisition parameters for the data used in this study, (iii) give an overview of seismic reflection data processing methods and (iv) describe the methods used to carry out the interpretation of the seismic reflection profiles.

2.1 A brief overview of the seismic reflection method

The seismic reflection method is a remote-imaging technique that is commonly used to estimate the geological properties of subsurface rock bodies. Seismic reflection data are used to extend interpretations of subsurface lithologies out from regions where borehole data are available. Information is derived from the seismic reflection data using known relationships that involve wave propagation across boundaries (Sheriff and Geldart, 1995). The principal relationship, the Law of Reflection, states that when a seismic wave is incident on the interface of two stratigraphic boundaries (or strata) some of its energy is reflected on the first layer and some is transmitted through the second layer. The degree to which a stratigraphic layer reflects energy is a piece of information that when combined with other data can be used to estimate the geological properties of that stratum.

Sedimentary strata differ not only in rock type but also in geophysical parameters such as bulk density and seismic velocity (Gadallah and Fisher, 2005). For the simplest case of normal incidence (which is commonly assumed in reflection surveys) the amplitude of the reflected wave is determined by its reflection coefficient, R (see Equations 2.1 and 2.2).

$$R_{12} = \rho_2 v_2 - \rho_1 v_1 / \rho_2 v_2 + \rho_1 v_1 \qquad \text{Eqn. 2.1}$$

where: $\rho_{1,2}$ = Bulk density of layers 1 and 2,

$v_{1,2}$ = P-wave velocities of layers 1 and 2.

Equation 2.1 can also be written in terms of acoustic impedance, Z:

$$R_{12} = Z_2 - Z_1 / Z_2 + Z_1, \qquad \text{Eqn. 2.2}$$

where: $Z = \rho v$ Eqn. 2.3

Seismologists commonly speak of a reflection in terms of its acoustic impedance contrast (Z). Acoustic impedance is simply the product of the bulk density (ρ) and seismic velocity (v) in a layer (see Eqn. 2.3). Equation 2.2 states that the reflected amplitude varies with the incident amplitude directly with the change in acoustic impedance between strata. In other words, the stronger the contrast in acoustic impedance between layers, the stronger the observed reflection will appear on the seismogram (Sheriff and Geldart, 1995). For example, the impedance contrast between the water column and the seabed is high mainly because water and sediment have significantly different densities. The result is a high-amplitude seabed reflection observed on seismic reflection profiles. Another example relating to the study area is the

boundary between the Miocene evaporite package and the Pliocene-Quaternary sediment package, which is often seen on seismic reflection profiles as a prominent reflecting surface (locally known as the "M-reflector", Ryan, 1969; see Chapter 4). The difference in acoustic impedance between these two layers is high because the difference in seismic velocity between the lowermost sediments and the halite-containing evaporites can be upwards of ~2000 m/s. On the other hand, contrasts in acoustic impedance within clastic formations (eg. sandstone-shale) may be quite small, perhaps a few percent at most.

2.1.1 Seismic surveying

In order to extract seismic information from the Earth there must be a way to capture and record the seismic energy that is reflected upwards to the surface. A typical seismic reflection survey requires three pieces of equipment: (i) a source to generate the seismic waves (e.g. dynamite, air gun, Vibroseis etc.), (ii) receivers to detect the upcoming seismic waves and convert them to electrical signals (e.g. geophone array for land surveys or hydrophone array for marine surveys) and (iii) a seismograph to record the amplitude and traveltime from source to receivers of the reflections (Gadallah and Fisher, 2005). Additionally, a digitizer is included in most modern surveys to convert the analog signal to a digital signal, which is necessary for all software-related processing procedures (Yılmaz, 2001). A schematic of a typical 2D marine seismic reflection survey is shown in Figure 2.1.

The simplest example of a seismic reflection experiment is one where the source and receiver are placed at the same location (i.e. zero offset/normal incidence). In this experiment, the resultant data are a convolution of: the seismic wavelet (including the

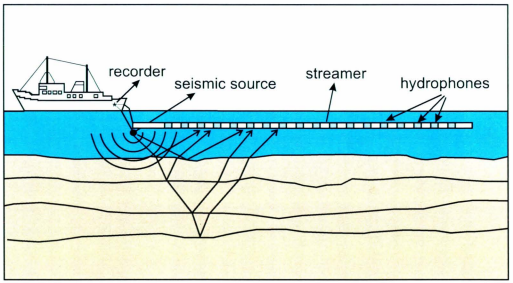

Figure 2.1 A generic 2D marine seismic reflection survey highlighting the key pieces of equipment: the seismic source, the streamer carrying the hydrophones, and the recording system (modified from Cranshaw, 2011).

source signature, the recording filter, the receiver-array response, etc.), the Earth's impulse response and any noise that may be present. The Earth's impulse response is comprised of primary reflections arising from the Earth's reflectivity series, as well as multiple reflections (Yılmaz, 2001). Because the seismic energy must travel down into the earth and then back up the receivers, the resulting seismogram is represented as a time series of amplitude versus two-way traveltime, commonly known as a "wiggle trace". In practice, the zero offset/normal incidence configuration does not produce strong enough data, so multiple receivers are laid out at variable short offsets from the source. In this configuration each shot produces a time-space (t-x) seismogram (Fig. 2.2), which includes various arrivals – direct waves, reflections and refractions. The reflections have a hyperbolic shape on the t-x plot (Fig. 2.2) that is tilted where the horizons dip. The reflector t-x function is constrained by (i) the seismic velocity of the material through which the wave propagates, (ii) the depth to the reflector, (iii) the dip of the reflector and (iv) the source-to-receiver distance (Yılmaz, 2001).

Seismic energy is also subject to various forms of attenuation and scattering that decrease the overall amplitude of the received signal. Therefore, it is necessary to optimize signal to noise ratio in the survey design. The most commonly used method is known as the "common midpoint acquisition method". In this survey method multiple shot and receiver pairs image the same location in the subsurface. This is achieved by moving the spread (source plus receivers) less than one-half the spread length between shots, resulting in an overlap of subsurface coverage (see Fig. 2.3). The common midpoint acquisition method ensures there is redundancy in the data, thereby increasing the signal to noise ratio (Gadallah and Fisher, 2005). The degree of redundancy is known

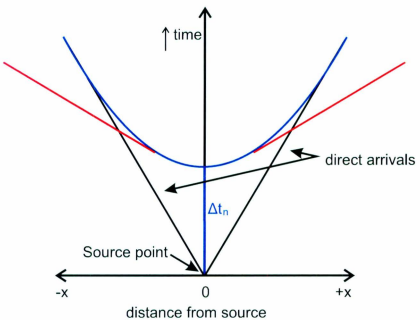

Figure 2.2 Schematic of the hyperbolic shape produced by a reflecting surface in the seismic reflection experiment on the t-x plot (reflection shown in blue). The red lines are the refractions and the direct arrivals are identified.

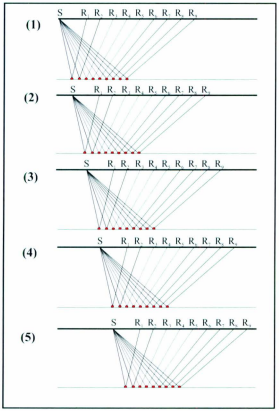

Fig. 2.3 Common-mid-point (CMP) seismic acquisition configuration; spread (i.e. source plus receivers) moves to the right with each consecutive shot 1-5 resulting in multiple subsurface coverage (from Işler, 2005).

as fold and is calculated as follows, for a shot taken at each receiver point, (i.e. shot interval = group interval):

Fold = ½ (number of channels [receiver spacing / shot interval]) Eqn. 2.4

2.2 Eastern Mediterranean Data Acquisition

The primary data used for this thesis are ~700 km of multi-channel 2D seismic reflection profiles acquired during the 2008 Eastern Mediterranean Sea Project survey. Memorial University of Newfoundland (MUN), in partnership with the Institute of Marine Sciences and Technology (IMST), Dokuz Eylül University, Izmir, Turkey, collected the data onboard IMST's research vessel, *K. Piri Reis*. The 2008 profiles were collected fanning outward from the mouth of the Göksu River (Fig. 2.4) to emphasize the desire to delineate the growth history of the Göksu delta (Hall, 2008). The survey connects to two exploration wells located on the eastern margin of the Inner Cilicia Basin. Two longer tie lines intersect the rest of the profiles (see Fig. 2.4). Older seismic data used as tie lines for interpretation include: profiles from two earlier cruises of the Eastern Mediterranean Sea Project in 1991 (12-fold) and 1992 (3-fold). Deeper penetration industry seismic reflection profiles and data from two exploration wells were provided by the Turkish Petroleum Corporation (Fig. 2.4).

2.2.1 Equipment

The source, provided by MUN, consisted of a broad-band, high frequency airgun array. The seven sleeve guns employed included: 4 x 40 in^3 (4 x 655 cm^3), 1 x 20 in^3 (1 x 328 cm^3) and 2 x 10 in^3 (2 x 164 cm^3) airguns, with two of the 40 in^3 guns hung in close

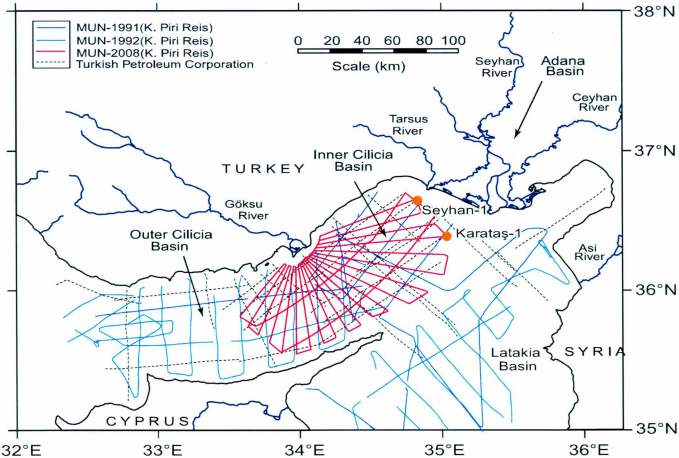

Figure 2.4 Map showing the positions of the multi-channel seismic reflection profiles collected from the Cilicia Basin. Seyhan and Karataş are exploration wells used for chronostratigraphy (see Chapter 4).

proximity so that when fired their bubbles would coalesce to simulate a single 80 in^3 gun. The total source volume when all guns were firing correctly was 200 in^3 (3277 cm^3). Shots were fired automatically on fixed time intervals using a trigger pulse system. The survey plan was to engage the source every 25 m by maintaining a constant ship speed and sending out a trigger pulse on fixed time intervals. Reflections were detected on IMST's 96 x 6.25 m channel Hydroscience Technologies Inc., high resolution, fluid-filled digital streamer. The streamer was towed at a constant depth of 3 m using nine Digi-Course depth controllers spaced at 75 m intervals. Its position with respect to the sail line azimuth was monitored visually (by tail buoy with strobe light) and by radar. The resultant data was digitally recorded for 7 seconds at 1 millisecond sample rate, using a SeaMUX NTRS-2 seismograph with the output recorded on the SeaMUX hard disk. IMST's SeaStar 4000 GPS receiver and EIVA NaviPac software were used to digitally record the navigation data. The incoming data were saved in standard SEG-Y file format (see EMED Phase IV Cruise Report, 2008). A flow chart describing the 2008 cruise set-up is illustrated in Figure 2.5.

2.1.2 Acquisition parameters and geometry

During the 2008 eastern Mediterranean survey, shots were fired every 25 m based on fixed time intervals that assumed a constant ship speed of 5.5 knots. The airgun array was towed a distance of ~77 m from the ship's stern and maintained a depth of 3 m by four 36 in-diameter flotation buoys. Upcoming reflections were detected on all 96 channels of the hydrophone streamer, which had a receiver spacing (or group interval) of 6.25 m. This survey geometry produced a maximum fold of 12 (Fig. 2.6).

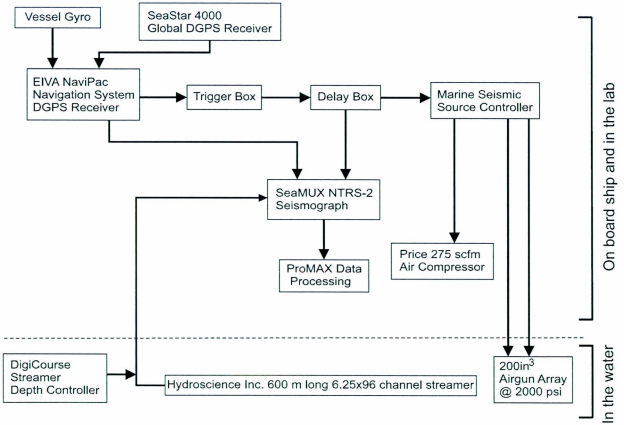

Figure 2.5 Flow chart illustrating the cruise set up for the 2008 eastern Mediterranean seismic survey. Modified from Cranshaw, 2010.

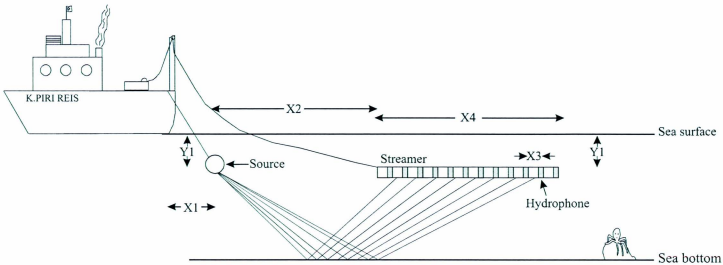

Fig. 2.6 The shooting geometry for 2008. Modified from Işler, 2005.
(X1) = stern to source distance, 77 m; (X2) = source to centre of first hydrophone group, 70 m; (X3) = hydrophone group interval, 6.25 m; (X4) = active streamer length, 600 m; (Y1) = source and streamer depth, 3 m.

2.3 Seismic Data Processing

The seismic data recorded by the receivers are not only composed of primary reflections resulting from Earth's reflectivity series, but also of data from coherent and ambient noise sources. Therefore, signals and noise are superimposed on the seismogram. The goal of seismic data processing is to separate signal from noise, thereby enhancing the signal to noise ratio, to produce an image that is truest to the Earth's subsurface (Yılmaz, 2001). To achieve this, the raw seismic shot gathers are processed digitally. Processing artifacts can be generated from inappropriate parameter choice, so the individual processing the data must be capable of determining the appropriate parameters and evaluating the output of the algorithm. A generic 2D marine seismic reflection data processing flow is outlined in Figure 2.7 and the various steps are explained in the following subsections.

2.3.1 Analysis of shot records

Firstly, the seismic record must be analyzed in its raw form to become familiar with frequency content and amplitude variations. Shots may have variations in these properties depending on the nature of the recording at that particular shot point. Coherent noise sources (such as the direct wave or multiple reflections) or ambient noise sources (such as monofrequency signals resulting from electrical interference) may present problems later in the flow. This stage allows the data processer to determine learn about the data's signal to noise ratio, amplitude losses and the presence of coherent/ambient noise in the record. Some selected raw common shot gathers from a marine survey are shown in Figure 2.8.

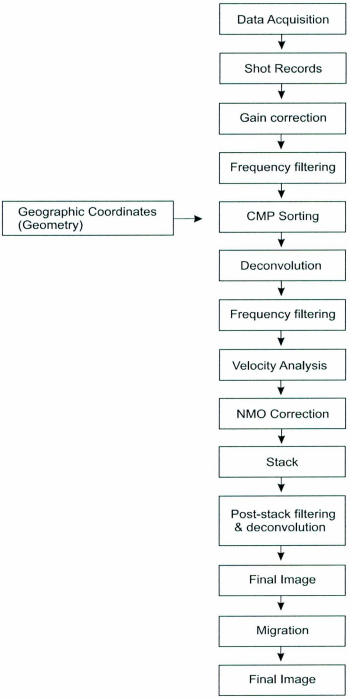

Figure 2.7 Generic 2D marine seismic reflection processing flow.

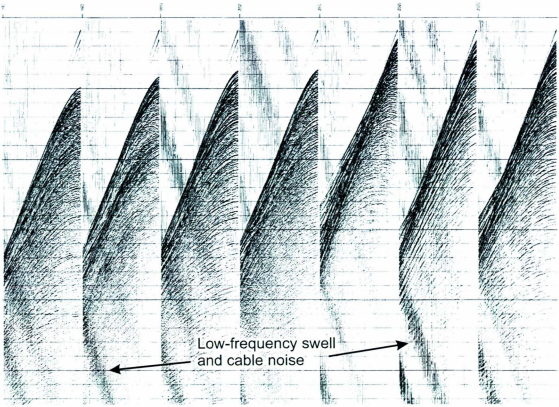

Figure 2.8 Selected raw marine seismic shot records. Note the noisy character, including the low-frequency swell and cable noise appearing as coherent streaks at later times in the record (from Yılmaz, 2001).

2.3.2 Frequency filtering

After the data has been inspected, a frequency filter may be applied to attenuate noise in the record so that a clearer picture may emerge. An unfiltered shot record can be so heavily laden with noise that primary reflections are totally obscured. In particular, marine data are often contaminated with a low-frequency, high-amplitude signal caused by swell and cable noise, as shown in Figure 2.8 (Yılmaz, 2001). Applying a frequency filter will help to uncover the primary reflections and allow the processer to get a better picture of other problems he/she may have to address further into the processing flow. Figure 2.9 shows the same common shot gathers as in Figure 2.8 but this time with a low-cut bandpass filter applied.

2.3.3 Gain applications

As the wavefront travels through the Earth it is subject to various effects that result in attenuation of seismic energy. A gain function is a type of time-variant scaling that is applied to the dataset to correct for these effects. The wavefront spherically propagates from the source point through the Earth, so, as it travels some of its energy is lost due to geometrical spreading. In a homogeneous medium the energy density of the wavefront decays proportionately to $1/r^2$, where r is the radius of the wavefront. Wave amplitude is proportional to the square root of energy density, thus amplitude decays as 1/r. Because velocity generally increases with depth, the wavefront will display even further divergence and amplitudes will decay even more rapidly with increasing depth (Yılmaz, 2001).

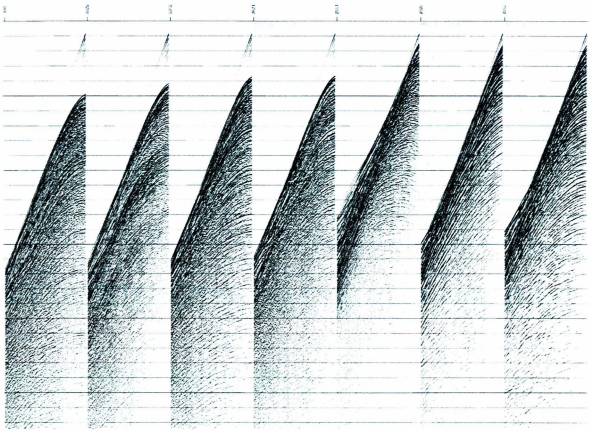

Figure 2.9 The same selected marine shot records as shown in Figure 2.8, with a frequency bandpass filter applied. The low-frequency streaks are gone and the variation of amplitude with time is more obvious (from Yılmaz, 2001).

Rocks are not perfect elastic carriers, so some of the received signal is also lost to anelastic attenuation. This attenuation effect of the Earth is frequency-dependent and causes the frequency content of the source wavelet to change in a time-variant manner as it propagates. As a result high frequencies are absorbed more rapidly than low frequencies, causing high frequencies to be concentrated at shorter traveltimes. This can be particularly damaging in areas containing soft fluid-filled sediments, typical of sedimentary basins (Yılmaz, 2001). A gain function can be applied to the seismic data to correct for these effects so that amplitudes are balanced throughout the seismic reflection profile. Figure 2.10 shows the same common shot gather as Figs. 2.8-2.9 with a geometric spreading correction applied, illustrating the importance of equalizing amplitudes for viewing later events.

For display purposes an automatic gain control (AGC) function can be applied to the dataset to bring up weak signals later in the profile. The AGC function operates by subdividing the input trace by specified time gates and averaging the root-mean-square (RMS) amplitude over those gates. The averaging algorithm moves down through the time gates in a sliding window to balance amplitudes all down the section. AGC tends to be used only for display purposes because applying it permanently in the flow can irrecoverably destroy signal character (Yılmaz, 2001).

2.3.4 Common midpoint (CMP) sorting

When the CMP shooting technique is employed in data acquisition, multiple source and receiver pairs image the same location in the subsurface more than once (see Fig. 2.3). While seismic recording is conducted in shot-receiver coordinates, most data

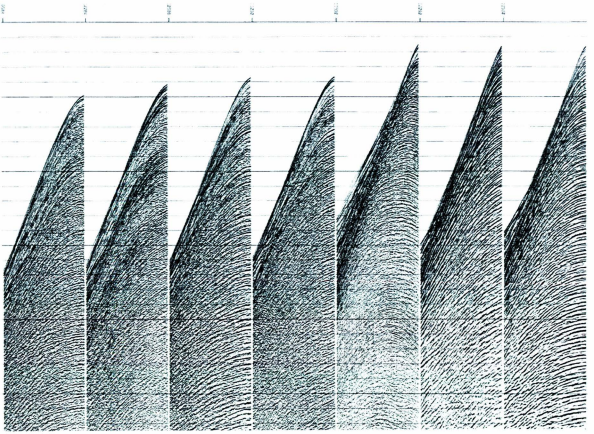

Figure 2.10 The same selected shot gathers as shown in Figs. 2.8 and 2.9 with a wavefront divergence correction applied. The amplitudes are now restored at later times in the section (from Yılmaz, 2001).

processing occurs in midpoint-offset coordinates (Yılmaz, 2001). The coordinate transformation is achieved by sorting the data into common midpoint (CMP) gathers. CMP sorting involves assigning each individual trace to the midpoint between the shot and receiver locations associated with that trace, based on the field geometry. Sorting the traces in terms of a common midpoint for a source and receiver pair allows the program to group all traces that have the same midpoint to one CMP gather. The number of traces in the CMP gather corresponds to the fold of the dataset (see Eqn. 2.4). CMP sorting can be problematic in the case of dipping reflectors because reflection points do not lie below the corresponding CMP (Fig. 2.11). This can result in smearing of data in midpoint-offset coordinates.

2.3.5 Deconvolution

As previously stated, the seismic trace recorded by the receivers is a convolution of the seismic wavelet with the Earth's impulse response. The purpose of deconvolution, ideally, is to remove the source-time function from the recorded seismogram leaving only the Earth's reflectivity series, thereby compressing the seismic wavelet so that it approximates a unit impulse function. Compressing the wavelet can attenuate reverberations and short-period ("peg-leg") multiples, which in turn will increase temporal resolution in the profile (Yılmaz, 2001). Wavelet compression is achieved by using an inverse filter containing the source waveform as the deconvolution operator. When the inverse filter is applied to the entire seismogram, it should yield the Earth's impulse response. The main assumptions underlying the deconvolution process are that: the Earth is composed of horizontal layers of constant velocity, the seismic source generates a compressional wave that strikes the Earth at normal incidence, the source

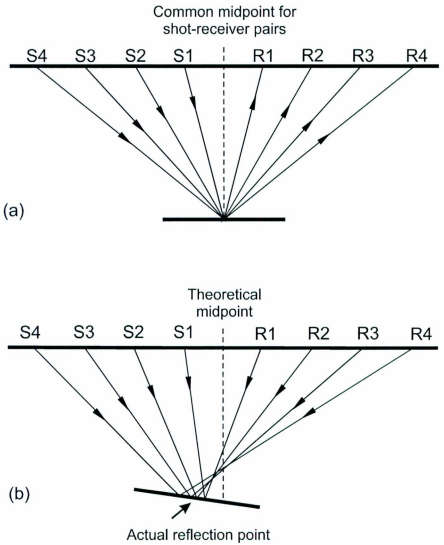

Figure 2.11 (a) For a horizontal surface, shot and receiver pairs image the same location in the subsurface using the "common midpoint shooting technique", (b) for a dipping horizon, the midpoint is chosen as its theoretical counterpart assuming the reflector was horizontal. The actual midpoint location is updip from the chosen theoretical midpoint. This results in "CMP smearing".

waveform is stationary (i.e. does not change as it travels through the subsurface), there is no noise present in the seismic record and the source waveform is known. When any of these assumptions fail, deconvolution will not be fully successful. It is important to note that if the source waveform were known then the deconvolution process could be deterministic with a simple solution. Because this is often not the case, deconvolution must be applied to the data iteratively to determine the appropriate parameters required to obtain the best possible outcome, and no method is perfect – especially in the presence of noise. The two main types of deconvolution operators that are commonly applied to seismic reflection data are: spiking deconvolution and predictive deconvolution. Spiking deconvolution will ideally convert a reflection wavelet to a zero-lag spike to increase temporal resolution, whereas predictive deconvolution exploits the periodicity of multiples to predict their arrival times and remove them. Both of these operators require minimum phase data (Yılmaz, 2001). Figure 2.12 displays a series of shot gathers before and after deconvolution.

2.3.6 Normal moveout correction and velocity analysis

The next stage in conventional seismic reflection data processing is to correct the CMP gathers for moveout. Similarly to the shot gather, the traveltime curve for a CMP gather as a function of offset is hyperbolic, under some common assumptions. The difference in traveltime between a given offset and zero offset is known as "normal moveout", or NMO. It is necessary that reflection events in the CMP gathers be corrected for their moveout so that all offsets occur at the same traveltime for later stacking of the CMP gathers into a single trace (Fig. 2.13). The traveltime equation for a single horizontal layer as a function of offset is found using the Pythagorean Theorem:

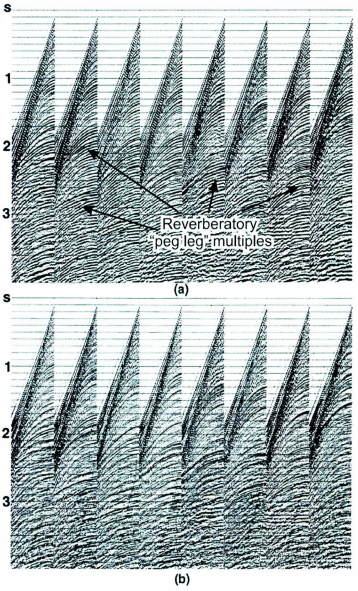

Figure 2.12 Marine shot gathers (a) before and (b) after deconvolution. Prominent reflectors are more clearly visible after deconvolution because shallow reverberations have been attenuated (from Yılmaz, 2001).

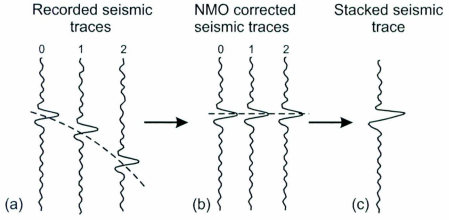

Figure 2.13 Schematic of (a) a series of recorded seismic traces displaying the hyperbolic trajectory of a reflection, (b) the same traces corrected for normal moveout (NMO) and (c) the stacked version of these traces summed together to produce an enhanced reflection. Note that arriving time increases downwards along each trace.

$$t^2 = t_0^2 + x^2 / v^2 \qquad \text{Eqn. 2.5}$$

where: x = offset (distance from source to receiver)

v = velocity above the reflecting interface

t_0 = two-way zero offset time, and

t = the traveltime for the raypath.

Given that the offset, x, and two-way traveltimes t_0 and t are known, velocity can be computed. The NMO correction is given by the difference in t_0 and t:

$$\Delta t_{NMO} = t - t_0 \qquad \text{Eqn. 2.6}$$

Or alternatively, using Equation 2.5 the NMO correction is given as:

$$\Delta t_{NMO} = t_0 \left[(1 + (x / v_{NMO}\, t_0))^{0.5} - 1\right] \qquad \text{Eqn. 2.7}$$

Therefore, correcting the data for NMO requires an estimate of the seismic velocity at a particular reflection point. The velocity required to correct for NMO is known as the NMO velocity, or v_{NMO}. In the case of a single horizontal reflector v_{NMO} is equal to the velocity of the medium above the reflector. For a single dipping reflector v_{NMO} is equal to the velocity of the medium above the reflector divided by the cosine of the dip angle (Yılmaz, 2001). For a variable velocity case, v_{NMO} is the RMS velocity with respect to time. The interval velocity within a series of flat, parallel reflections can be calculated using the Dix equation, as such:

$$v_{int} = \left[(t_2 v_{rms2}^2 - t_1 v_{rms1}^2)/(t_2 - t_1)\right]^{0.5} \qquad \text{Eqn. 2.8}$$

where: v_{int} = interval velocity

t_1 = traveltime of the first reflection

t_2 = traveltime of the second reflection

v_{rms1} = root-mean-square velocity of the first reflection

v_{rms2} = root-mean-square velocity of the second reflection

Velocity analysis is performed on selected CMP gathers and the resulting velocity function is interpolated between the selected locations (Fig. 2.14). There are many ways to estimate velocity, all of which are generally used in conjunction to improve the accuracy of the estimate. One method of estimating the seismic velocity of a particular reflector is based on computing the velocity spectrum (Fig. 2.14a). In this case, semblance - a measure of signal coherency - is displayed on a graph of velocity versus two-way zero-offset time. The stacking velocities are chosen at points of the highest coherency at times with significant event amplitude. A second way to estimate NMO velocity is to apply various NMO corrections to a CMP gather using a range of constant velocity values (Fig. 2.14b). The velocity that best flattens the reflector, as a function of offset, is picked as the NMO velocity for that surface. Another commonly used method is to display a panel of constant velocity stacks (Fig. 2.14d). Using a range of constant velocity values the program will stack a small portion of the line. The velocity that produces the highest amplitude reflection is chosen as the stacking velocity at that reflection point. In the absence of other information, the stacking velocity is used to approximate the RMS velocity for input into the Dix Equation. With the advent of high-powered computers, most processing software will display all of these methods in one analysis tool. This way the individual processing the data may take advantage of multiple methods of estimating the velocity concurrently, which improves the accuracy of the

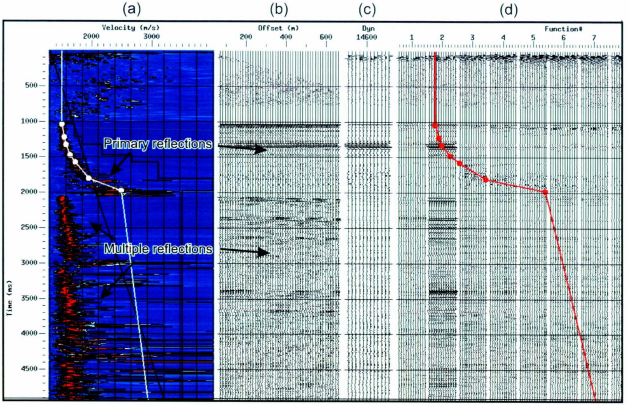

Figure 2.14 ProMAX's interactive velocity analysis tool. Each panel allows for a different method of estimating velocity and each are used concurrently to get the best possible result. The panels employed display: (a) the semblance spectrum of the particular CDP location displayed, highlighted are primary and multiple energies, (b) shows the NMO corrected gather at this location, note that primaries are flattened and multiples are undercorrected, (c) a portion of stacked data in the vicinity of the CDP being anaylzed using the chosen velocities and (d) various stacked CDP's at constant velocities.

velocity estimate (see Fig. 2.14). Velocity analysis is an iterative process. Its effectiveness is often determined by the outcome of the processes that came before it, as well as the quality and nature of the recorded data.

2.3.7 CMP stacking

Once the CMP gathers are corrected for their moveout using the NMO velocities derived from the velocity analysis, the traces that share a common midpoint can be summed together along the offset axis to produce a single stacked trace (Fig. 2.13). This has the effect of amplifying primary reflections and decreasing unwanted noise. Random noise sources are "summed out" as they do not have redundancy of sampling. For this reason CMP stacking is considered the most robust method of noise attenuation in processing of seismic reflection data. CMP stacking also has a positive effect on multiple attenuation. Multiple reflections generally have a lower velocity than primary reflections that occur at the same depth. It is possible to attenuate this energy during the stacking process by picking velocities that result in an undercorrected multiple (Fig. 2.14). Undercorrected energy that deviates from zero offset in the CMP gather will be "summed out" during the stack. The stacked section has a higher signal-to-noise ratio than the previous shot and CMP gathers, but still displays large diffraction hyperbolae resulting from dipping reflectors and various edge effects (Fig. 2.15a). Schlumberger's Oilfield Glossary defines a diffraction as "a type of event produced by the radial scattering of a wave into new wavefronts after the wave meets a discontinuity such as a fault surface, an unconformity or an abrupt change in rock type. Diffractions appear as hyperbolic or umbrella-shaped events on a seismic profile" (Schlumberger, 2012). In order to collapse

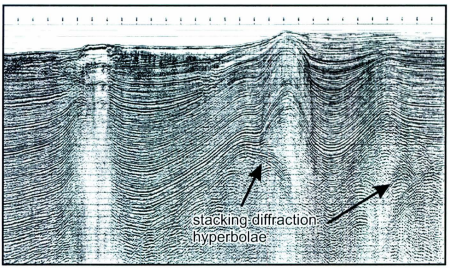

(a)

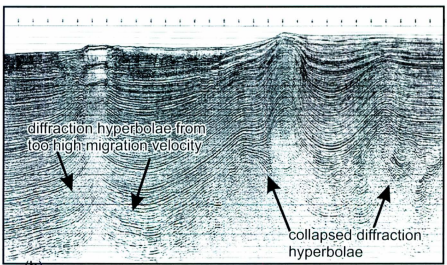

(b)

Figure 2.15 (a) A stacked section and (b) the same section as (a) but migrated. Note that events have become steeper and shorter in the migrated section although some diffraction hyperbolae resulting from incorrect migration velocities remain (from Yılmaz, 2001).

these hyperbolic diffractions, proper migration of seismic data will properly position reflections by making use of the diffracted energy.

2.3.8 Migration

Migrating the data is the last crucial process in the seismic reflection data processing flow. Simply put, migration focuses the image. As previously stated, the common midpoint for dipping reflectors is not properly positioned. The program, assuming the reflecting surfaces are horizontal, will choose a reflection point between source and receiver pairs. At the stacking stage, the reflection point is located down-dip from its true location in the subsurface. Also, when surfaces are dipping the midpoint will not occur discretely, resulting in a distortion of certain reflection points. The migration process will restore the image and move the reflection points up-dip to their true subsurface location (Yılmaz, 2001). Migration also collapses diffraction hyperbolae to a single point, thereby focusing the image further. Unlike velocity analysis, the output of migration is self-evident and the success of the chosen velocity function is obvious from the resulting image. Migration velocities that are too high result in upward-facing diffraction hyperbolae (i.e. "smiles") and migration velocities that are too low result in downward-facing diffraction hyperbolae (i.e. "frowns"). In general, stacking velocities and migration velocities are not the same and it is important to spend considerable time picking the proper velocities to focus the image as well as possible. Migration is an essential step in seismic data processing, and the correct migration velocity function will make structural and stratigraphic interpretations possible. Figure 2.15 displays a stacked section and a migrated section, illustrating how migration causes dipping reflectors to be

moved up-dip in the section and diffraction hyperbolae resulting from the stacking process to collapse.

2.4 Seismic Interpretation and Mapping

Detailed seismic interpretations were carried out by hand on paper sections by carefully tracing prominent seismic reflections and major unconformities across the profiles. Structures were mapped on a line-by-line basis and interpretations were followed through closed loops in the survey grid. Line crossovers were used to correlate prominent reflections across the study area, allowing a stratigraphic framework to be erected.

In seismic reflection profiles unconformities are often delineated based on the truncation of steeper-dipping marker reflectors by a prominent but less steeply-dipping surface. However, there are various other reflection terminations that also reveal the presence of unconformities; these include: onlap, offlap, downlap and toplap (see Figs. 2.16 and 2.17). Onlap is a relationship between seismic reflections in which less steeply-dipping, younger layers converge and gently lap onto older layers. This represents the progressive fill of a depression and subsequent encroachment of the deposits over a pre-existing high. When strata thin below the vertical resolution of the seismic reflection data, an offlap reflection termination occurs. Downlap is a termination of reflections in which steeply-dipping younger layers lap on top of a less steeply-dipping older layer. Downlap terminations represent the progressive advancement of a depositional system into a new area. Lastly, a toplap reflection termination occurs when sediments bypass a nearly flat and stable depositional surface and built sedimentary piles progressively

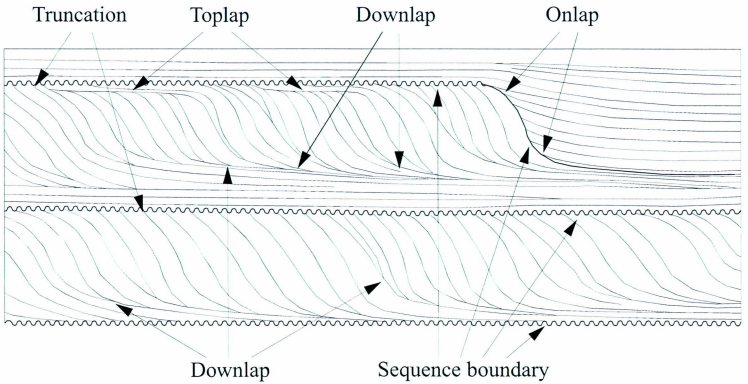

Figure 2.16 Schematic demonstration of reflector terminations used for interpretation (Modified from Isler, 2005).

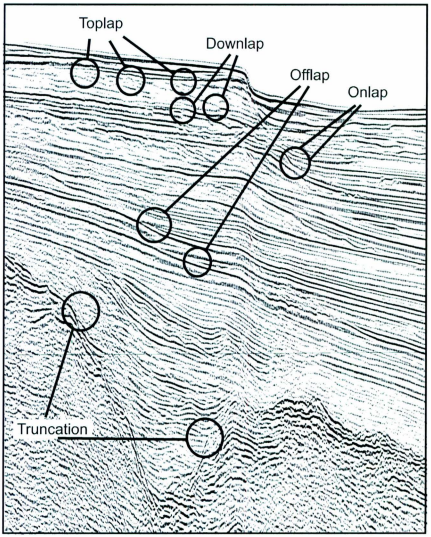

Figure 2.17 Seismic example from the 2008 Cilicia Basin survey demonstrating the various reflector terminations used to conduct the interpretation of seismic reflection profiles.

further seaward. Toplap is commonly observed in deltaic settings and it signifies the cycles of delta progradation (Mitchum et. al, 1977). In seismic reflection profiles acquired perpendicular to the shoreline, deltas display a distinct wedge-shaped architecture, with pronounced thinning both toward and away from the shoreline (Gilbert, 1885; Kenyon and Turcotte, 1985). The internal architecture of deltas is also very distinctive. At the proximal end near the channel mouth, the sediments are nearly horizontal; these beds are often referred to as the topset beds and are characterized by toplap reflection terminations. Moving into slightly deeper waters, the prodelta sediments are inclined and are referred to as foreset beds (Mitchum, 1977). The foreset beds of a delta are imaged as seismic packages characterized by variably seaward-dipping clinoform reflections. In the deeper water setting of the inner shelves, the gently seaward-dipping to nearly horizontal successions are referred to as the bottomset beds and are imaged in seismic reflection profiles as downlap reflection terminations (Mitchum, 1977). The topset-to-foreset transition of a delta package marks the delta front and can give an first estimate of the position of the former shoreline during the time of deposition, especially in a non-aggrading system; these transition points were carefully mapped in seismic reflection profiles, when present. A schematic of a prograded delta system is shown in Figure 2.18.

Several discontinuities that extend with steep angles and cut many prominent reflections were discovered in the seismic reflection profiles (see Fig. 2.19). Examination of the seismic reflection profiles revealed that the reflections on the left and right sides of the discontinuities could be confidently correlated across these breaks; these discontinuities are interpreted as faults. The apparent vertical and horizontal offsets of

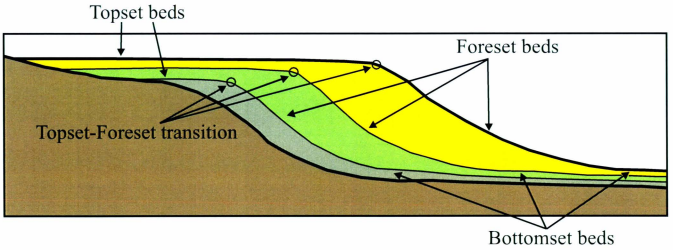

Figure 2.18 Schematic cross-section of a prograded delta package illustrating: topset, foreset and bottomset beds, as well as the topset-foreset transition points observed in seismic reflection profiles.

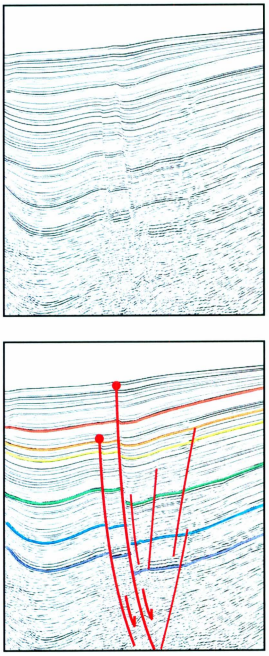

Figure 2.19 An example of a seismic reflection profile that displayed discontinuities in reflections. Bundles of reflections with similar acoustic characteristics were highlighted so that reflections on the left and right sides of the discontinuities could be confidently correlated across these breaks; these discontinuities are interpreted as faults. Tip points are shown as red circles on top of faults.

the prominent reflections across the fault allowed for the identification of the footwall and hanging wall blocks and the sense of motion along the fault plane. In addition to these discontinuities, the identification of the growth strata wedges further assisted in the determination of the footwall and hanging wall blocks across the faults. For example, a prominent sedimentary wedge that thickens towards the fault and displays growth strata on the block that has shifted downward along a fault that shows extensional separations of prominent reflections is labeled as the hanging wall block of a normal fault (Fig. 2.20). Similarly, a prominent growth strata wedge that thickens away from the fault and is nestled on the back limb of a block that has shifted upward along a fault showing contractional separations of prominent reflections is labeled as the hanging wall of a reverse fault (see Fig 2.20).

The tip points of the faults were marked in the seismic reflection profiles (see Fig 2.19) and the faults are often classified on the basis of the angle of their trajectory. For example, a curved fault plane that is concave upwards is called a listric fault. The timing of fault activity can be broadly determined by the effects of the fault on the surrounding sedimentary succession. For example, the termination of the development of growth strata on the hanging wall and the eventual blanketing of the fault step by sediments that do not show any inflection is interpreted as the cessation of activity on that particular fault (Fig 2.19). The soles of faults in the study area were difficult to image, and it is assumed that most of the listric faults in the Inner Cilicia Basin sole somewhere in the Messinian successions either at or below the M-reflector (Chapters 4-5).

Lastly, over the crestal regions of a number of antiformal structures, sedimentary strata are imaged as converging reflectors. Detailed examination of these regions reveals

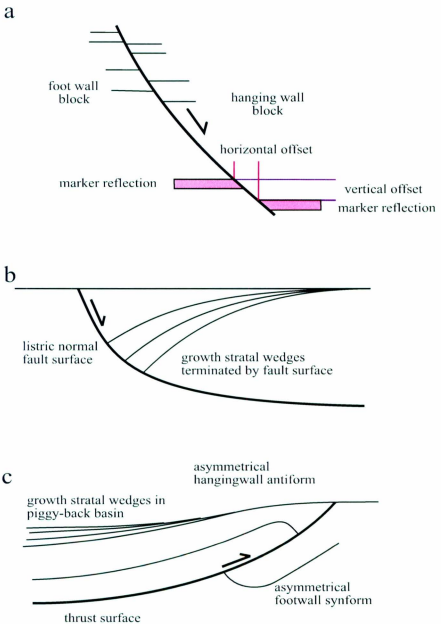

Figure 2.20 Secondary structures associated with (a) horizontal and vertical separation of marker reflections in a normal fault, (b) growth strata wedges developed in a listric normal fault and (c) growth strata wedges developed as piggy-back basins in a thrust fault (modified from Aksu et al., 2009).

that this architecture is often imaged as the convergence of prominent reflectors and onlap/offlap of reflections toward the crest of the structure. A number of these internally convergent reflections on top of one another are interpreted as stacked progressive syn-tectonic unconformities, similar to those described in the large fold-thrust belts (e.g., Riba, 1976).

2.5 Sediment volume and subsidence rate calculations

On the basis of acoustic character and continuity, the seismic reflection profiles are divided into three units: Units 1-3, where Unit 1 is further subdivided into subunits 1a, 1b and 1c (see Chapter 4 for detail). Four marker horizons (the M-, A-, P- and Q-reflectors) are traced throughout the study area (see Chapter 4 for detail). Ages for the M- and A-reflectors are assigned using correlations with two offshore exploration wells. The age of the Q-reflector is taken from Aksu et al. (1992a,b), whereas the age of the P-reflector is assigned through interpolation between P- and Q-reflectors (see Chapter 4 for detail). The seismic reflection profiles were depth-converted using the interval velocities extracted from the seismic reflection data processing (see Chapters 3 and 6 for detail). Sediment volume calculations were done in the following four isopach maps constructed using the depth converted seismic reflection profiles and the software Petrosys: (i) a total isopach map of the Pliocene-Quaternary successions of Unit 1, (ii) an isopach map of the sediments contained between the M- and A-reflectors, i.e. Unit 1c, (iii) an isopach map of the sediments contained between the A- and P-reflectors, i.e. Unit 1b, (iv) an isopach map of the sediments contained between the P-reflector and the seabed, i.e. Unit 1a.

The total volume of sediments contained within each isopach map was calculated using the seismic interpretation software Petrosys. Because the available well data lacked detailed descriptions of exact sediment type, densities, porosities etc., a number of assumptions and estimates had to be made to arrive at a dry, solid weight for each interval. These are discussed in detail in Chapter 6.

The subsidence rates are calculated using the OSXBackstrip 1D Airy backstripping method with exponential reduction of porosity to extract the tectonic subsidence in the Cilicia Basin. The method systematically removes from successive layers in a basin the effects of sediment compaction and sediment and water loading so that the amount of tectonic subsidence can be determined. It is based on the algorithms of Allen and Allen (1990) and Watts (2001). The technique presupposes that the way water and sediment loading deform the crust as well as the changes that take place during burial-related dewatering and sediment compaction are known. The details of the subsidence rate calculations are presented in Chapter 6; results are discussed in Chapter 7.

CHAPTER 3: SEISMIC DATA PROCESSING

The primary seismic reflection data used for this study consist of the easterly portion of the 2008 Cilicia Basin survey (Fig. 3.1) and include six transects running radially basinwards from the Göksu River delta and one long cross profile running southwest-northeast crossing the Inner and Outer Cilicia Basin, totalling ~750 km, and were processed at Memorial University of Newfoundland by the authour. The purpose of this chapter is to discuss in detail the processing techniques applied to the seismic data and any limitations that were encountered. Data processing was carried out using the Landmark ProMAX© software and the processing flow applied to the data is provided in Figure 3.2. All of the lines were processed using the same general flow with only minor variations from line-to-line due to changes in geology, water depth and acquisition parameters (such as the misfiring of guns, rough seas, etc.). Further discussion of the various processing steps will be conducted in subsequent sections. The additional seismic reflection profiles used to carry out the interpretation include the remainder of the data collected during the 2008 Cilicia Basin survey as well as transects from the 1991 and 1992 surveys, all of which were processed at Memorial University of Newfoundland. The Turkish Petroleum Corporation provided deeper-penetration seismic reflection profiles that were also used for interpretation.

3.1 Pre-processing

The first stage in processing the 2008 seismic data highlighted in Figure 3.1 was to load the raw SEG-Y files into ProMAX© using the SEG-Y input application. Because most lines were too long to be read into ProMAX© they were input in segments (e.g. 72a

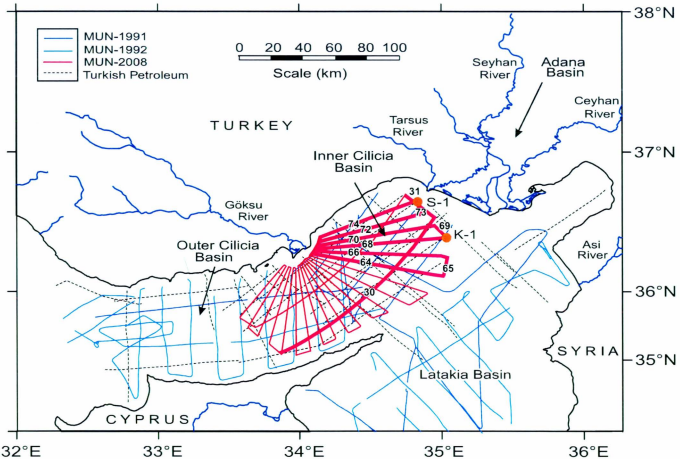

Figure 3.1 Map showing the locations of the seismic reflection profiles discussed in this chapter. Seismic reflection profiles processed for this study by the author include: lines 64-66, 68, 70, 72 and 74 and are included in the back panel of this thesis.

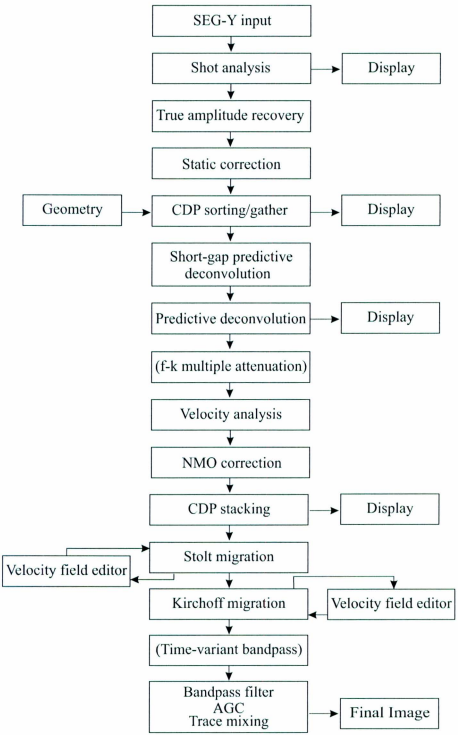

Figure 3.2 ProMAX seismic reflection processing flow applied to the data highlighted in Figure 3.1.

and 72b) with an overlap roughly equal to the length of the streamer. Each segment was processed independently using similar parameters. The segments were recombined at the stacking stage by splicing the lines together at a carefully chosen location on each seismic reflection profile within the overlapping common depth points (CDPs). This location is chosen to avoid any end-of-line effects, as well as the NMO mute. After being read into the program the raw shot gathers were inspected to get a first impression of signal-to-noise ratio and/or problematic sections. Figure 3.3 displays two typical shot gathers, one from a deeper water setting and one from a more shallow water setting. Another useful way of viewing the shot data is to display the shots as a single channel near-trace gather. This allows for the first glimpse of the subsurface geology along the profile. Figure 3.4 shows the near-trace gather of a seismic reflection profile from the Inner Cilicia Basin.

3.1.1 Static correction

When conducting a seismic survey, a time delay between shot and recording may be introduced to avoid imaging the water column, therefore not utilizing the full penetration depth available for the study. This delay is usually variable, depending on the change in water depth along each profile. Upon inspecting the shot data from each seismic reflection profile, it was determined that no manual delay was introduced during the portion of the survey described in this chapter and highlighted in Figure 3.1. However, it was discovered that the shot data experienced a uniform time shift that was consistent across all profiles. The 2008 survey configuration was such that the first offset (i.e. the distance from the shot point to the first receiver) was equal to 70 m. In this case, the direct wave should arrive on the seismic record at: $t_{arrival} = x/v_{water}$ = 70 m / 1.5 m/ms = 46 ms, however, as seen in Figure 3.5 the direct wave's arrival time at first offset is

(a)

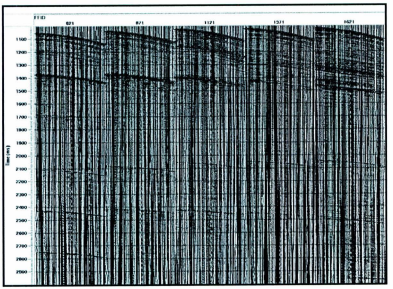

(b)

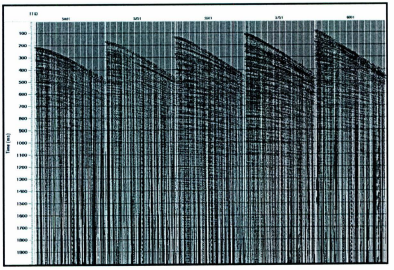

Figure 3.3 Selected raw shot gathers from (a) a deep water setting and (b) a shallow water setting. Most of the data are obscured by a low frequency noise appearing as vertical streaks on the seismic shot record.

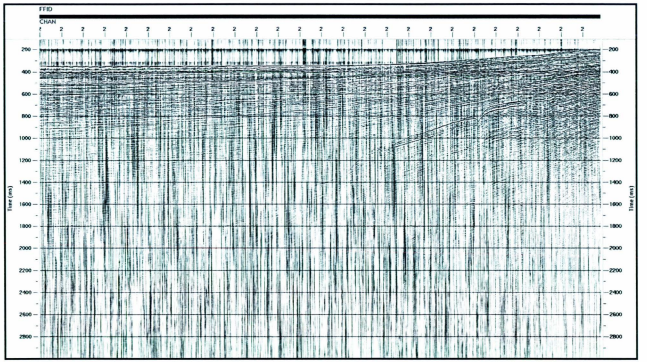

Figure 3.4 The near trace gather of the raw data from the westerly portion of line 72. Some near-surface primary reflections are visible but there is an obvious need for frequency filtering and amplitude equalization to view later events.

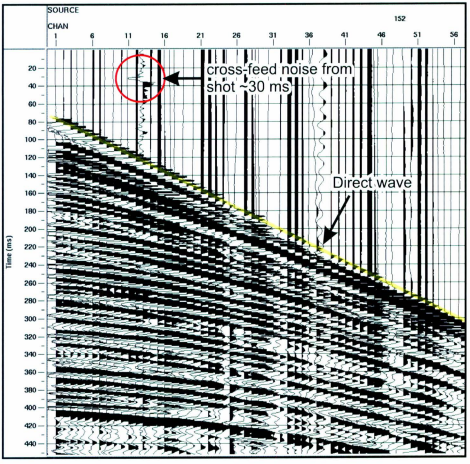

Figure 3.5 Part of an unfiltered shot record highlighting the earliest arrivals. The direct wave (outlined in yellow) has an arrival time at first offset of 76 ms, but is expected to arrive at 46 ms (discussed in text). This indicates that the data has experienced a downward shift of 30 ms. Also, the cross-feed noise from the shot pulse (outlined in red) is seen on the noisy channel number 13 to arrive at 30 ms. This is an indicator of the time of the shot pulse, confirming the downward shift of 30 ms.

actually 76 ms. This delay is caused by the particular set-up of the synchronization of the shooting box with the recorder and was corrected by applying a static shift of -30 ms to all shots using the "Hand Statics" process of ProMAX© to restore the time of the shot to zero. A secondary confirmation of this downward shift in time is seen on the noisy channel number 13. At 30 ms, a pulse occurs, which is the cross-feed noise from the shot pulse (Fig. 3.5). This indicates that the shot pulse occurs on the seismic record at 30 ms instead of the expected 0 ms shot time.

3.1.2 Frequency filtering

Low-frequency swell and cable noise

The signal-to-noise ratio of the shot gathers was low. Figure 3.6a shows the frequency spectrum of a selected shot gather (shot no: 621; Fig. 3.3a) from the southwesterly portion of Line 30. The bandwidth of the seismic source should lie ~50-200 Hz, but as seen from the amplitude spectrum of this selected shot (Fig. 3.6a), this bandwidth is overwhelmed by a dominating low frequency noise, occurring at ~0-2 Hz. Further analysis of the frequency spectra of all seismic reflection profiles highlighted in Figure 3.1 showed that each profile contained this high amplitude, low frequency noise, which consistently occurred at ~0-2 Hz (Fig. 3.6a). The low frequency noise could be directly observed on the shot gathers and close analysis showed strong coherence (Fig. 3.7). This noise was likely generated by the flow and swell of the sea, which is a common problem in marine surveys, especially those that employ fluid-filled streamers (Elboth et al., 2009; Yılmaz, 2001).

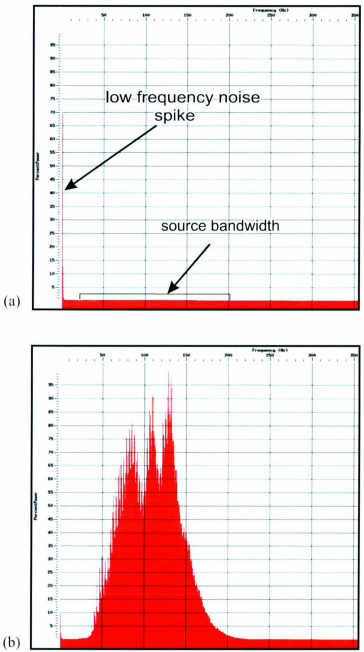

Figure 3.6 The amplitude spectra of shot gather 621 displayed in Figure 3.3a: (a) before any frequency filtering and (b) after frequency filtering. After the frequency filter is applied, the low frequency noise spike is attenuated and the source bandwidth is amplified.

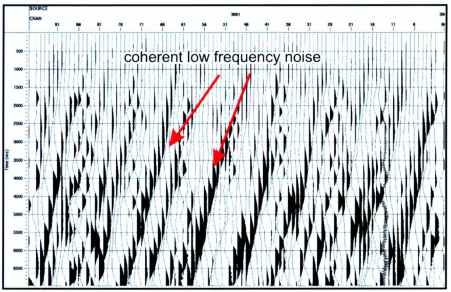

Figure 3.7 A shot gather from Figure 3.3a that has a low-pass filter of 0-10 Hz applied. By viewing the gather in this way, the low frequency noise is isolated and its coherent nature is obvious.

Bandpass filtering

To carry out the interpretation of the seismic reflection profiles, the frequencies that lie outside the seismic bandwidth (i.e. noise) must be removed. A bandpass filter was designed to exclude the unwanted frequencies that had an allowed bandwidth containing the relevant signal and slopes between the high- and low-cuts that were large enough to not include the noise, yet gentle enough to avoid ringing that can be associated with steep filter slopes. The filter used for displaying the data in the seismic reflection processing flow was chosen to be a Butterworth bandpass filter (40Hz low-cut @ 36 db/octave and 200 Hz high-cut @ 36 dB/octave). Figure 3.6b displays the frequency spectrum of a shot gather after the application of this filter and clearly the frequency filter has uncovered the seismic bandwidth. The shot gathers have also been improved and primary and multiple reflections can now be seen at deeper traveltimes (Fig. 3.8).

Time-variant filtering

Late in the processing flow (see Fig. 3.2), it was often necessary to apply a time-variant bandpass filter to remove the higher frequencies that still remained deep in the profile where only lower frequency reflections can be imaged. When setting up the time-variant filter, various time gates must be chosen at locations where the filters will be applied. A gap is left between the chosen time gates to allow the program to linearly interpolate the filters creating a smooth transition (Fig. 3.9a). After the time-variant filter has been applied deeper reflections, such as the M-reflector (see Chapters 4-5) and those beneath it, become more visible (Fig. 3.9b). Figure 3.9 shows a series of migrated

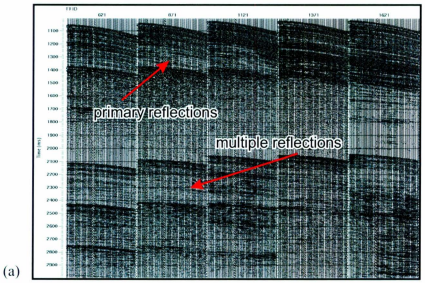

(a)

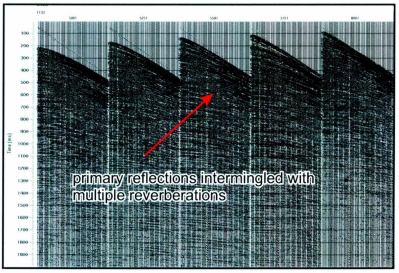

(b)

Figure 3.8 The same selected shot gathers from Fig. 3.3a,b with a frequency filter applied (pass bandwidth ~40-200 Hz). Primary and multiple reflections have been uncovered and the highest amplitudes are now concentrated at shorter arrival times in each setting. This effect is greatest in (b), i.e. shallow water shots; discussed in Chapter 2.

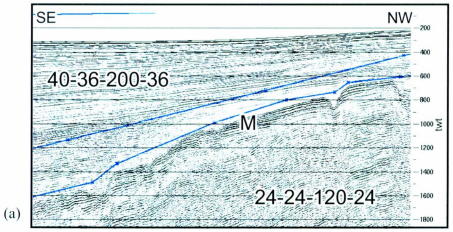

(a)

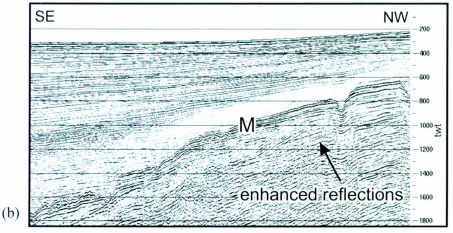

(b)

Figure 3.9 The northwestern portion of seismic reflection profile line 72 (a) with the standard Butterworth frequency filter (40-36-200-36) applied uniformly throughout the section. The chosen time gates and filter parameters used for time-variant filtering are also shown, (b) the same seismic reflection profile with the above time-variant filtered parameters applied. Removing the lower frequencies at deeper traveltimes resulted in enhanced reflections beneath the M-reflector (marked by an "M").

sections from the westerly shelf-edge portion line 72 before and after time-variant filtering. The chosen time gates and filter parameters are also given (Fig 3.9).

3.1.3 Gain applications

Recall from Chapter 2 that the amplitude of seismic energy decreases from the source point as 1/distance, in a homogeneous Earth. Therefore, the highest amplitude reflections observed on the seismogram will originate from the near-surface reflections. A gain correction was applied to the survey data to correct for this loss of amplitude with depth, using the "True Amplitude Recovery" tool of ProMAX©. A gain function with a time power scaling of 1 was applied to the 2008 data, which assumes a constant velocity Earth. For display purposes only (including final displays) an amplitude balancing function was applied in the form of "Automatic Gain Control" (AGC). AGC involves scaling the amplitudes of reflections in inverse proportion to the average signal level in a sliding window. The most favourable time gate window used to calculate the gain function was determined to be 500 ms. Because AGC alters the true amplitude information contained within the signal, it was never permanently applied to the data but used only to improve visibility in displays. Figure 3.10 shows the same filtered shots as in Figure 3.8 after the application of True Amplitude Recovery and AGC. Late arriving events are now clearly visible for the first time.

3.2 Geometry and CDP sorting

In order to sort the data into CDPs, which is necessary for stacking, the survey geometry must be correctly applied to each line individually. This involves assigning a location to each trace from a binning spreadsheet. During the 2008 Cilicia Basin survey

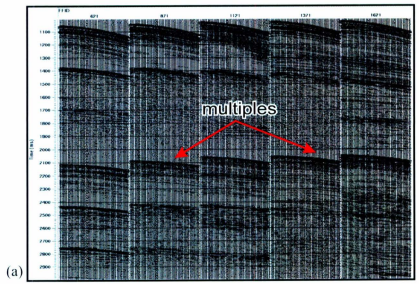

(a)

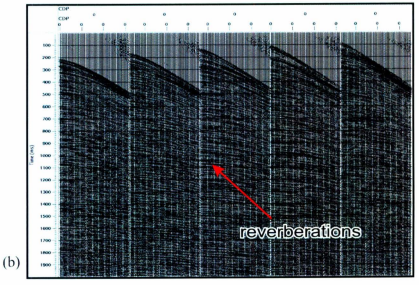

(b)

Figure 3.10 The same selected raw shot gathers as displayed in Figs. 3.3 and 3.8 with True Amplitude Recovery, AGC and a bandpass filter applied. All events are now visible down through the section, but issues such as multiple reflections and reverberations have become apparent.

the shot point coordinates were recorded by the Global Positioning System, GPS. The exact coordinates of each shot point were input via text files recorded during the survey and combined with parameters such as: minimum offset, receiver spacing, near and far channel numbers and channel increment. This is in contrast to previous data processed at MUN that used the "Automatic 2D Marine Geometry" process, which automatically creates a straight-line, constant shot interval geometry and does not account for changing vessel speed or curvatures and gaps in the lines. Applying the geometry using the latitudes and longitudes recorded by the GPS allowed for more accurate mapping of location, which was imperative because the 2008 Cilicia Basin survey had a tighter line density than employed in previous years and this study used an integrated digital interpretation in Landmark's Seisworks seismic interpretation software for later volume calculations. Once the survey geometry was applied, the completed geometry spreadsheet was carefully examined to ensure that each trace corresponded to the proper CDP for quality control.

It should be noted here that on paper copies miss-ties with the crossovers of other seismic lines from the same survey were discovered on the order of ~300 m upwards to 1 km at one point. Crossover points on paper copies are determined using fixes recorded manually by scientific personnel on board which are gathered every 10 minutes. The closer line spacing and hence multitude of crossovers in this survey drew out some problems in this method. When the data were input into Seisworks using the GPS coordinates to determine location, the crossover miss-ties within the 2008 data were generally not as significant. The method of inputting coordinates from the GPS is

therefore a better, more accurate method and should be used in the future - especially if a digital interpretation program will be used.

3.3 Predictive deconvolution

Predictive deconvolution was used on the dataset to shorten the source wavelet and attenuate short- and long-period multiples. Many trials were conducted to determine the best deconvolution outcome. The best result was produced prior to stacking when a "short-gap" predictive deconvolution was applied, with an operator length of 8 ms, followed by a second predictive deconvolution, with a longer operator length equal to 125 - 200 ms. The "short-gap" deconvolution was applied to shorten the source wavelet and is meant to approach spiking deconvolution without generating as much high frequency noise. The operator length was chosen to be equal to the second zero crossing of the autocorrelation function. The longer-lag deconvolution operator was chosen to predict and attenuate multiples in a sliding window equal to the operator length down through the section. This iterative process of predictive deconvolution generally had a positive effect on attenuating the reverberations and seabed multiples. The regions in which deconvolution failed were likely the results of a violation of the assumptions used in the algorithm, such as in areas with steeply dipping reflectors or areas with increased noise levels. Furthermore, the source wavelet for the 2008 EMED survey was not quite minimum phase, which is an assumption in the predictive deconvolution algorithm. Hence, the outcome is not always optimal. Predictive deconvolution introduced additional high frequency noise to the seismic reflection profiles, though subsequent frequency filtering and the common midpoint stacking method had a positive effect on its

removal. Figure 3.11 displays part of a seismic reflection profile before and after the above process of predictive deconvolution was applied.

3.4 Velocity analysis

Accurate velocity analysis is a critical step in seismic reflection data processing. The successful picking of stacking velocities at specified supergather locations determines the output of the stack and hence all other processes. Hence, considerable time was spent on analyzing the velocities of the seismic reflection data. The velocity analysis was conducted at carefully chosen locations where anomalous effects could be avoided, such as in regions with highly dipping reflections and where changes in dip occur. It was important to avoid these regions to allow the linear interpolation of the normal moveout corrections to be reasonably accurate. A balance had to be found between too many and too few analysis locations. Figure 3.12 shows the output of a stack when too few analysis locations were chosen as well as the output after more were added. Note that the stack with too few locations is not imaged properly and reflections are discontinuous with a "fuzzy" appearance. Next, supergathers were formed using the "2D supergather formation" process of ProMAX©. These supergathers are formed by summing together several adjacent CDPs at the chosen location (i.e. CDP) for velocity analysis. This process increases the quality of the semblance spectra, thereby allowing for a more accurate velocity analysis. The number of traces chosen for summation into each supergather was 13, which is a value higher than the fold of the data (fold = 12).

Once the locations are determined and supergathers were formed, stacking velocities were picked using the "interactive velocity analysis" tool of ProMAX©. A

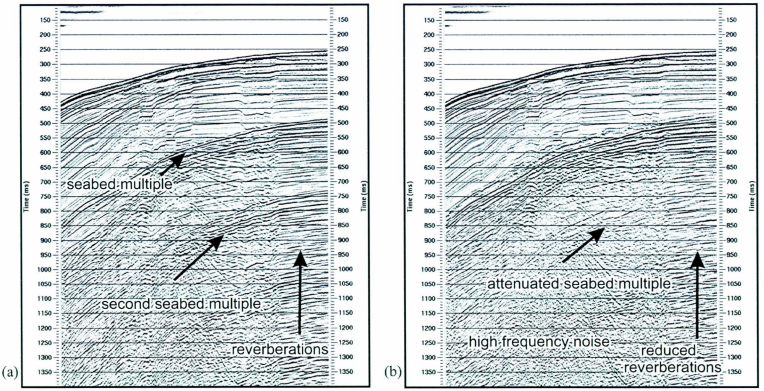

Figure 3.11 A near trace gather of the northeasterly portion of line 30 (a) before and (b) after the iterative process of predictive deconvolution described in text (section 3.3). The deconvolution process has done a better job of attenuating the second and third seabed multiples than the first, though reverberations have also been reduced. Deconvolution has introduced some extra high-frequency noise, but common-midpoint stacking will remove most of this non-coherent noise.

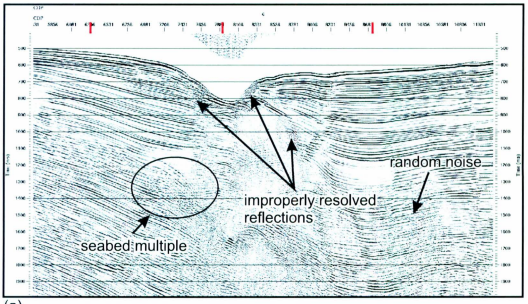

(a)

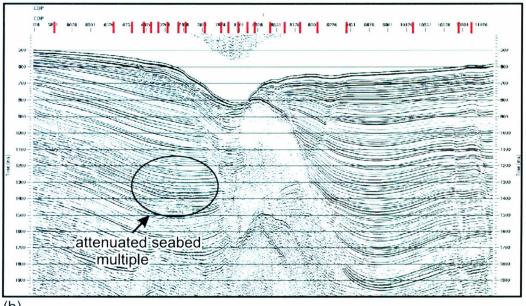

(b)

Figure 3.12 Stacked section (a) before and (b) after improved velocity analysis. Supergather locations for each stack are shown in red at the top of each section. Stacked section shown in (b) was improved by adding more supergather locations. An increased number of supergathers also had a positive effect on attenuating multiples and random noise.

combination of semblance peaks, dynamic stacking and visual NMO inspection were used to choose the best stacking velocity for each strong reflection. Figure 3.13 shows an ideal velocity analysis gather and its corresponding velocity picks from the southwesterly portion of line 30 (also see Fig. 3.1). The velocity picks for primary reflections are chosen along points of maximum semblance ("bulls-eyes") and the NMO panel is used to ensure primary reflections are flattened. The points of maximum semblance for multiples are avoided, leaving the multiple reflections undercorrected. Figure 3.13b shows the area along the seismic reflection profile where the analysis shown in Figure 3.13 occurred.

Two distinct problems were encountered while processing the data for the study area. In shallow water, energy trapped in near surface layers gave the profiles a very reverberatory characteristic. This made velocity analysis extremely difficult because the semblance spectra were littered with multiple energy, giving a smeared appearance. Because the velocities of primary and multiple reflections were very similar, it was difficult to distinguish between primary and multiple energy. Figure 3.14 shows a velocity analysis for a supergather location in shallow water along line 73 (also see Fig. 3.1). Picks were made at higher velocities in an attempt to avoid "peg-leg" multiple energy, which has a lower, albeit marginally, stacking velocity. In particularly reverberatory sections it was sometimes useful to display panels of the data stacked at constant velocities. The stacking velocity was then chosen based on visual inspection of the best stack produced for the reflector in question. Figure 3.15 shows a number of constant velocity stacked panels used for processing shallow water data. The second problem was encountered at the flanks of steeply dipping salt structures. Here, the velocity increases so sharply that the semblance spectra is miscalculated, giving a

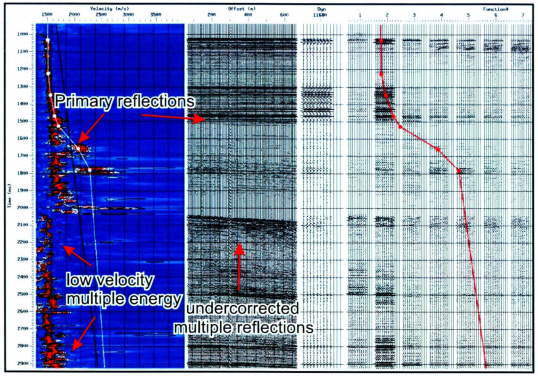

Figure 3.13a An example of a ideal velocity analysis location chosen from the southwesterly part of line 30. The semblance peaks are well-defined and the multiples can be readily distinguished from primaries. The velocity function is chosen to flatten primary energy and leave multiple energy undercorrected.

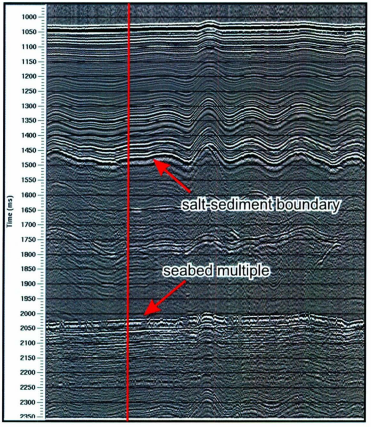

Figure 3.13b A portion of the southwesterly end of line 30 illustrating the location of the velocity analysis supergather from Fig. 3.14a (highlighted in red). This profile occurs in deeper water (~1000 ms) and has a hard salt layer boundary occuring at ~1500 ms and a seabed multiple occuring at ~2000 ms. The location of line 30 is given in Fig. 3.1.

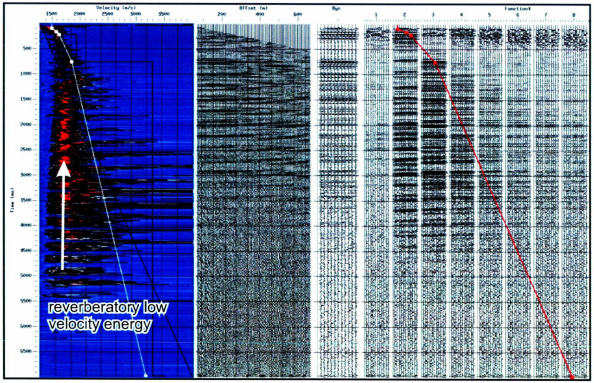

Figure 3.14a An example of a velocity analysis location along line 73 that is dominated by shallow water reverberations. The semblance spectrum is smeared and velocity picks are chosen at the higher end of the peaks to avoid multiple energy.

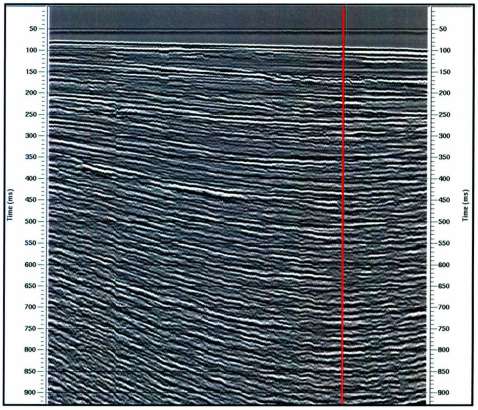

Figure 3.14b A portion of line 73 showing the location of the supergather being analysed in Fig. 3.14a. This profile occurs in very shallow water depths (~100 ms) and is dominated by reverberatory peg-leg multiples. The location of line 73 is given in Fig. 3.1.

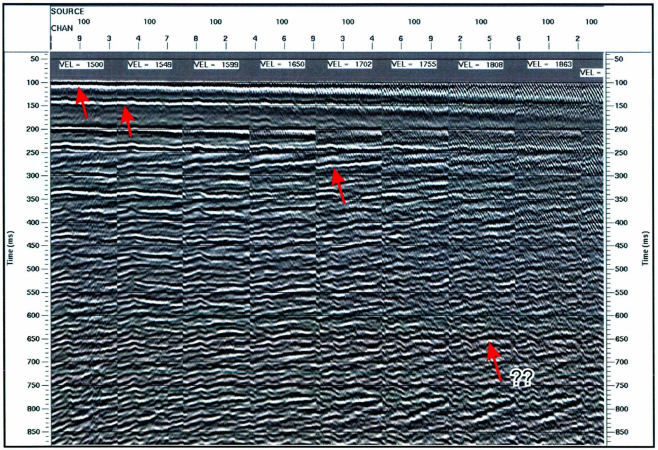

Figure 3.15 An example of the constant velocity stacks used to determine the correct stacking velocities in shallow sediments where conventional velocity analysis was not adequate. Velocity picks are shown by red arrows.

scattered appearance. Figure 3.16 shows a demonstration of a velocity analysis location and the picks made on top of a salt structure.

Choosing the best stacking velocity function was often an iterative process, but in some areas of very shallow water with soft underlying sediments the primary reflections could not be imaged, and it had to be conceded that the 2D seismic reflection method is not perfect and these reflections were likely not properly imaged during acquisition. The final images produced from these sections are highly reverberatory with discontinuous reflections, making detailed interpretation in these areas virtually impossible.

3.5 NMO correction and common midpoint stacking

Once a satisfactory velocity function was determined a normal moveout correction (NMO) was applied to the dataset to flatten the reflections in the CDPs. The velocity chosen for a given reflection determines the degree of flattening. Next, the data were stacked together along CDPs, i.e. multiple CDP traces were added at constant time. Flattened reflections (i.e. primaries) are stacked in and undercorrected reflections (i.e. multiples) are stacked out. Random noise sources, such as the high frequency noise from deconvolution, were also reduced because they do not occur consistently across traces in the CDP gathers. The stacked seismic reflection profiles show a significant increase in signal-to-noise ratio when compared to the near-trace gather of the same section (Fig. 3.17). The image, however, is now marred by diffraction hyperbolae and migration is necessary to collapse these diffractions and move reflectors up-dip to their true subsurface location. Diffraction hyperbolae result from the assumption of the CMP stacking method that reflection points lie on vertical lines midway between the shots and

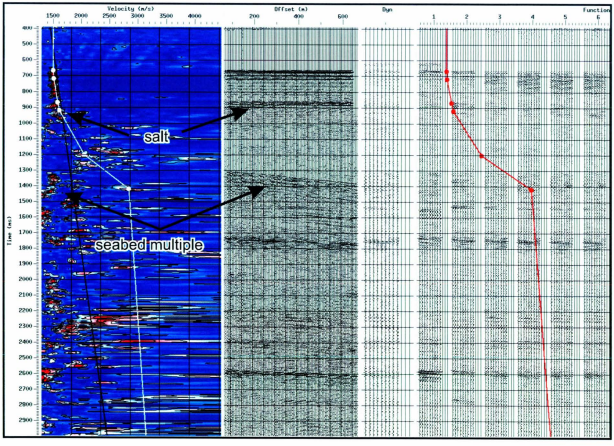

Figure 3.16a An example of a velocity analysis location from the flanks of a salt structure. The semblance spectrum has a scattered appearance in the presence of these steeply dipping, high velocity edges.

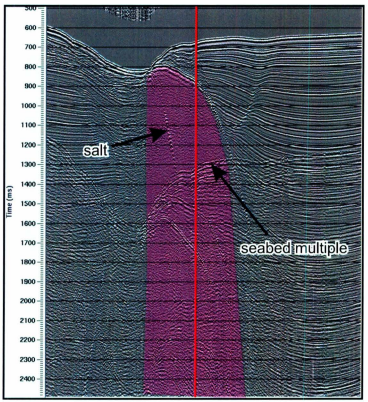

Figure 3.16b A portion of line 66 illustrating the supergather location shown in Fig. 3.16a. In order to properly resolve this structure, many analysis locations had to be chosen (see also Fig. 3.13). This location occurs on the flanks of a salt diapir with little sediment cover. The location of line 66 is given in Fig. 3.1.

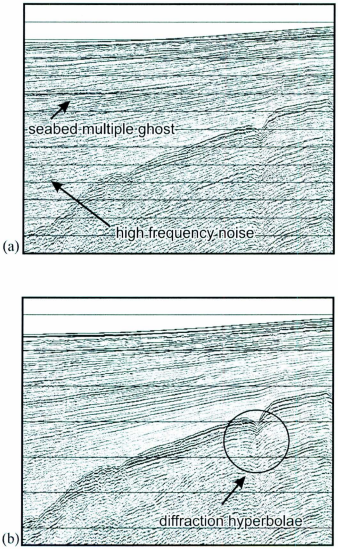

Figure 3.17 The westerly portion of line 72 as (a) a near trace gather and (b) a stacked section. In the stacked section the multiple ghost is fully attenuated and the level of noise is drastically reduced.

receivers. In areas of steeply dipping reflectors or complicated geology this assumption is violated. Therefore, in these areas the stacking velocities are not sufficient as migration velocities and considerable time had to be spent to edit the stacking velocity function for migration.

3.6 Migration

Migrating the data is the last major step in the processing flow (Fig. 3.2). Migration ensures the data are accurately located and diffraction hyperbolae from the stacking process are properly collapsed. A three-step process was used to migrate the data that involved multiple iterations to produce the desired outcome.

Firstly, the data were migrated at constant velocities using the "Stolt migration" process. Constant velocity Stolt migrations were conducted at 1500 m/s, 1600 m/s, 1700 m/s, 1900 m/s, 2100 m/s and sometimes upwards to 2300-2700 m/s. Figure 3.18 displays three constant velocity Stolt migrations along the central portion of line 30, at (a) 1500 m/s, (b) 1800 m/s and (c) 2100 m/s. Each section was then visually inspected to determine a general velocity-depth trend. Next, the "velocity viewer/editor" tool was used to open the velocity model in an interactive tool that allows the chosen velocity functions to be edited according to the Stolt migration outcomes. Secondly, a variable velocity Stolt migration was run using the new velocity model. The Stolt migration is not ideal for final migration purposes, but it takes a much shorter time to run than other algorithms and allows for a quick view of the data migrated with the new velocity model. After the Stolt variable velocity migration was inspected, the velocity function often required further editing. Once this process seemed satisfactory, a Kirchoff time

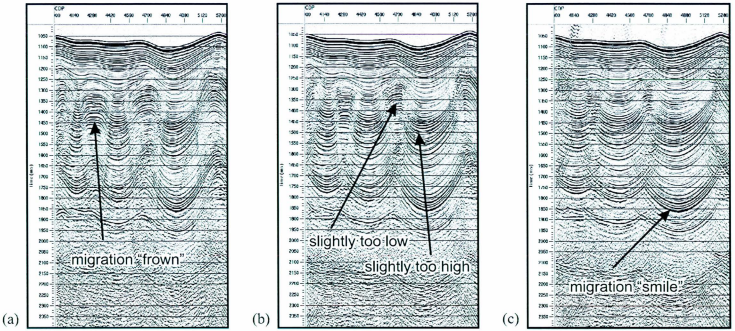

Figure 3.18 An example of a series of constant velocity Stolt migrations migrated at (a) 1500 m/s, (b) 1800 m/s and (c) 2300 m/s. Migration velocities that are too low, leave the diffraction hyperbolae undercorrected resulting in a migration "frown". As the migration velocity gets higher, reflections that properly migrate at lower velocities display migration "smiles".

migration was applied to the data. This algorithm produces the best migration outcome. This process takes many hours to complete so it is best to have a very good idea of the velocity model prior to running it. After the Kirchoff time migration had finished the data were again visually inspected to determine if the migration velocity model was successful. The process was usually repeated two or three more times until the desired output was achieved (Fig. 3.19). A final migration should have all diffraction hyperbolae collapsed. Figure 3.20 shows a stacked section and its corresponding migration. Some places, including areas with out-of-plane reflections, are notoriously difficult to migrate so the "law of diminishing returns" was invoked and these areas were migrated to the best possible correction while investing a reasonable amount of time. Other areas which proved difficult to migrate were places where seabed or peg-leg multiples were obscuring the M-reflector. Typically, the seabed multiple will migrate at ~1500 m/s and the M-reflector at ~2100 m/s. If the migration velocity for the M-reflector is chosen, the multiple is often overmigrated and diffraction "smiles" can creep upwards to obscure primary reflections in the P-Q succession. These cases were few as the multiple generally occurred much higher in shallow water with similar velocities to nearby primaries or the multiple was sufficiently removed by deconvolution.

3.7 Additional multiple attenuation

The f-k multiple attenuation method was attempted to suppress the seabed and salt layer multiples that remained after deconvolution on the seismic reflection profile that was processed from the Outer Cilicia Basin (i.e. the SW portion of line 30; Fig. 3.1). Here, the high amplitude, highly irregular salt layer multiple was difficult to remove with the method of iterative predictive deconvolution described above. The f-k multiple

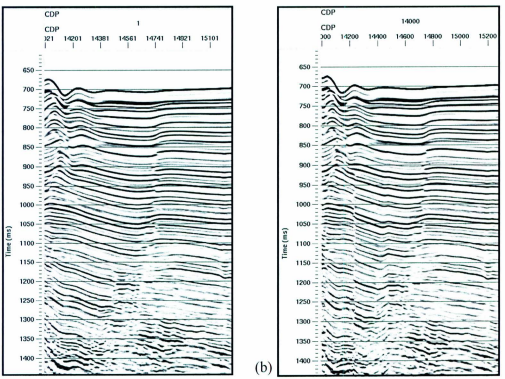

Figure 3.19 A series of two iterations of Kirchoff time migrations at an area that was difficult to migrate properly. The second iteration of migration velocities sharpened the fault planes at the left side of each section. The fault plane to the middle of each section was difficult to migrate and required an anomalously high migration velocity. A balance had to be found between collapsing the diffraction hyperbolae of this fault plane, while migrating the surrounding reflections properly.

(a)

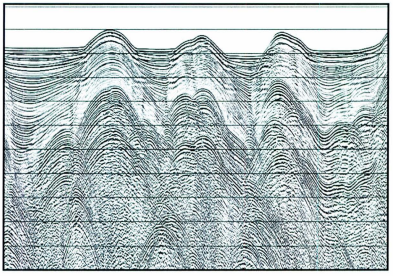

(b)

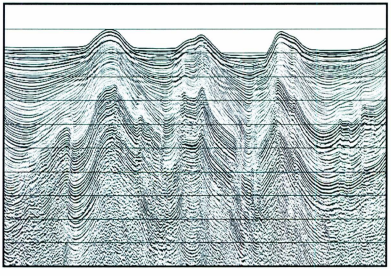

Figure 3.20 A section from the mid-portion of line 30 (a) before and (b) after migration. The diffraction hyperbolae are collapsed in the migrated section and reflections are moved down-dip to their true location in the subsurface.

attenuation method works by exploiting the discrimination in velocity between primaries and multiples. A false velocity function was chosen every 13 CDPs with picks that resulted in the primary reflections being overcorrected and the multiple reflections being undercorrected (Fig. 3.21). When the resultant model is transformed to f-k space the primary energy maps to one quadrant and the multiple energy maps to another. Next, an f-k filter was applied to effectively zero the quadrant containing the multiple energy. The result was a small, barely perceptible attenuation of multiple energy. For the time invested in picking a velocity function at every thirteenth CDP, there was not enough of an improvement on the stacked section to attempt it on any of the other lines. The failure of this process on this particular line was likely due to the relatively short streamer length and therefore small moveout difference between primaries and multiples at this water depth. Another factor in the decision not to use this on other lines was that in areas where short-period multiples reverberated down through the section, the difference in velocities between primary and multiple is minute and an application of the f-k filter described above would likely have caused a loss in primary reflection signal.

3.8 Final display parameters

Final images were generated by the processing program Starpak© and are displayed with a Butterworth frequency filter (allowed bandwidth ~40-200 Hz), AGC and an adjacent trace sum of four traces. Interpreted versions of the lines highlighted in Figure 3.1 are presented as plates in the attached pocket at the back of this thesis. Scales and vertical exaggerations are given on the seismic reflection profiles.

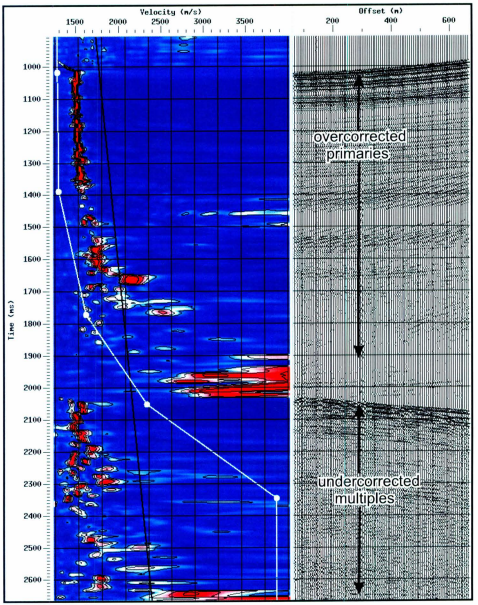

Figure 3.21 Demonstration of the picks used to create the false velocity function for f-k multiple attenuation. The primary reflections beginning at ~1000 ms are overcorrected and the multiple reflections beginning at ~2000 ms are undercorrected, resulting in the energies being mapped onto two separate quadrants in f-k space.

CHAPTER 4: SEISMIC STRATIGRAPHY AND CHRONOLOGY

Three seismic stratigraphic units are identified for the purposes of this study (Units 1-3; see Figs. 4.1, 4.2). The ages of Units 1 to 3 are established by ties to two exploration wells in the Inner Cilicia Basin, Seyhan-1 and Karataş-1 (Turkish Petroleum Corporation, unpublished data), whose location is given in Figure 4.3.

4.1 Seismic stratigraphy

4.1.1 Unit 1: Pliocene-Quaternary

Unit 1 consists of high frequency, high amplitude reflections, which are continuous and can be traced laterally across the study area (Fig. 4.2). Data from exploration wells Seyhan-1 and Karataş-1 show that Unit 1 is composed mainly of siliciclastic sediments and is Pliocene-Quaternary in age (Turkish Petroleum Corporation, unpublished data). Previous studies report that the architecture of Unit 1 in the southern Adana and Inner Cilicia Basins is that of a thick prograded wedge of deltaic sediment mainly originating from the perennial Göksu, Seyhan and Taurus Rivers (Aksu, 1992a). Unit 1 is further subdivided into Quaternary (Unit 1a), Late Pliocene-Quaternary (Unit 1b) and Early Pliocene (Unit 1c) subunits. Units 1a and 1b are tentatively correlated with the onland Kuranşa Formation of the Cilicia Basin's onland extension, the Adana Basin (Yalçın and Görür, 1984; Aksu et al., 2005a; Burton-Ferguson et al., 2005) and the Erzin Formation of the Latakia and Iskenderun Basins (Kozlu, 1987; Yılmaz et al., 1988; Uffenorde et al., 1990; see Fig. 4.4). In the deeper portion of the Cilicia Basin, a predominantly transparent package with weakly reflective and discontinuous parallel

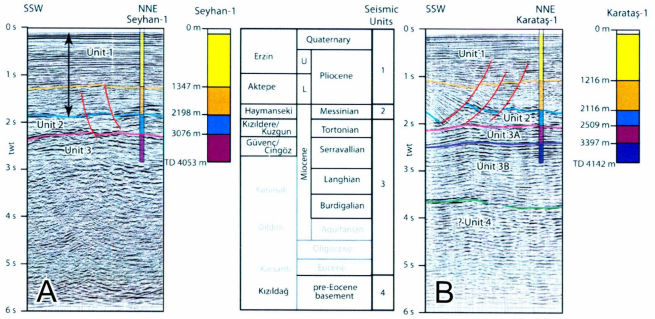

Figure 4.1 Schematic diagram showing the lithologies encountered in the exploration wells Seyhan-1 and Karataş-1 and their correlations with onland formations in the Iskenderun Basin (modified from Aksu et al., 2005). Profiles A and B demonstrate the correlation of Units 1-3 with industry seismic reflection profiles. The locations of seismic reflection profiles A and B are given in Figure 4.3.

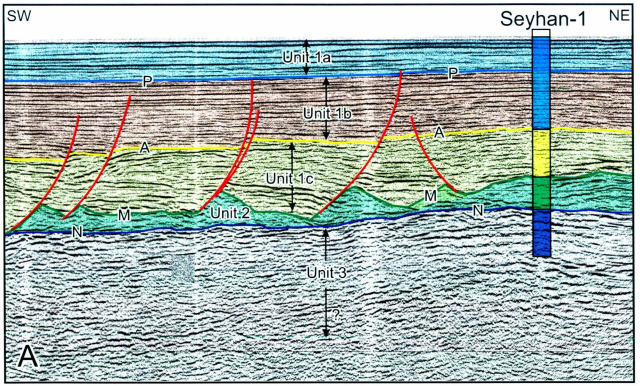

Figure 4.2 The northeastern portion of an industry multi-channel seismic reflection profile (Profile A) highlighting stratigraphic Units 1-3 bounded by the P-, A-, M- and N-reflectors, discussed in text. The location of the Seyhan-1 exploration well and its recovered stratigraphic units used to develop the chronology in the area is also given (Turkish Petroleum Corporation, unpublished data). Locations are shown in Fig. 4.3.

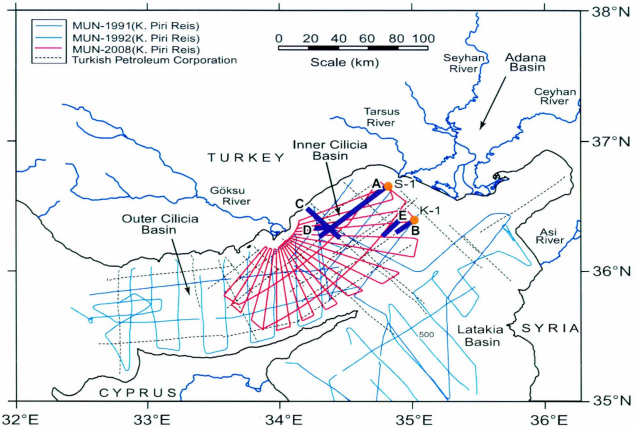

Figure 4.3 Location map showing the exploration wells Seyhan-1 (S-1) and Karataş-1 (K-1) and the seismic reflection profiles used in the establishment of the chronology in the study area. Locations of seismic reflection profiles A, B, C, D and E - discussed in text - are highlighted in purple.

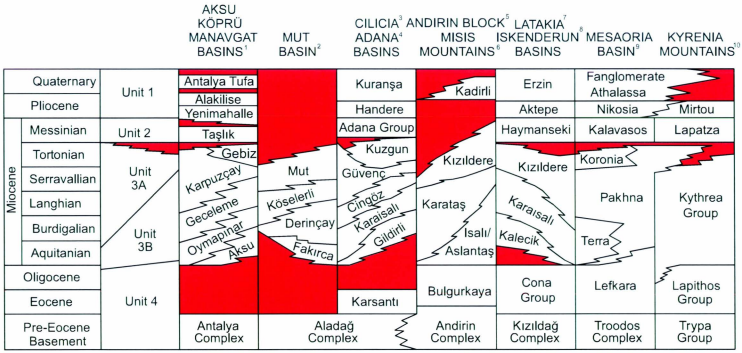

Figure 4.4 Stratigraphy of the Cilicia Basin showing the correlations between seismic stratigraphic units and the sedimentary successions on land and exploration wells complied using (1) Akay and Uysal, 1985; Akay et al., 1985; Karabıyıkoğlu et al., 2000; (2) Bassant et al., 2005; (3) Turkish Petroleum Corporation, unpublished data; (4) Yalçın and Görür, (1984) and Kozlu (1987); (5) Kozlu (1987) and Yılmaz et al. (1988); (6) Gökçen et al. (1988) and Yılmaz et al. (1988); (7) Kozlu (1987), Yılmaz et al. (1988) and Uffenorde et al. (1990); (8) Kozlu (1987), Yılmaz et al. (1988) and Uffenorde et al. (1990); (9) Robertson et al. (1995); (10) Weiler (1969), Cleintaur et al. (1977) and Robertson et al. (1995). Figure modified from Aksu et al. (2005).

reflections occurs within Unit 1c (Fig. 4.2, 4.5). Unit 1c is correlated with the Early Pliocene Handere Formation of the Cilicia and Adana Basins (Yalçın and Görür, 1984), the Aketepe Formation of the Latakia and Iskenderun Basins (Kozlu, 1987; Yılmaz et al., 1988; Uffenorde et al., 1990), the Mirtou Formation of the Kyrenia Range (Robertson and Woodcock, 1986) and the slumped marls of Unit IV in Deep Sea Drilling Project Site 375 (Hsü et al., 1973, 1978) – see Fig. 4.4. The base of Unit 1 is marked by a distinct low frequency, but high amplitude reflection that represents an angular unconformity. This surface has been identified in the eastern Mediterranean as the "M-reflector" (Fig. 4.2, 4.5; Ryan, 1969). The boundaries between each of these three subunits are marked by moderately strong reflections that can be carried across the study area. Herein, the boundary between the Quaternary subunit (i.e. Unit 1a) and the Late Pliocene-Quaternary subunit (i.e. Unit 1b) is referred to as the "P-reflector" and the boundary between the Late Pliocene-Quaternary subunit (i.e. Unit 1b) and the Early Pliocene subunit (i.e. Unit 1c) is referred to as the "A-reflector" (Figs. 4.2, 4.5).

A detailed isopach map was drawn to demonstrate the variation in thickness of Unit 1 across the study area. The isopach map was drawn using depth-converted seismic reflection profiles (see Chapters 2 and 6 for details). Reflections originating from the seabed and the Pliocene-Miocene boundary (i.e. the M-reflector) were carried across each profile using Landmark's Seisworks seismic interpretation software. The study area was divided into a series of equally sized cells and the various thicknesses were averaged in these cells. The software interpolated the reported thickness values between profiles based on the chosen cell size. Because the line spacing was fairly large in some areas, it was necessary to choose a cell size that could accommodate a reasonable interpolation in

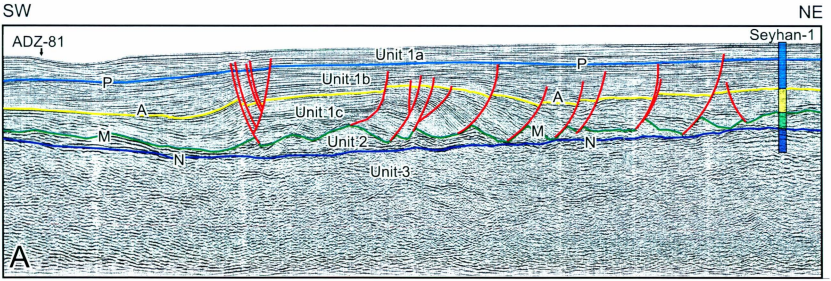

Figure 4.5 Industry multi-channel seismic reflection profile A (ADZ-90) showing the lateral continuity of the P-, A-, M- and N-reflectors. This particular profile was also used to correlate these reflectors across the study area in the establishment of the chronology.

these regions. The optimal cell size was chosen to be approximately half that of the largest line spacing (cell spacing = 2500 m), which seemed to be sufficient in expressing trends in the data, rather than creating too many bulls-eyes. The interpretations and grids were then transferred to Petrosys where detailed mapping was carried out. The resulting isopach map, shown in Figure 4.6, illustrates that Unit 1 is thickest (~2400 m) towards the center of the Inner Cilicia Basin, immediately seaward of the present-day mouths of the Göksu, Seyhan and Taurus Rivers. The region of maximum sediment thickness is somewhat elongated in the NE-SW direction following the central axis of the Inner Cilicia Basin. The unit rapidly thins as it approaches the Misis-Kyrenia Range in the southeast and toward the southwestern Turkish coast.

4.1.2 Unit 2: Miocene (Messinian)

Unit 2 is composed of a weakly reflective package with discontinuous reflections in the study area (Figs. 4.2, 4.5). In the Outer Cilicia Basin, Unit 2 becomes more clearly stratified with discrete continuous reflections that have a corrugated geometry (Aksu et al., 2005a; Piercey, 2011). Correlations with industry exploration wells Seyhan-1 and Karataş-1 show that Unit 2 is Messinian in age and is composed predominantly of evaporitic sediments consisting of halite, anhydrite and gypsum, with frequent interbeds of minor siliciclastic sediment (Turkish Petroleum Corporation, unpublished data). This unit is tentatively correlated with the onland Adana Formation of the Adana Basin (Yalçın and Görür, 1984; Kozlu, 1987), the Haymanseki Formation of the Latakia and Iskenderun Basins (Kozlu, 1987; Yılmaz et al., 1988; Uffenorde et al., 1990), the Lapatza Formation of the Kyrenia Mountains (Weiler, 1969; Cleintaur et al., 1977; Robertson et al., 1995) and the Kalavasos Formation of the Mesaoria Basin (Robertson et al., 1995 -

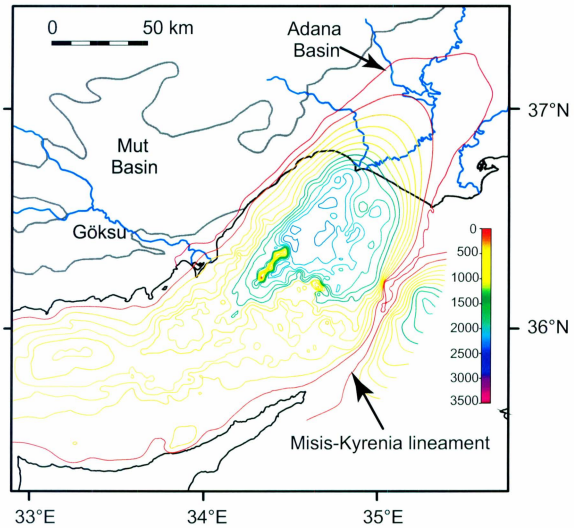

Figure 4.6 Isopach map of the total Pliocene-Quaternary successions (i.e. Unit 1). Contours are drawn every 200 m and have been calculated using depth-converted multi-channel seismic reflection profiles (see Chapter 6).

see Fig. 4.4). Unit 2 is marked by its strongly reflective top (M-reflector) and its weakly reflective and more discontinuous base. The base is a regionally correlatable unconformity that is referred to as the "N-reflector" (Figs. 4.1, 4.2, 4.5; Asku et al., 2005a,b; Hall et al., 2005a,b). Previous studies show that Unit 2 is either missing or very thin near the Misis-Kyrenia horst block (e.g. Mulder, 1973), the southern flanks of the Kyrenia Range and the Turkish margin of the basin complex (Aksu et al., 2005a). The N-reflector is either poorly imaged or totally absent in the 2008 Inner Cilicia Basin seismic reflection profiles due to shallow water reverberations obscuring later reflections and penetration depths that do not reach to the base of Unit 2 in areas of thick Pliocene-Quaternary sedimentation.

4.1.3 Unit 3: Miocene (pre-Messinian)

Unit 3 lies beneath the Messinian evaporites of Unit 2 when present. This unit is difficult to observe in the available seismic reflection profiles due to complexities in sub-salt imaging and thus is not able to be correlated across long distances. Furthermore, Unit 3 is never adequately imaged in the 2008 seismic data due to shallower penetration depths and multiple energy masking later reflections. Nonetheless, data from exploration wells show a thick package of fluvio-deltaic successions of Tortonian age is present in the Inner Cilicia Basin, comprising Unit 3 (Uffenorde et al., 1990; Turkish Petroleum Corporation, unpublished data). Unit 3 is further subdivided into two major seismic stratigraphic subunits. The upper subunit (Unit 3a) is composed of a series of low-frequency rhythmic reflections that have moderate lateral continuity. Unit 3a is tentatively correlated with the Kuzgun Formation of the Adana and Inner Cilicia Basins (Yalçın and Görür, 1984; Turkish Petroleum Corporation, unpublished data), the

Kızıldere Formation of the Misis Mountains (Gökçen et al., 1988; Yılmaz et al., 1988) and the Latakia and Iskenderun Basins (Kozlu, 1987; Yılmaz et al., 1988; Uffenorde et al., 1990), the Koronia Formation of the Mesaoria Basin and the Kythrea Group of the Kyrenia Mountains (Weiler, 1969; Cleintaur et al., 1977; Robertson et al., 1995; also see Fig. 4.4). It is important to note that the equivalent marine successions to Unit 3a in the Inner Cilicia Basin are represented by the Köseleri Formation of the Mut Basin: the latter is presently perched at ~2000 m elevation over the Central Taurus Mountains (Bassant, 2005; Fig. 4.4). A similar scenario occurs in the onland Aksu, Köprü and Manavgat Basins where marine sediments equivalent to Unit 3a are represented by the Gebiz and Karpuzçay Formations (Akay and Uysal, 1985; Akay et al., 1985; Karabıyıkoğlu et al., 2000; Fig. 4.4). The base of this subunit is a more prominent but discontinuous reflection that represents an unconformity within the study area (Fig. 4.1, Turkish Petroleum Corporation, unpublished data).

Unit 3b is composed of higher frequency, fairly continuous reflections. The base of this unit is not clearly observed, but a similar seismic character can be observed extending downward over 1 second. Exploration well data show that Unit 3b is mainly composed of Middle Miocene turbidite successions (Turkish Petroleum Corporation, unpublished data). The base of this unit may include the Aquitanian to Serravallian Karaisalı Formation, identified in exploration wells in the Adana Basin (Yalçın and Görür, 1984; Burton et al., 2005) and in the Iskenderun and Inner Latakia Basins (Uffenorde et al., 1990). It can be correlated with the turbiditic successions of the Güvenç and Cingöz formations of the Adana Basin (Fig. 4.4), which constitute the main part of mega-sequence 2 of Williams et al. (1995), as well as with the Karataş/Isalı-

Aslantaş formations of the Misis Mountains (Kelling et al., 1987) and the Kythrea Group of the Kyrenia Range (Weiler, 1969; Robertson and Woodcock, 1986 – also see Fig. 4.4). The marine successions of Unit 3b are also observed in the Mut Basin over the Central Taurus Mountains and can be correlated with the Early Miocene Mut, Derinçay and Fakırca Formations (Bassant, 2005; Yılmaz, 1988; Fig. 4.4). Subunit 3b is further correlated with the Geceleme, Oympınar and Aksu Formations of the onland Aksu, Köprü and Manavgat Basins (Akay and Uysal, 1985; Akay et al., 1985; Karabıyıkoğlu et al., 2000; Fig. 4.4).

4.2 Chronology of the seismic stratigraphic units

The chronology of the three seismic units identified in the Inner Cilicia Basin and described above is established though correlations with two exploration wells drilled in the Inner Cilicia Basin by the Turkish Petroleum Corporation; Seyhan-1 and Karataş-1 (Figs. 4.1, 4.3). The Seyhan-1 well was drilled in the western and shallower portion (~40 m water depth) of the Inner Cilicia Basin. It encountered ~2158 m of Pliocene-Quaternary deltaic and pro-deltaic successions (Turkish Petroleum Corporation, unpublished data). On the basis of biostratigraphic and lithostratigraphic data from the well, the Pliocene-Quaternary succession was further divided into a 1307 m-thick upper subunit and an 851 m-thick lower subunit separated by the A-reflector (Figs. 4.1, 4.2). The base of the Pliocene-Quaternary successions was marked by a major erosional unconformity, which is correlated with the regional M-reflector. An 878 m-thick, predominantly evaporitic unit, consisting of halite, anhydrite, gypsum with frequent interbeds of minor siliciclastic and carbonate debris is identified below the unconformity: this unit is correlated with the Messinian evaporite succession (Fig. 4.1). The base of the

evaporitic unit is also delineated by a major unconformity (i.e. represented by the N-reflector). The well further encountered ~977 m of Tortonian age siliciclastic and carbonoclastic successions and terminated within the upper Miocene at a depth of 4053 m.

Karataş-1 well was drilled further southeast and seaward of the Seyhan-1 well in 74 m water depth (Figs. 4.1, 4.3) near the Misis-Kyrenia fold-thrust belt that extends from the Kyrenia Mountains of northern Cyprus to the Misis Mountains of southern Turkey (Turkish Petroleum Corporation, unpublished data). The well encountered a sequence of sedimentary successions similar to those observed in the Seyhan-1 well, including ~2116 m-thick Pliocene-Quaternary siliciclastics, 393 m-thick Messinian evaporites, ~888 m-thick Tortonian and ~745 m-thick Middle Miocene (?Langhian-Serravallian) successions (Fig. 4.1; Turkish Petroleum Corporation, unpublished data).

The depths of the sedimentary successions observed in the exploration wells are correlated with the two-way-time industry seismic reflection profiles using the velocity information provided by the Turkish Petroleum Corporation (Fig. 4.1). Only the industry seismic reflection profiles were used to establish the chronology across the study area because the 2008 MUN seismic reflection data that were collected in the innermost shallow-water region of the Inner Cilicia Basin were highly reverberatory and lack the deep penetration needed to observe the Pliocene-Quaternary and Miocene markers, such as the base Messinian and Tortonian (Figs. 4.5, 4.7). Close examination of the seismic reflection profiles and the well data showed that all major biostratigraphic markers identified in the exploration wells by the Turkish Petroleum Corporation corresponded within ±30 ms with acoustically strong and laterally continuous reflections in the industry

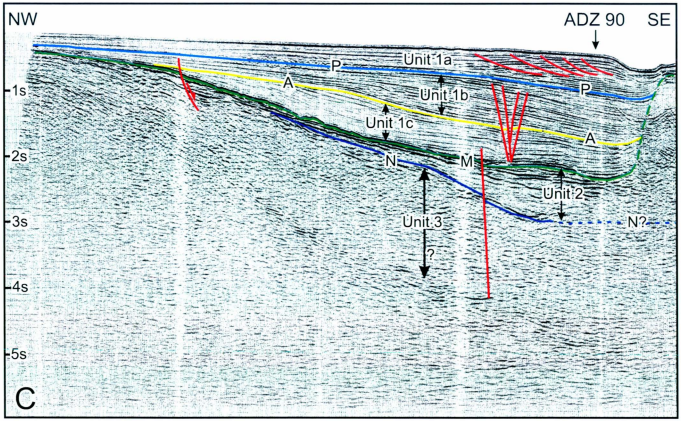

Figure 4.7 Industry multi-channel seismic reflection profile C displaying the crossover with the industry profile A shown in Fig. 4.5 and the correlation of the P-, A-, M- and N-reflectors used to establish the chronology in the study area. Location is given in Figure 4.3.

profiles. For example, the top and base of the Messinian evaporite successions (i.e. Unit 2) correlated with strong seismic markers, referred to in the eastern Mediterranean region as the M- and N-reflectors (Ryan, 1969; Aksu et al., 2005a,b).

Ages were assigned to each marker horizon on the basis of the correlations of the biostratigraphic data available from the industry well data with the seismic reflection profiles. The M-reflector separates the lowermost Pliocene sediments from the uppermost Miocene evaporite deposits. The age of desiccation of the Mediterranean Sea and the development of the M-reflector is said to occur at 5.3 Ma at the Messinian – Pliocene boundary (Ryan, 1969). It is important to note here that the well data are mute regarding how much of the Messinian strata are missing in the wells. The well data are also mute regarding the timing of initiation of the Pliocene sedimentation in the Cilicia Basin following the Messinian Salinity Crisis (e.g., Hsü et al., 1978; Bridge et al., 2005; Cosentino et al., 2012). Because the M-reflector is a major erosional unconformity and the Turkish Petroleum Corporation well data lack the biostratigraphic details about the Messinian evaporite successions, the age of the underlying Messinian sediments is not known. However, previous studies as well as this dissertation showed that the Pliocene-Quaternary Unit 1 unconformably overlies the M-reflector in many eastern Mediterranean basins (if not all). This unit is characterized by a 2-3 seconds-thick delta succession (also see Aksu et al., 2005a). Seismic reflection profiles studied in this dissertation show no evidence for major interruptions in sedimentation within the Pliocene-Quaternary Unit 1. Therefore, for the purpose of various calculations, such as broad sedimentation rates, regional subsidence rates and delta accumulation rates, the base of Pliocene is assumed to be 5.3 Ma. The A-reflector is correlated with the

sediments dated in the exploration wells as the transition between the Early and Late Pliocene and therefore is assigned an age of 3.6 Ma.

Two additional markers in the upper portion of Unit 1 were identified for the purposes of this study. The first of these markers is referred to as the Q-reflector, which defines the base of a marked delta progradational package mainly mapped in the Inner Latakia and eastern Inner Cilicia Basins (Aksu et al., 1992a,b). Using shallow penetration seismic profiles these authors correlated approximately eleven prograded delta packages with global oxygen isotope stratigraphy and determined that the base of the seventh oldest delta most likely developed during the glacial isotopic stage 16 (Fig. 4.8), dated at ca. 621 ka (Lisiecki and Raymo, 2005). This age assignment is tentative and uses the assumption that the correlation of the seismic stratigraphic packages can be readily matched with the global oxygen isotopic stages. The second prominent reflection marks the top of a particular prograded delta package that was traced across the study area; this reflection is referred to as the "P-reflector". The depth migrated multi-channel seismic reflection profiles (see Chapter 6 for detail on depth conversions) were used to assign an age estimate to the P-reflector. As noted above, seismic reflection profiles studied in this dissertation show no evidence for major interruptions in sedimentation within the Pliocene-Quaternary Unit 1 in the deep portion of the Inner Cilicia Basin. The absence of intra-unit unconformities and the very thick package at the deepest portion of the basins characterized by parallel reflections strongly support the validity of using linear interpolation between the Q- and the P-reflectors as a reasonable method for estimating an age for the P-reflector. To determine the age of the P-reflector a constant rate of sedimentation was assumed in the interval between global isotopic stage 16 (i.e.

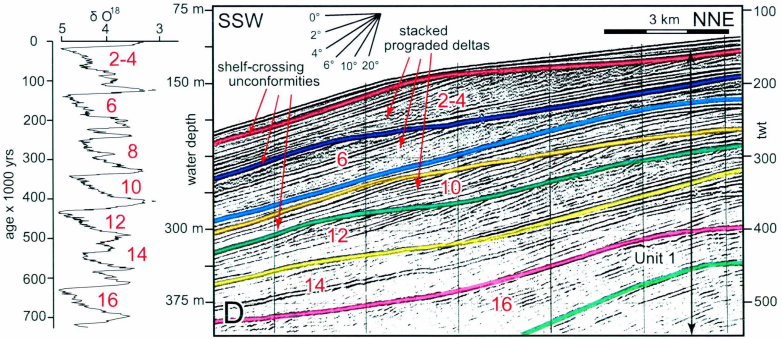

Figure 4.8 Single channel seismic reflection profile D showing the internal architecture of several vertically stacked prograded delta packages in Inner Cilicia Basin (re-drawn from Aksu et al., 1992a). Note that each prograded delta package is separated from the other by major shelf-crossing unconformities. Also shown is the global oxygen isotopic curve (δ18O) from Lisiecki and Raymo (2005) and the correlation of the stacked prograded delta packages and the global oxygen isotopic curve. Red even numbers represent global glacial intervals when the deltas prograded seaward. The Q-reflector corresponds with the top of stage 16, outlined in pink. Location is shown in Figure 4.3.

Q-reflector) and the P-reflector. The analysis was conducted at multiple locations to determine an average age for the P-reflector of ~1.9 Ma. Figure 4.9 shows an example of a location in the depth converted seismic reflection profiles where the age approximation was conducted.

Although determining the rates of sedimentation in various intervals is an objective of this study, in the absence of more detailed well data the method of linear interpolation in the relatively short time period between the Q- and P-reflectors gives the best approximation for an age for the P-reflector. The Q-reflector was not traced throughout the entire study area and was used solely to determine the age of the P-reflector. These markers, although tentative, provide additional anchoring points in the chronostratigraphy of the Inner Cilicia Basin.

The three dated markers, the M-, A- and P-reflectors, are correlated across the study area using two key industry seismic reflection profiles, ADZ 90 and ADZ 81 (Figs. 4.5 and 4.7, respectively). The tracing of the M-reflector was straightforward because as the salt migrated to the footwall and hanging wall of prominent listric extensional faults the evaporitic successions of Unit 2 created a prominent series of salt rollers across the floor of the Inner Cilicia Basin (see Chapter 5). In some areas of thick sediment cover where peg-leg multiples covered the M-reflector, tracing the M-reflector was somewhat difficult and its position was chosen based on the cross-overs with deeper penetration industry profiles. The tracing of the A-reflector proved to be more challenging, as the reflector had to be carried across a number of listric normal faults. To accomplish this, paper copies of the seismic profiles were printed, and the A-reflector was carried across the profiles until a major fault was encountered. Here the A- reflector was carried to its

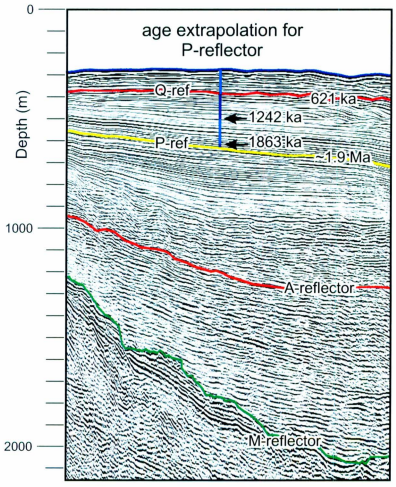

Figure 4.9 An example of a location where the age of the P-reflector was found using a linear interpolation between the Q- and P-reflectors. This same procedure was conducted at multiple locations to determine an average age of 1.9 Ma for the P-reflector.

termination at the footwall of a fault and the paper copies were then cut along the fault plane. The acoustic characteristics of a bundle of reflectors, which included the A-reflector, on the footwall block of the fault were compared and matched with those on the hanging wall block. The acoustic characteristics that made the position of the A-reflector clear included reflector frequency, amplitude and lateral continuity within the bundle. This type of correlation is colloquially known as "jump correlation" (see Chapter 2). The method was successful and the A-reflector was confidently carried across each major listric fault to the western margin of the Inner Cilicia Basin, east of the present-day Göksu River where several stacked prograded delta packages of the ancestral Göksu delta occur. The P-reflector generally occurred above the tip points of the aforementioned listric faults and could be carried across the study area very easily. In regions where the P-reflector had to cross major subsurface features, such as salt diapirs and faults, the method of "jump correlation" was employed.

In summary, the data presented in this chapter allowed for the firm dating of two prominent reflections that were traceable across the entire study area: the M-reflector (5.3 Ma) and the A-reflector (3.6 Ma). The top of a Quaternary prograded delta package (i.e. the P-reflector) was also carried throughout the study area and was assigned a more tentative age of 1.9 Ma. These two firmly dated markers (M- and A-reflectors) and one tentatively dated marker (P-reflector) are critical for later discussion regarding the analysis of sedimentary volumes to determine sedimentation rates by the Göksu River during the Pliocene-Quaternary (see Chapters 6 and 7).

CHAPTER 5: STRUCTURAL GEOLOGY

In this chapter the structural architecture of only the Inner Cilicia Basin is described, because the structural and sedimentary evolutions of the Outer and central Cilicia Basins constitute the core of two other MSc theses by Piercey (2011) and Kurtboğan (in progress).

5.1 Structural architecture of the Inner Cilicia Basin

The Pliocene-Quaternary structural architecture of the Inner Cilicia Basin can be described using three morpho-tectonic domains: (1) the northwestern margin (Kozan Fault Zone), (2) the southeastern margin (Misis-Kyrenia Fault Zone) and (3) the extensional fault fan (Fig. 5.1).

Domain 1: northwestern margin of Inner Cilicia Basin: the Kozan Fault Zone

The western margin of the Inner Cilicia Basin is delineated by a zone of broadly NE–SW-trending dominantly SE-dipping extensional faults (Fig. 5.2). The zone is characterized by several closely spaced high-angle faults that show small dip separations (<50 ms) on the M-reflector and have tip points extending mainly into the middle portion of the Pliocene-Quaternary succession (Figs. 5.3, 5.4). Occasionally, some of these narrowly spaced high-angle faults show tip points extending into the seabed where they create small steps on the seafloor (Fig. 5.5). The eastern margin of the fault zone is marked by a narrow zone of SE-dipping listric faults which sole in the Messinian evaporite succession and show 150-200 ms dip separations on the M-reflector: this fault is best imaged in the deeper penetration industry seismic reflection profiles (Fig. 5.6). This zone shows a steeply dipping root within the pre-Messinian basement, extending

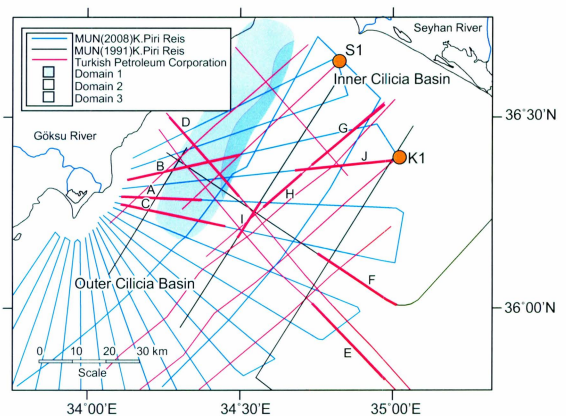

Figure 5.1 The map of the Inner Cilicia Basin showing the three morpho-tectonic domains and the seismic reflection profile data used in this study. Domain 1: the northwestern margin of the Inner Cilicia Basin, the Kozan Fault Zone; Domain 2: the southeastern margin of the Inner Cilicia Basin, the Misis-Kyrenia Fault Zone and Domain 3: the extensional fault fan situated between Domains 1 and 2. S-1 and K-1 are exploration wells Seyhan-1 and Karataş-1, respectively. Seismic profiles discussed in text are highlighted in pink and labelled alphabetically.

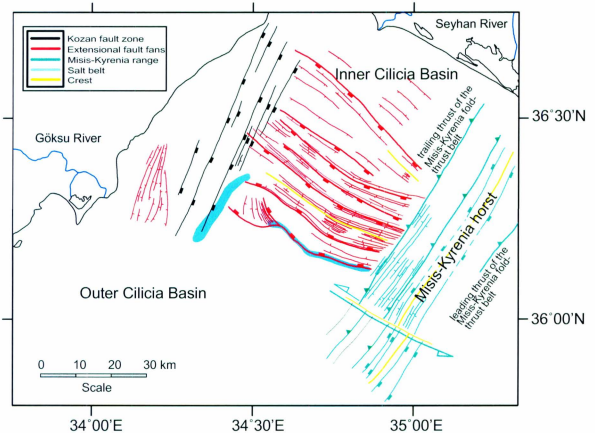

Figure 5.2 Detailed structural map of the Inner Cilicia Basin, showing the Kozan Fault Zone in the northwest, the Misis Kyrenia Fault Zone in the southeast and the extensional fault fan in the middle. Extensional faults are shown as lines with rectangular tick on hanging walls, whereas reverse faults and thrusts are shown as lines with triangular ticks on hanging walls.

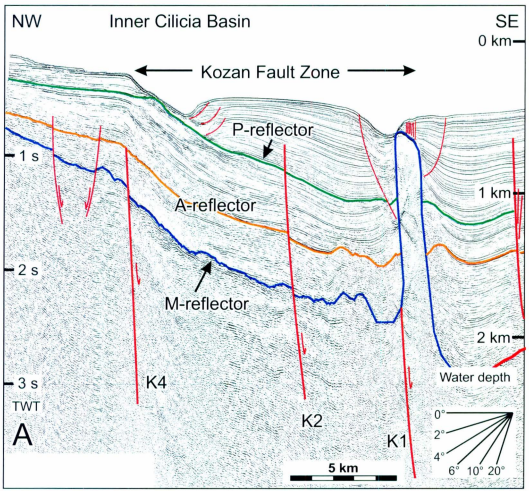

Figure 5.3 Multi-channel seismic reflection profile A showing the structural and stratigraphic architecture of the northwestern margin of the Inner Cilicia Basin. Three prominent reflections are highlighted: the M-reflector and the intra-Unit 1 A-and P-reflectors, discussed in text. Note that several closely-spaced high-angle faults create minor offsets on the M-reflector. Also note that most of these faults have tip points extending into the lower to middle portion of the Pliocene-Quaternary succession of Unit 1. Location is shown in Figure 5.1. Depths at right assume a constant velocity of 1500 m/s.

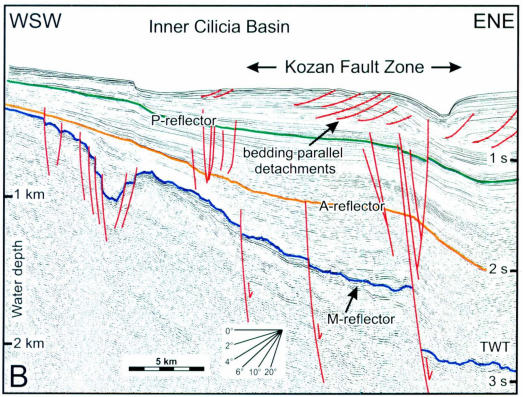

Figure 5.4 Multi-channel seismic reflection profile B showing the structural and stratigraphic architecture of the northwestern margin of the Inner Cilicia Basin, including the M-, A- , and P-reflectors, discussed in text. Note that several closely-spaced high-angle faults create minor offsets on the M-reflector, with tip points extending into the lower to middle portion of the Pliocene-Quaternary succession of Unit 1. Also note the presence of several near-bedding-parallel detachment surfaces in the upper portion of the profile. Location is shown in Figure 5.1.

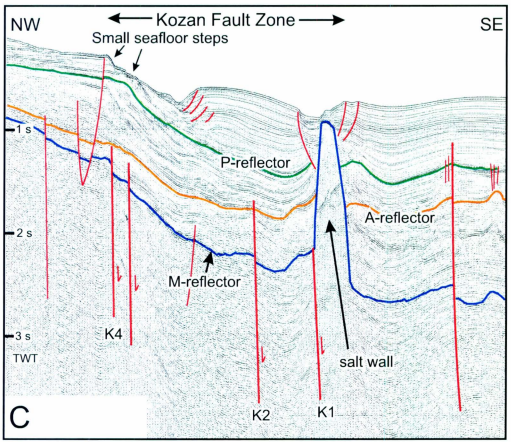

Figure 5.5 Multi-channel seismic reflection profile C showing the structural and stratigraphic architecture of the northwestern margin of the Inner Cilicia Basin, including the M- , A- and P-reflectors, discussed in text. Note that occasional faults create small steps on the seafloor. Also note the large salt wall that partitions the Inner Cilicia Basin. Location is shown in Figure 5.1.

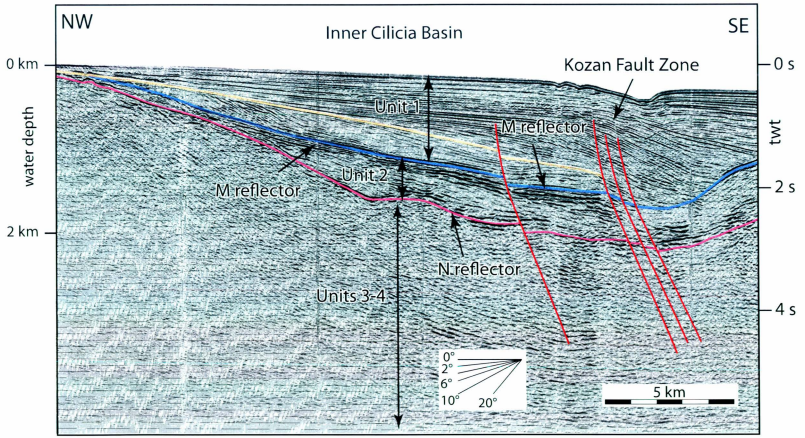

Figure 5.6 Industry multi-channel seismic reflection profile showing the SE-dipping listric normal faults that bound the eastern margin of the Kozan Fault Zone. Location is shown in Figure 5.1. Depths at left assume a constant velocity of 1500 m/s.

well below 2500 ms in most seismic profiles (Fig. 5.6). Aksu et al. (2005) also described this fault as a listric SE-dipping extensional fault with 100-200 ms dip separation on the M-reflector. The westernmost margin of the fault zone, east and southeast of the present-day Göksu delta, is also a prominent feature where a smaller fault creates a 100-150 ms step on the seafloor, marking the shelf edge (Figs. 5.2-5.5). This fault was previously described by Evans et al. (1978) as one of the terraces that fringe the southern Turkish margin. Towards the northeast this fault zone loses its seafloor expression as it becomes progressively buried under the Pleistocene deltaic successions of the Göksu River entering the basin from the west and the Seyhan, Ceyhan and Tarsus Rivers from the north. But, the fault(s) that define the northwestern margin of the Kozan Fault Zone can still be traced in the seismic reflection profiles as a prominent NE-SW trending SE-dipping extensional fault zone marking the western and northwestern margin of the innermost Cilicia Basin. Here, the fault exhibits 150-250 ms extensional separations on the M-reflector, and growth in both the Messinian and Early Pliocene successions associated with roll-overs on E-dipping listric fault segments (e.g., Fig. 5.6). Further to the northeast, near the northern limit of exposure of the Messinian-Recent successions in the Adana Basin, this belt merges with the Kozan Fault Zone (Perinçek et al., 1987; Kozlu, 1987; Aksu et al., 2005). Aksu et al. (2005) argued that the Kozan Fault Zone defines a basin-bounding system that marks the northwest fringes of the onland Adana Basin to the northeast. Detailed examination of a dense grid of seismic reflection profiles shows that the faults of the Kozan Fault Zone display marked increases in extensional separations toward the south. Aksu et al. (2005) also noted this character and suggested that the zone defines a scissor-type extension.

Domain 2: southeast margin of Inner Cilicia Basin: Misis-Kyrenia Fault Zone

The Misis-Kyrenia Fault Zone constitutes the southeastern margin of the Inner Cilicia Basin (Figs. 5.1, 5.2). The zone extends northeast and delineates the southeastern margin of the onland Adana Basin (Aksu et al., 2005). In marine seismic reflection profiles the eastern and southeastern boundary of the Inner Cilicia Basin is delineated by a ~7-10 km wide bathymetric ridge. This structure extends from the southern tip of the Misis Mountains in southern Adana Basin to the northeastern tip of the Kyrenia Range in northeast Cyprus (Figs. 5.1, 5.2; Aksu et al., 2005; Hall et al., 2005). This bathymetric ridge is developed over the crest of a 30-40 km wide, pre-Messinian basement high, interpreted as the erosional remnant of a Late Miocene (Tortonian), SE-verging fold/thrust belt (Aksu et al., 2005; Fig. 5.2). The narrower bathymetric ridge is the expression of a prominent set of basin-bounding faults that developed during the Pliocene-Recent (Aksu et al., 2005). This structure is referred to as the Misis-Kyrenia central horst block (Fig. 5.2; Aksu et al., 1992, 2005).

Aksu et al. (2005) divided the Misis-Kyrenia pre-Messinian basement high into three structural domains: the eastern platform, the western platform and the central horst block (Fig. 5.7). They noted that the eastern and western platforms are entirely situated in the Inner Latakia Basin and Inner Cilicia-Adana Basins, respectively, and that they respectively represent the leading and trailing portions of the pre-Messinian fold/thrust belt. The western platform is a 15-25 km wide zone (Fig. 5.2). In the northern Inner Cilicia Basin it defines a broad erosional high, marked at its top by the M-reflector (Fig. 5.8). Traced from the northwest towards the southeast across the Inner Cilicia Basin, the >2500 ms-thick Pliocene-Quaternary succession progressively onlaps over the slope of

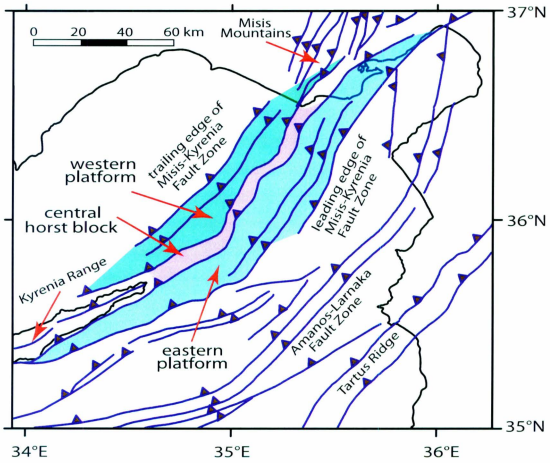

Figure 5.7 Simplified map showing the eastern and western plateforms and the central horst block of the Misis-Kyrenia fold/thrust belt. Structures are from Aksu et al. (2005) and Hall et al. (2005).

the western platform, thinning to a 100-400 ms thick veneer over the crest of the Misis-Kyrenia horst block (Figs. 5.8, 5.9). This veneer is largely composed of the uppermost Pliocene-Quaternary succession (e.g., Fig. 5.9). Limited industry seismic reflection profiles show that the western platform is underlain by a number of east-verging imbricate thrust sheets involving large-scale east-verging fold structures developed in the pre-Messinian Miocene Unit 3 (Fig. 5.8). In this region, the M-reflector defines a prominent angular unconformity truncating the fold structures (Figs. 5.8, 5.9).

The central horst block is a 7-10 km wide zone characterized by several NE-SW trending and NW- and SE-dipping high-angle extensional faults which cut most of the Pliocene-Quaternary strata, creating pronounced steps on the sea-floor (Fig. 5.9). Traced from the Inner Cilicia Basin toward the southeast, the M-reflector sharply rises ~500-1000 ms across the western faults of the central horst block (Fig. 5.9). The Pliocene-Quaternary succession shows a clear southeast-directed onlap, wedging over the western platform. Over the crest of the horst, most of the lower portion of the Pliocene-Quaternary is missing and the upper portion of the sequence is largely condensed (Fig. 5.9). This thinning is accomplished by southeast-directed interstratal onlap and convergence of the Pliocene-Quaternary reflections over the Misis-Kyrenia horst.

Domain 3: the extensional fault fans

Two prominent NW-SE trending and SW- and NE-dipping imbricate fault fans are identified within the Inner Cilicia Basin between the Kozan Fault Zone in the northwest and the Misis-Kyrenia Fault Zone in the southeast (Fig. 5.2). One fan is largely situated in the innermost segment of the Inner Cilicia Basin, immediately south of the present day shoreline. The other is situated further southwest, and extends across the

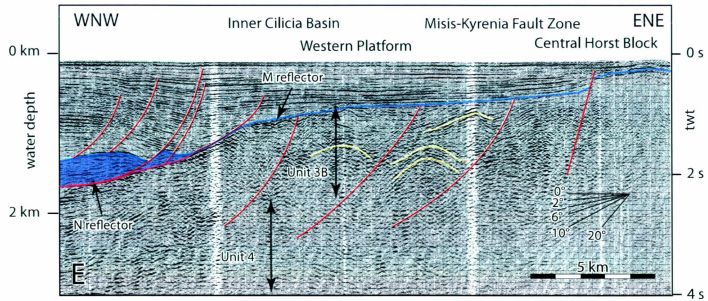

Figure 5.8 Industry multi-channel seismic reflection profile E showing the erosional remnant of the western platforms defining trailing portion of the Misis Kyrenia fold/thrust belt and the central horst block (from Aksu et al., 2005; Hall et al. 2005). Location is given in Figure 5.1. Depths at left assume a constant velocity of 1500 m/s. Vertical lines in the seismic reflection profiles are created by creases on the paper copies that were scanned.

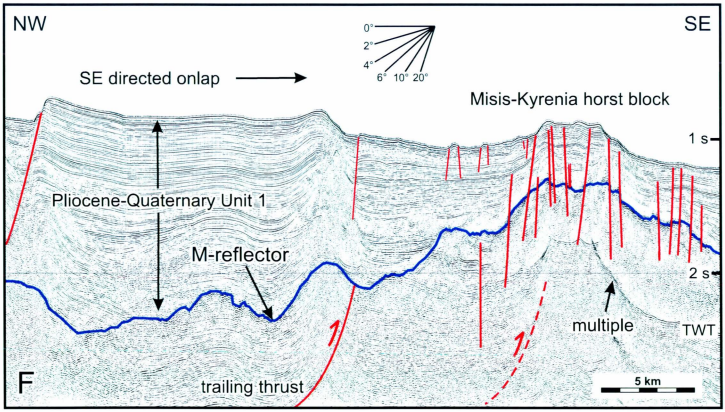

Figure 5.9 NW-SE trending multi-channel seismic reflection profile showing the progressive southeast-directed onlap of the Pliocene-Quaternary succession over the western platform and the thin veneer over the Misis-Kyrenia horst block. Location is given in Figure 5.1.

length of the Inner Cilicia Basin to the major fault zone that defines the boundary between the Inner and Outer Cilicia Basin. The northern fan extends into the onland Adana Basin (Aksu et al., 2005; Ferguson et al. 2005). The northern fan has a cross-sectional width of ~30-35 km (Aksu et al., 2005), whereas the southern fan is much larger with a cross-sectional width of ~50 km (Fig. 5.2). The southern fan is ~90° to both the eastern and western basin-bounding fault systems (Fig. 5.2).

The northern fan is characterized by several NNW-SSE trending and mainly SW-dipping listric extensional faults (Fig. 5.2). The orientation of the faults in the northern fan is ~45° to the southeastern basin-bounding Misis-Kyrenia Fault Zones, but are nearly orthogonal to the western basin-bounding Kozan Fault Zone (Fig. 5.2). The marine seismic reflection profiles across the northern fan display an array of regularly spaced, SW-dipping listric extensional faults that sole into a gently SW-dipping detachment surface, which lies within Unit 2 (Fig. 5.10). The northern edge of this fault fan roughly coincides with the northeastern limit of Unit 2 in the Adana Basin (Burton-Ferguson et al., 2005). Dip separations on individual faults in the fan are consistently small (50-300 ms).

The transition between the northern and southern fans is characterized by a NNW-SSE trending anticline in the north, which is detached at its base within the Messinian evaporite succession and a NW-SE trending syncline in the south (Fig. 5.2; Bridge et al., 2005). The anticline can be traced from the Misis-Kyrenia horst northwest toward the shoreline where it is a very broad and open anticline. The crest of the anticline is dissected by numerous NE- and SW-dipping subsidiary extensional faults (Figs. 5.10, 5.11). The NE-dipping limb of the structure terminates against a prominent SW-dipping

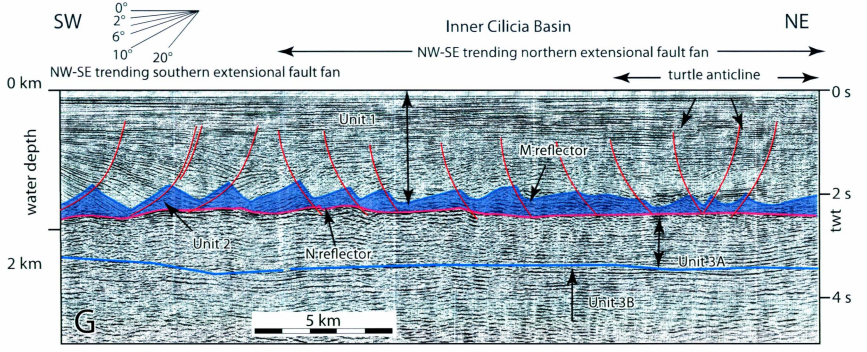

Figure 5.10 Industry multi-channel seismic reflection profile G showing the architecture of the northern extensional fault fan and the boundary between the northern and southern fans. Location is shown in Figure 5.1. Depths at the left assume a constant velocity of 1500 m/s.

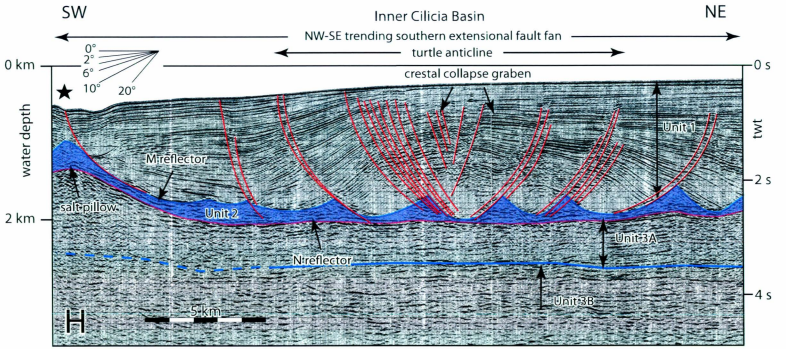

Figure 5.11 Industry multi-channel seismic reflection profile H showing the architecture of the southern extensional fault fan and the master fault that separates the Inner and Outer Cilicia Basins (marked by a star). Location is shown in Figure 5.1. Depths at the left assume a constant velocity of 1500 m/s.

listric extensional fault which shows notable growth in the lower-middle portion of the Pliocene-Quaternary strata. The SW-dipping limb of the anticline terminates against a NE-dipping listric extensional fault. Up-section the fault terminates within an open synclinal structure which shows sediment growth within the Middle Pliocene-Quaternary succession (Figs. 5.2, 5.10, 5.11). This syncline defines the boundary between the northern and southern fans.

The southern extensional imbricate fault fan can be divided into three NW-SE trending zones (Figs. 5.11, 5.12). The northern zone is 10-15 km wide and consists of 5-7 major fault panels separated by SW-dipping listric extensional faults which show tip points within the Late Pliocene-Quaternary succession and display demonstrable sediment growth, largely in the Early-Mid Pliocene (Figs. 5.2, 5.11, 5.12). The fault panels are further dissected by numerous NE-dipping synthetic and SW-dipping antithetic subsidiary extensional faults. These faults sole into a gently SW-dipping (1-3°) detachment surface at the base of the Messinian evaporites of Unit 2 (Fig. 5.11). Above the detachment, the Messinian evaporites are mobilized into wedge-shaped bodies underlying the listric fault surfaces: these structures are best imaged in the industry seismic reflection profiles (Fig. 5.11). The evaporites appear to have penetrated both the footwalls and hanging walls of the listric extensional faults (Fig. 5.11).

The central zone consists of a very prominent fault-controlled anticline, with SW-dipping faults in the northeastern segment of the anticline and NE-dipping faults in the southwestern segment of the anticline (Figs. 5.11, 5.12). The NE-dipping limb of the structure terminates against a prominent SW-dipping listric extensional fault which shows notable growth in the lower-middle portion of the Pliocene-Quaternary strata. The

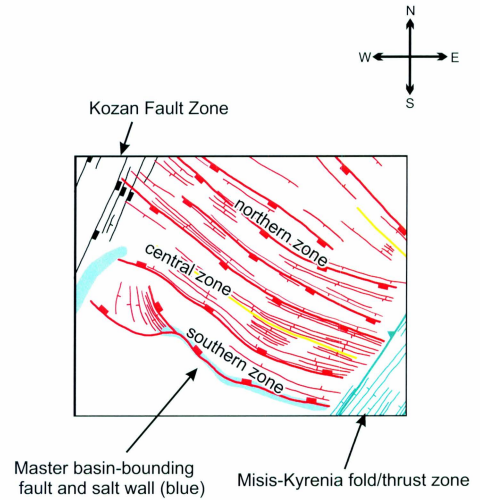

Figure 5.12 Map showing the detailed structural architecture of the southern extensional fault fan and the relationship between the individual faults of the fan and the basin-bounding elements the Kozan Fault Zone in the northwest, the Misis Kyrenia Fault Zone in the southeast. Extensional faults are shown as lines with rectangular tick on hanging walls, whereas reverse faults and thrusts are shown as lines with triangular ticks on hanging walls. The anticline that defines the central zone of the southern extensional fault fan is delineated by a yellow line on the map.

SW-dipping limb of the anticline terminates against a NE-dipping listric extensional fault. The NE- and SW-dipping faults sole into Unit 2 and the anticline is detached at its base within the Messinian evaporites (Figs. 5.11). The development of the structure is associated with large sediment growth, particularly in the Early and Middle Pliocene strata on its northern limb and Late Pliocene to Quaternary strata on its southern limb. Detailed mapping showed that the axis of the anticline gently plunges to the northwest (Figs. 5.2, 5.12). In the northwest, the structure is cored by a prominent salt wedge, situated above the gently S-dipping detachment surface. The crestal region of the structure is dissected by numerous subsidiary extensional faults, which define a well developed crestal collapse graben (Figs. 5.11, 5.12). This anticline is also imaged in single channel seismic profiles and its crest is the site of a major local unconformity (Aksu et al., 1992). This anticline is also mapped by Aksu et al. (2005), who referred to it as the "turtle anticline".

The southern portion of the southern fan is a 9-13 km wide zone consisting of 3-5 prominent NE-dipping listric extensional faults, showing tip points at or near the depositional surface and large sediment growth in the Mid-Late Pliocene-Quaternary strata (Figs. 5.11, 5.12). Similar to the northern portion of the fan, each fault panel is also dissected by numerous NE- and SW-dipping subsidiary extensional faults. These faults also sole into the regional detachment surface and are underlain by wedge-shaped evaporite bodies. Toward the south this regional detachment surface exhibits a concave-up listric trajectory and rises >2000 ms over a distance of 2-5 km, emerging as a prominent master fault at the depositional surface (Figs. 5.11, 5.12, 5.13). Here this fault divides into a number of synthetic and antithetic subsidiary faults, which together form a

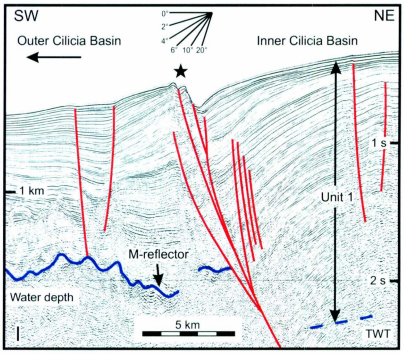

Figure 5.13 Multi-channel seismic reflection profile I showing the architecture of the master basin-bounding fault of the southern extensional fault fan (marked by a star). Note the decrease in thickness of Unit 1 from the footwall to the hanging wall of this fault (i.e. toward the Outer Cilicia Basin).

prominent graben structure northeast of the master fault (Fig. 5.11, 5.12). This graben structure has also been previously described by Evans et al. (1978) and Aksu et al. (1992, 2005).

Within the deeper portion of the footwall of the NW-SE trending, NE-dipping master fault, the Messinian evaporites of Unit 2 are mobilized to form a salt pillow (Figs. 5.11, 5.12). This pillow delineates a prominent structure defining the boundary between the Inner and Outer Cilicia Basins, rising in places up to 700 ms above the level of the detachment surface in the deep Inner Cilicia Basin (Figs. 5.1, 5.2, 5.11). This NW-SE trending salt pillow is also mapped by Aksu et al. (2005) and Bridge et al. (2005). Along the northwestern margin of the Inner Cilicia Basin, another large salt wall is mapped (Fig. 5.2). This secondary wall has a NE-SW trend and appears to merge in places with the NW-SE trending primary salt wall (Fig. 5.2). The NE-SW trending wall is best imaged in the 2008 seismic reflection profiles, and occurs in association with the southeastern faults of the basin-bounding Kozan Fault Zone (Figs. 5.3, 5.5, 5.14).

On the basis of growth strata wedges developed on the backlimb and forelimb of salt-cored fold belts, the timing of the salt mobilization can be determined. Seismic reflection profiles clearly show that the lowermost Pliocene section is nearly uniform in thickness, but that the Middle and Late Pliocene sections, particularly after the deposition of the sediments between the M- and the A-reflectors, show the development of prominent depletion synclines and associated sediment growth of Unit 1 successions. This architecture strongly suggests that salt mobilization occurred in the Middle and Late Pliocene and Quaternary and in synchronicity with the deposition of the thick deltaic succession.

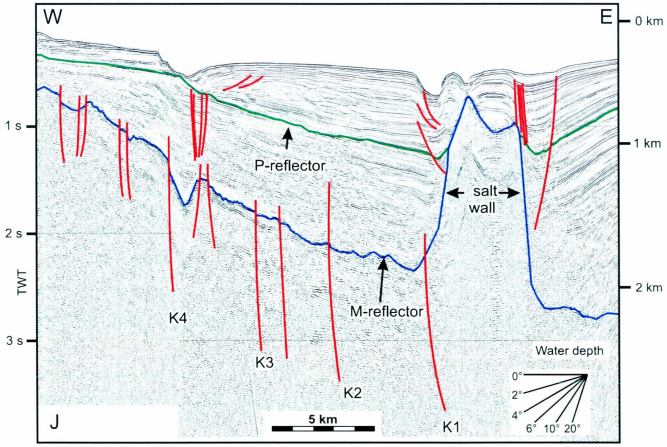

Figure 5.14 Multi-channel seismic reflection profile J showing the structural and stratigraphic architecture of the northwestern margin of the Inner Cilicia Basin with major salt wall, discussed in text. Location is shown in Figure 5.1. Depths at the right assume a constant velocity of 1500 m/s.

Comparison of post-Messinian sediments across the master fault that separates the Inner and Outer Cilicia Basins shows that Unit 1 displays dramatic thinning across the master fault (Fig. 5.13). The > 2200 ms-thick Pliocene-Quaternary successions in the Inner Cilicia Basin are attenuated to < 1200 ms just to the SW of the master fault in the Outer Cilicia Basin (Fig. 5.13). This depositional geometry suggests that the master fault had its most prominent activity in the Middle to Late Pliocene forming a major half graben depocentre in the hanging wall. The upper Quaternary depocentre straddles the Inner and Outer Cilicia Basins (Figs. 5.11, 5.13). The development of this depocentre is controlled by movements on the master fault, by the mobilization of salt in the footwall of the master fault and by the southward shift in the deposition of the younger Quaternary deltaic succession (Aksu et al., 1992).

5.2 Uncertainties in locating structures

It must be noted that there are certain uncertainties in the structural map presented in Figure 5.1. Particular structures (i.e. faults, thrusts, etc.) may deviate from actual boundaries. This uncertainty arises from: limited well data; incomplete seismic coverage for line-to-line correlation; discrepancies and misties in the crossover locations of seismic reflection profiles from different surveys and inherent uncertainties in the ability to trace structures over long distances in the seismic reflection profiles. The accuracy of the map to spatially locate structures decreases as the spacing between seismic reflection profiles increases.

CHAPTER 6: SEDIMENTOLOGY

6.1 Sediments of the Cilicia, Adana, Latakia and Iskenderun Basins

In this section, the sedimentary framework of the northeastern Mediterranean Sea is briefly described to create the basis for a detailed discussion to follow on the specific sedimentary architecture of the Inner Cilicia Basin and its primary sediment source(s) the Göksu River and possibly the Seyhan, Ceyhan and Tarsus Rivers (Fig. 6.1).

6.1.1 Major Rivers in the northeastern Mediterranean

There are four major rivers (Göksu, Tarsus, Seyhan and Ceyhan Rivers) and several ephemeral rivers that drain into the Inner Cilicia Basin (Figs. 6.1, 6.2). The smaller Asi River drains into the Inner Latakia Basin but has a negligible influence on the sediment budget of the Cilicia Basin since its erosional products have been partially separated from the Inner Cilicia Basin by the Misis-Kyrenia structural high during the majority of the Pliocene-Quaternary – see Chapter 5 (Aksu et al., 2005; Figs. 6.1, 6.2).

The Tarsus River is the smallest of the four major contributors to the sedimentary budget of the Cilicia Basin. It drains a basin of 1,426 km^2, with an average annual water discharge rate of 42 $m^3\ s^{-1}$, an average suspended sediment discharge rate of 4.1 kg s^{-1} and a corresponding annual sediment yield of 129 x 10^3 t (Figs. 6.3-6.5; EIE, 1982, 1984). The Seyhan River drains a basin of 19,352 km^2 and has an average annual water discharge rate of 274 $m^3\ s^{-1}$. The average suspended sediment discharge rate of the Seyhan River is 164.4 kg s^{-1}, with an annual sediment yield of 5,185 x 10^3 t (Figs. 6.3-

6.5; EIE, 1982, 1984). The Ceyhan River has the largest drainage basin at 20,466 km^2 and has an average annual water discharge rate of 303 $m^3 s^{-1}$. The average suspended sediment discharge rate of the Ceyhan River is 173.2 kg s^{-1}, corresponding to an annual sediment yield of 5,462 x 10^3 t (Figs. 6.3-6.5; EIE, 1982, 1984). The Göksu River drains a moderately sized basin of 10,065 km^2, with an average annual water discharge rate of 126 $m^3 s^{-1}$. The average suspended sediment discharge rate of the Göksu River is 80.5 kg s^{-1}, with an annual sediment yield of 2,539 x 10^3 t (Figs. 6.3-6.5; EIE, 1982, 1984). These four rivers are the main suppliers of siliciclastic sediments into the Adana, Cilicia and Iskenderun Basins, with a combined sediment yield of 13,315 x 10^3 t being deposited annually (Figs. 6.3-6.5; EIE, 1982, 1984). The middle reaches of Tarsus, Seyhan and Ceyhan Rivers were dammed between 1956 and 1972, so the above sediment discharge rates, measured after damming, should be regarded as minimum. Lastly, the Asi River, while not a main contributor to the sedimentary budget of the Cilicia Basin, drains an area of ~16,170 km^2, with an average annual discharge of 48 $m^3 s^{-1}$ and an annual sediment yield of 514 x 10^3 t (Figs. 6.3-6.5; EIE, 1982, 1984). Three of the major rivers in the region - the Tarsus, Seyhan and Ceyhan Rivers - form a major deltaic complex that occupies the present-day Adana Basin, with their proximal deltaic and distal prodeltaic successions extending into the Inner Cilicia Basin. The Göksu River forms a prominent, although smaller delta, along the western margin of the Inner Cilicia Basin near the transition between the Inner and Outer Cilicia Basin (Fig. 6.2). The deltaic sediments originating from these four major rivers constitute the Pliocene-Quaternary successions of Unit 1, described in Chapter 4.

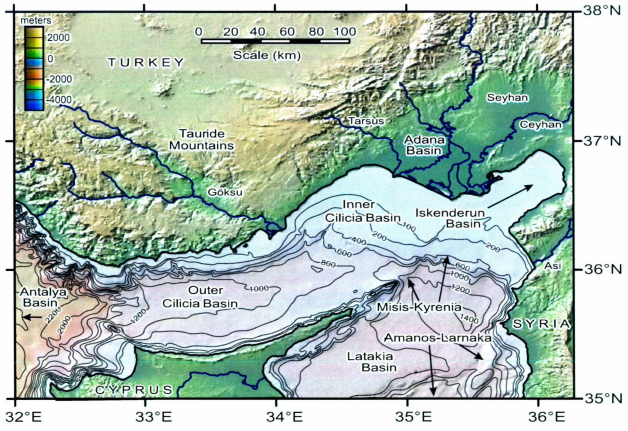

Figure 6.1 Map showing the physiography of the northeastern Mediterranean Sea, including major basins, such as the Adana, Cilicia and Latakia Basins and the corresponding sediment sources from the Seyhan, Ceyhan, Tarsus, Göksu and Asi Rivers. Digital seafloor topography from Smith and Sandwell (1997) and land elevation data from Global Multi-Resolution Topography (Ryan et al., 2009). Image from GeoMapApp (www.geomapapp.org).

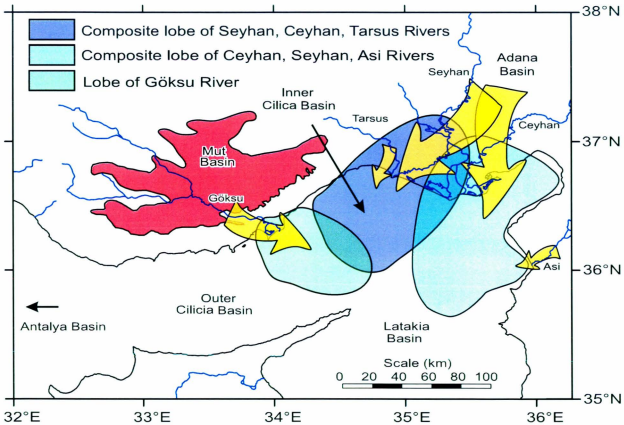

Figure 6.2 Map showing the sediment influx into the Adana, Cilicia and Latakia Basins from the delta lobes of the Seyhan, Ceyhan, Tarsus, Göksu and Asi Rivers. The position of the Mut Basin is highlighted in red.

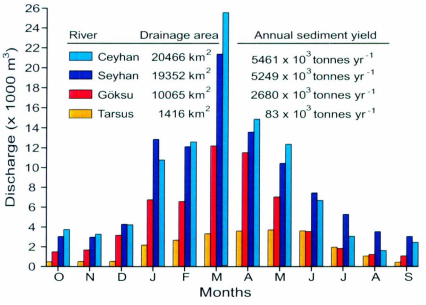

Figure 6.3 Average monthly water discharges (in 1000 m^3) of the Seyhan, Ceyhan, Tarsus and Göksu Rivers taken between 1972 and 1981 (data from EIE, 1984). Also shown are the drainage areas of these rivers and their associated annual sediment yields, also from EIE (1984) - see also Fig. 6.5.

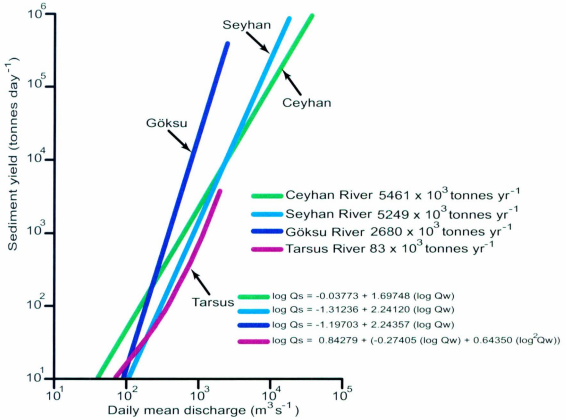

Figure 6.4 Suspended sediment discharge rates for the Seyhan (1966-1979), Ceyhan (1965-1979), Tarsus (1954-1979), and the Göksu (1963-1982) Rivers (data from EIE, 1982). Log QW = daily mean discharge in m^3s^{-1}, Log QS = sediment yield in t day^{-1}.

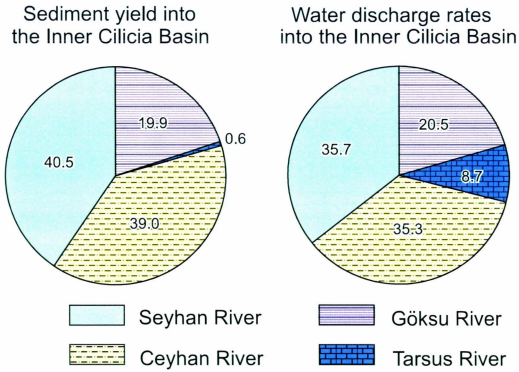

Figure 6.5 Pie charts showing the comparison between the present-day annual sediment yields and average annual water discharge rates entering into the Inner Cilicia Basin through the Seyhan, Ceyhan, Göksu and Tarsus Rivers.

Exploration well and seismic reflection data show that the Pliocene-Quaternary successions in the southern Adana and Inner Cilicia Basins are characterized by prograded wedges of proximal deltaic and distal prodeltaic sediments which reach their maximum thicknesses exceeding 2500 ms (or ~2400 m) in the central portion of the Inner Cilicia Basin (Fig. 6.6; Burton-Ferguson et al., 2005, Aksu et al., 2005). Previous studies (e.g. Aksu et al., 2005; Hall et al., 2005) report that the Pliocene-Quaternary successions of Unit 1 form two well-defined, arcuate lobes in the northeastern segment of the eastern Mediterranean Sea: (a) the northwestern lobe, which is situated within the Outer and Inner Cilicia Basins and extends into the onland Adana Basin in the northeast and (b) the southeastern lobe, which is situated within the Inner and Outer Latakia Basins and extends into the onland Mesaoria Basin in the southwest and the marine Iskenderun Basin in the northeast (Fig. 6.6). The northwest convex and arcuate Misis-Kyrenia fold-thrust belt separates these two major delta lobes from one another. The northwestern lobe is thickest along the central axes of the Inner and Outer Cilicia Basins and sharply thins toward the Kyrenia Range in the south and the southwestern Turkish coast in the north (Fig. 6.6). The northwestern sediment lobe also shows marked thinning toward the northeast into the Adana Basin and toward the southwest into the Outer Cilicia Basin, although a minor lobe is developed within the westernmost portion of the Outer Cilicia Basin (Fig. 6.6; Aksu et al., 2005). The southeastern lobe displays a markedly similar geometry, with its thickest pile lying along the central axis of the Inner and Outer Latakia Basins. This lobe also shows dramatic thinning toward the Misis-Kyrenia fold-thrust belt in the northwest and toward the Amanos-Larnaka fold-thrust belt in the southeast (Fig.

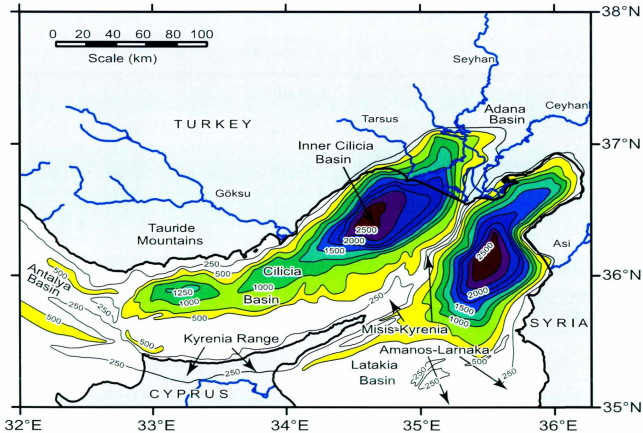

Figure 6.6 Isopach map of Unit 1 showing the distribution of Pliocene-Quaternary sediments in the Cilicia, Adana, Latakia and Iskenderun Basins (thicknesses in milliseconds; re-drawn from Aksu et al., 2005 and Hall et al., 2005). Note the presence of two continuous major lobes, which are separated by the Misis-Kyrenia Fault zone. The northwestern and southeastern lobes extend from the Adana Basin into the Cilicia Basin and Latakia Basin, respectively. The thickest portions of these lobes are situated along the central axis of the Cilicia and Latakia Basins.

6.6; Hall et al., 2005). This study integrates new seismic reflection profiles collected by Memorial University in 2008 with available seismic reflection profiles from previous studies to generate more detailed isopach maps (further discussed in Section 6.2.3)

6.1.2 Paleo-shoreline position in Inner Cilicia Basin

There are several factors that control the position of the shoreline in the northeastern Mediterranean Sea, which include: (i) tectonic movements, (ii) variations in global sea-level and (iii) the mode and rate(s) of sedimentation filling the accommodation space created by the interplay between tectonic movements and global sea-level variations. Because any discussion concerning "source-to-sink" relationships in the Inner Cilicia Basin will inevitably involve the position of the shoreline during certain geological times, the above three factors are briefly elaborated in the following paragraphs. Here, the aim is not to present a thorough review of the topics, but to provide sufficient background so that the "source-to-sink" issues can be placed within a solid framework.

Tectonic movements

Tectonic movements, whether uplift or subsidence, are important in determining the position of the shoreline in a given region. Recent studies in south-central Turkey (e.g. Şafak et al., 2005; Eriş et al., 2005; Bassant et al., 2005; Radeff et al., 2011; Shildgen et al., 2012; Cosentino et al., 2012) document that during the Early-Mid Miocene there existed an ancestral marine basin which occupied large portions of the

northeastern Mediterranean Sea. As the regional tectonics evolved during the Late Miocene to Pliocene-Quaternary, this basin became partitioned to create the isolated depocentres observed today (Fig. 6.7). These studies clearly show that the northern part of the Miocene basin must have become emergent after the Tortonian, because the geological histories of the Mut and Adana Basins are very similar in the Oligocene-Middle Miocene, but show major differentiations after the Tortonian (e.g. Cosentino, 2010; Radeff et al., 2011; Cosentino, 2012). Examination of geological samples from the Mut Basin show the presence of marine fossils in the sedimentary record in strata dated to be from the late Tortonian, with an abrupt cessation of marine deposition after this period when the region became emergent (e.g. Eriş et al., 2005; Bassant et al., 2005; Cosentino et al., 2012). During this Late Miocene uplift, the marine Mut Basin was incorporated into the Tauride orogens and became perched over the evolving Taurus Mountains, where it now rests higher than 2000 m above the present-day sea-level (e.g. Şafak et al., 2005; Eriş et al., 2005; Bassant et al., 2005; Radeff et al., 2011; Schildgen et al., 2011-12; Cosentino et al., 2012).

In the meantime, the Adana Basin continued to subside, remaining marine for the majority of the Pliocene-Quaternary (Turkish Petroleum Corporation, unpublished data; Cosentino et al., 2010; Radeff et al., 2011; Cosentino et al., 2012). Recent studies indicate that the rate of subsidence increased notably during the early Messinian at about 5.6 Ma as well as at about 5.45 Ma (Cosentino, 2010; Radeff et al., 2011) when >1,000 m-thick fluvial sediments of the Handere Formation were deposited within the Adana Basin. The Adana Basin eventually became emergent as it progressively filled to

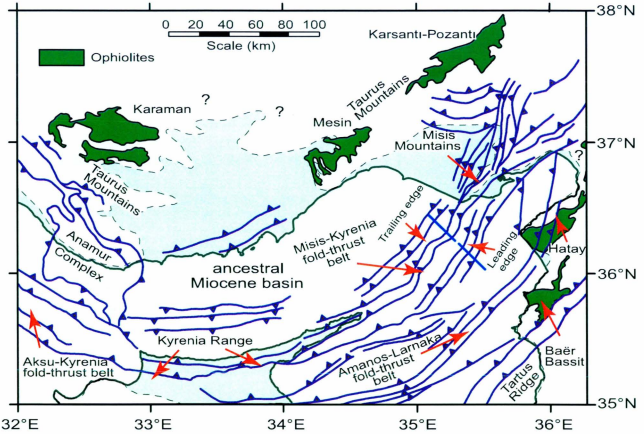

Figure 6.7 Map showing the approximate position of the ancestral basin that occupied the northeastern Mediterranean during the Early-Middle Miocene compiled using published geological maps of Turkey (1:500,000 Adana Sheet, Ternek 1962) and Kouwenhoven and van der Zwaan (2006).. The Miocene structures are from Aksu et al. (2005), and Aksu and Hall unpublished maps. Also shown are the major ophiolite successions.

capacity with the prograded deltaic successions sourced from the Seyhan, Ceyhan and Tarsus Rivers during the latter portion of the Pliocene-Quaternary (Burton-Ferguson et al., 2005).

During the entire period from Messinian to the Recent, the Cilicia Basin continued to subside, creating the deep depocentre that we observe today (e.g. Aksu et al., 2005).

Global sea-level variations

Global sea-level is another critical factor that controls the position of the shoreline. Global sea-level (eustasy) has a well-documented oscillatory nature, with fluctuations directly corresponding to the volume of the world's oceans locked away in growing or decaying continental ice sheets. As sea-level increases, the shoreline retrogrades (i.e. moves landward) to accommodate the increase in water level. As the sea-level falls, the shoreline progrades (i.e. moves seaward). To determine how far the shoreline retrogrades/progrades, the sea-level at various intervals must be estimated. The global $\delta^{18}O$ record is a known proxy for global sea-level. Oxygen isotopic studies in benthic foraminifera show that global $\delta^{18}O$ values were considerably depleted during the Early Pliocene (Fig. 6.8; Karner et al., 2002). Because there is a strong positive relationship between the global ice volume and the global $\delta^{18}O$ record, with intervals of depleted $\delta^{18}O$ values corresponding to periods of reduced global ice volume (e.g. Imbrie et al., 1984), the Early Pliocene low $\delta^{18}O$ values suggest considerably higher global sea-level (e.g. Dwyer and Chandler, 2009). For example, various authors estimated that the

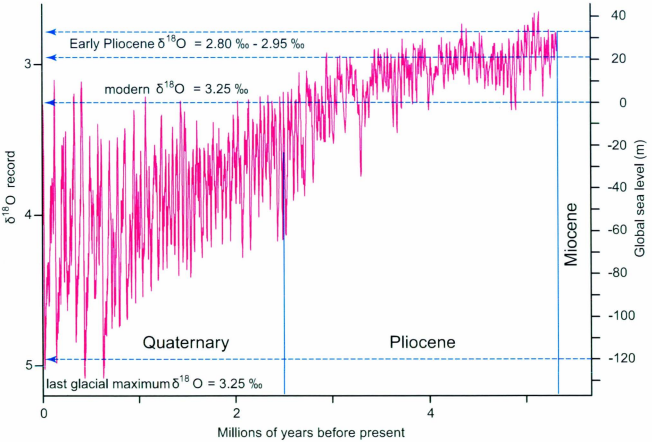

Figure 6.8 Stacked global benthic foraminiferal oxygen isotope ($\delta^{18}O$) record (from Karner et al., 2002), showing the considerably lower $\delta^{18}O$ values during the Early Pliocene, which suggests higher global sealevel.

sea-level during the Pliocene ranged from 10-40 m above the present-day sea-level, with an average value of +25 m being used for the Mid-Pliocene warm interval in various numerical climate model simulations (e.g. Dwyer and Chandler, 2009; Raymo et al., 2011).

Infilling of the accommodation space

The infilling of the accommodation space created by tectonic subsidence and/or sea-level rise (actual or relative) is another important factor which defines the position of the coastline. During the Pliocene-Quaternary, the Seyhan, Ceyhan, Tarsus and Göksu Rivers constructed major deltas that form the core of the sediments deposited within the onland Adana Basin and the offshore Inner Cilicia, Inner Latakia and Iskenderun Basins. Extensive exploration drilling results and a dense grid of industry seismic reflection profiles from the onland Adana Basin show that the region was a shallow marine depocentre during the end of the Messinian (Burton-Ferguson et al., 2005; Cosentino et al., 2010). Industry seismic reflection profiles show the presence of an approximately 1800 m thick Pliocene-Quaternary succession in the Adana Basin, which progressively thins from the present-day shoreline toward the north (Burton-Ferguson et al., 2005; Aksu et al., 2005). Additionally, the seismic data show that the subcrop edge of the Pliocene-Quaternary successions are clearly erosional, suggesting that the edge of the ancestral Pliocene-Quaternary basin may have been located further towards the north. As the available accommodation space filled, the paleoshoreline migrated 40-60 km toward the south to reach its present position. While the volume of sediments lost to erosion

cannot be readily estimated, the erosional products are assumed to be re-deposited further into the Adana and/or Cilicia Basin. For the purpose of sediment budgets, the amount of net sediment loss is assumed to be negligible.

There are no hard data from the northeastern Mediterranean region regarding the past positions of the shoreline during Pliocene-Quaternary. For the back-of-the-envelope bulk volume calculations, an average shoreline position was assigned so as to include the Pliocene-Quaternary sediments that may now be emergent (e.g. the Adana Basin). To this end, a "Pliocene coastline" was assigned at the 200 m topographic contour (in regions other than the Adana Basin), based on several lines of argument:

1. The global oxygen isotopic curve shows that there was considerably less glacial ice stored in the polar regions during the latest Miocene-Early Pliocene than there is today (Fig. 6.8; Karner et al., 2002). Thus, the global sea-level during the Early Pliocene was 10-40 m higher than the present-day sea-level (Dwyer and Chandler, 2009).

2. During the Late Miocene (i.e. Tortonian), the region presently occupied by the Taurus Mountains was part of a shallow sea connected to the ancestral Cilicia, Adana, Latakia and Iskenderun Basins (Figs. 6.7; Şafak et al., 2005; Eriş et al., 2005; Bassant et al., 2005; Cosentino et al., 2012). The topographic gradient along the central Taurus Mountains must have changed sharply from the Early Pliocene to Recent as the Taurus Mountains uplifted and became a prominent structure (e.g. Şafak et al., 2005). For example, the Mut Basin was a marine

depocentre connected to the Adana and Cilicia Basins until the Late Miocene (Eriş et al., 2005; Bassant et al., 2005; Cosentino et al., 2012), but became fragmented and subaerially exposed during the rise of the Taurus Mountains in the Late Miocene (Radeff et al., 2011; Cosentino et al., 2012), with the uplift continuing into the Pliocene-Quaternary (Schildgen et al., 2011; Cosentino et al., 2012).

3. Examination of the geological maps published by the Maden Tetkik ve Arama (Turkish Mineral Exploration and Research) shows that in the vicinity of the Inner Cilicia Basin, the 200 m topographic contour broadly corresponds with the transition from the Pliocene-Quaternary marine successions and the early Cenozoic-Mesozoic successions that constitute the core of the Taurus Mountains (Erentöz and Ternek, 1962; see Fig. 6.9).

4. While the morphology of the ancestral Adana Bay changed dramatically during the Pliocene-Quaternary as it became filled with sediments, there was likely little change in the morphology of the northern margin of the Cilicia Basin. For example, the coastal plain around the Göksu River is notably narrower than that observed in the Adana Basin, suggesting that the Pliocene shoreline was approximately in the same position as is the present-day shoreline, which is quite close to the 200 m contour in the Outer Cilicia Basin (Figs. 6.1, 6.2).

In summary, the Pliocene-Recent evolution of the shoreline in the northeastern corner of the eastern Mediterranean Sea is controlled by a complex interplay between the

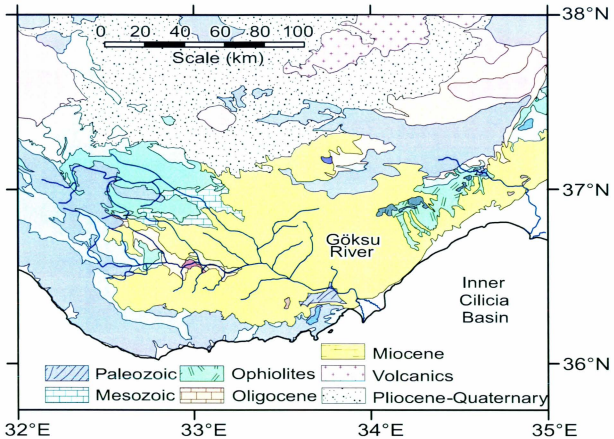

Figure 6.9 Simplified geological map of southern Turkey from Maden Tetkik ve Arama (*Turkish Mineral Exploration and Research*). In the Inner Cilicia Basin, the 200 m topographic contour broadly corresponds with the transition from the Pliocene-Quaternary marine successions and the early Cenozoic-Mesozoic successions that constitute the core of the Taurus Mountains (Erentöz and Ternek, 1962).

variations in the height of the global sea-level, the amount of delta progradation during the Pliocene-Quaternary by the Seyhan, Ceyhan, Tarsus and Göksu Rivers and the relationship between the rates of basin subsidence within the Adana and Inner Cilicia Basins and uplift along the Taurus Mountains. In order to delineate the history of the sedimentary by-products of the Göksu River, a number of constraining assumptions must be made; the first of which is listed below:

- **Assumption-1:** In the sediment volume calculations of the Pliocene-Quaternary successions, the position of the Pliocene shoreline (Fig. 6.10) is assumed to lie at the 200 m topographic contour, except in the Adana Basin, where the paleoshoreline was taken as the 0 m contour in the Pliocene-Quaternary isopach map of Burton-Ferguson et al. (2005) and Aksu et al. (2005), i.e. Fig. 6.6.

6.1.3 Delta morphology

Deltas develop at the mouths of rivers. When a river enters a standing water body (e.g. the sea) it deposits its sediment load, depositing coarser sediments near the river mouth and more fine-grained sediments further seaward. Over time, deltas build characteristic wedge-shaped deposits along shorelines (Gilbert, 1885; Kenyon and Turcotte, 1985). In seismic reflection profiles acquired perpendicular to the shoreline, deltas are imaged as distinctive lenticular packages that show pronounced thinning both toward and away from the shoreline (e.g. Fig. 6.11). The stability of the delta is controlled by the interplay between (i) the rate of sediment supplied by the river, (ii) the rate of global sea-level rise or fall, and (iii) the rate of tectonic subsidence or uplift. The

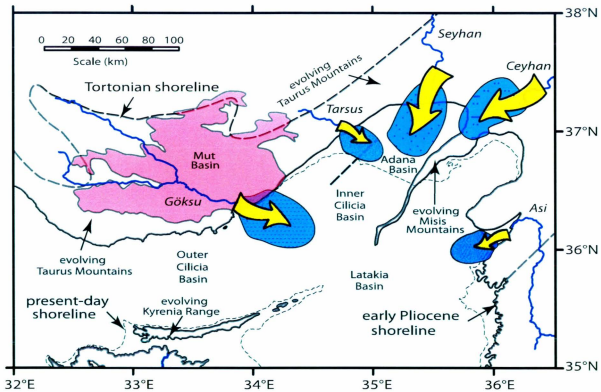

Figure 6.10 Map showing the paleogeography of the northeastern Mediterranean during the early Pliocene. The Upper Miocene (Tortonian) shoreline is re-drawn from Kouwenhoven and van der Zwaan (2006). Also shown are the present-day shoreline (dashed line) and the approximate positions of the ancestral Seyhan, Ceyhan, Tarsus, Göksu and Asi Rivers and their Early Pliocene delta lobes. River positions are taken from their present-day locations, but are truncated at the 200 m topographic contour. The gray shaded areas are the evolving mountains associated with the ongoing tectonics.

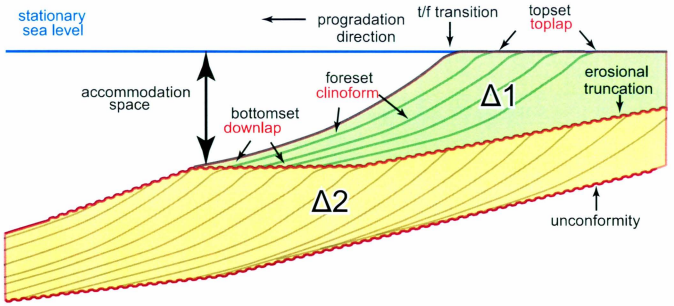

Figure 6.11 Schematic cross-section showing the internal architecture of two vertically stacked deltas (Δ1 and Δ2) separated by a shelf-crossing unconformity. t/f transition = topset-to-foreset transition.

interaction(s) between global sea-level variations and tectonic movements is/are responsible for the creation of accommodation space, i.e. the space below the relative sea-level available for sedimentary infilling by the river. If the rate of sediment supply by the river is greater than the amount of accommodation space the delta quickly fills the accommodation space and progrades. However, if the rate of sediment supply is less than the creation of accommodation space the delta will retrograde. When the rate of sediment supply is equal to the rate of creation of accommodation space, the delta develops a still stand and aggrades (i.e. stacks vertically).

The internal architecture of deltas is very distinctive (Fig. 6.11): at the proximal end near the channel mouth, the sediments are nearly horizontal; these beds are often referred to as the topset beds. Moving into slightly deeper waters, the inclined prodelta sediments are referred to as foreset beds (Fig. 6.11). In the deeper water setting of the inner shelves, the gently seaward-dipping to nearly horizontal successions are referred to as the bottomset beds. Recall from Chapter 2 that the regions of topset and bottomset beds are imaged as seismic packages that are respectively characterized by toplap and downlap reflection terminations, whereas variably seaward dipping clinoform reflections characterize the foreset beds of the delta (Mitchum, 1977; Fig. 6.11). The topset-to-foreset transition of a delta package denotes the position of the former delta front during the time of deposition. If the topset-to-foreset transition point of a delta becomes buried, this is viewed as a clear signal that the deltaic successions that once occurred somewhere near the shelf edge of a basin must have experienced subsidence. The depth of burial of the topset-to-foreset transition reveals the amount of subsidence a delta wedge has

experienced. If the age of a delta is known where the depth of the topset-to-foreset transition can be measured, this information can be used to determine the rate of subsidence of the receiving basin. In modern deltas of the eastern Mediterranean Sea, the topset-to-foreset transition occurs within 5-10 m water depth (e.g. Aksu et al., 1992a,b).

During the rapidly oscillating sea-level setting of the Quaternary and to a lesser extent Late Pliocene, deltas in the northeastern Mediterranean Sea were forced to prograde seaward and retrograde landward many times following the coastline. For example, during the glacial periods, deltas prograded seaward as the glacio-eustatic sea-level fell. Across the Inner Cilicia and Inner Latakia Basins, the present-day shelf break denotes the topset-to-foreset transition at the maximum progradation phase during the last glacial period (i.e. isotopic stage 2; Fig. 6.12; Aksu et al., 1992a,b). As the post-glacial sea-level rose, deltas lost their dynamic equilibrium with the environment and rapidly retreated landward, leading to the deposition of a thin veneer of sediments originating from reworking and ravinement (i.e. erosion during transgression) of former coastal sediments. At the maximum sea-level highstand, deltas were re-established in the ancestral Adana Bay (e.g. Fig. 6.10) and foreset progradation started again. During times of sea-level fall associated with continental glaciations, deltas prograded seaward 40-60 km from their former positions, establishing themselves along the shelf-edge. In these intervals the former nearshore shelf setting became subaerially exposed and experienced further erosion, initiating the erosional surface associated with the shelf-crossing unconformities, which are further eroded during the subsequent transgression.

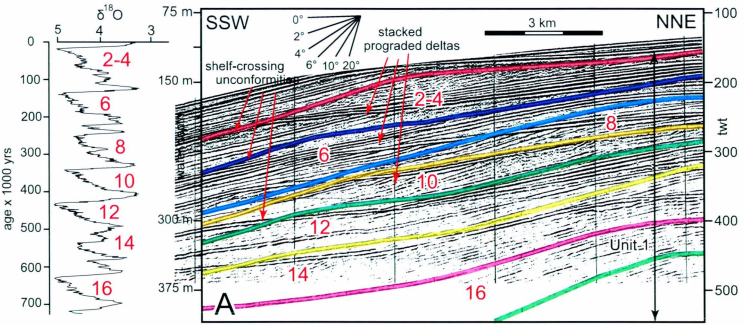

Figure 6.12 Single channel seismic reflection profile A showing the internal architecture of several vertically stacked prograded delta packages in Inner Cilicia Basin (re-drawn from Aksu et al., 1992a). Note that each prograded delta package is separated from the other by major shelf-crossing unconformities. Also shown is the global oxygen isotopic curve ($\delta^{18}O$) from Lisiecki and Raymo (2005) and the correlation of the stacked prograded delta packages and the global oxygen isotopic curve. Red even numbers represent global glacial intervals when the deltas prograded seaward. Location is given in Figure 6.13.

Along continental margins that do not experience tectonic subsidence, the repeated sea-level rises and falls create a series of seaward prograded packages developed from a nearly horizontal surface, where subsequent packages simply by-pass the previously-deposited packages. However, along continental margins that experience sustained subsidence, such deltas form distinctive stacked, prograded successions that are separated from one another by major shelf-crossing unconformities. The shelf and the upper slope regions of the Inner Cilicia and Inner Latakia Basins are underlain by numerous stacked, prograded seismic packages, which are bounded by unconformities, suggesting that the margin has experienced significant tectonic subsidence in the Pliocene-Quaternary (Figs. 6.12-6.14 and 6.20; Aksu et al. 2005; Hall et al., 2005).

6.2 Sediment budget calculations

Until now, the primary study area for this thesis in terms of data processing and structural interpretation has been located in the Inner Cilicia Basin. However, the Göksu River enters the Mediterranean Sea near the transition between the Inner and Outer Cilicia Basins, with its delta lobe extending both into the Inner and Outer Cilicia Basins (Fig. 6.2). In order to account for all the sediments carried by the Göksu River since the latest Messinian and to provide realistic rates of sediment supply from the rising Taurus Mountains, including denudation rates, the sediment volume calculations must be extended to include the entire Cilicia Basin. Therefore, the calculations in the following text were conducted using all of the available seismic reflection profiles collected from the Inner and Outer Cilicia Basins, shown in Figure 6.13. Here, the author acknowledges

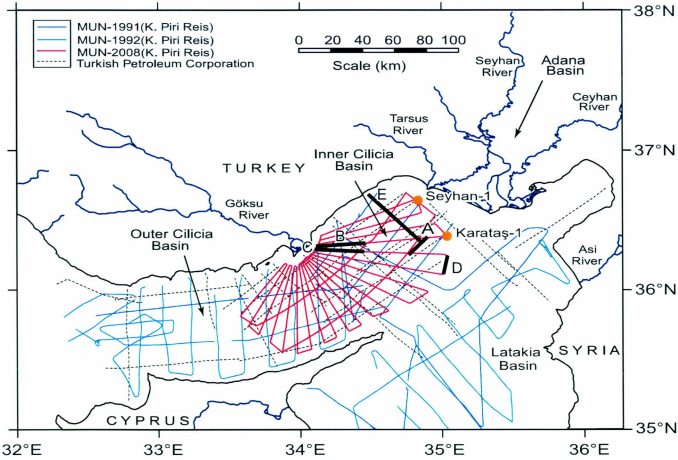

Figure 6.13 Map showing the locations of seismic reflection profiles illustrated in Chapter 6. Also shown are the locations of the exploration wells Seyhan-1 and Kartataş-1. Profiles A, B, C, D and E (discussed in text) are highlighted in black.

the data contributions and structural interpretations from two M.Sc. theses from Memorial University of Newfoundland: Piercey (2011) and Kurtboğan (in progress). The author has re-interpreted all the seismic reflection profiles from these two theses and carried across the M-, A- and P-reflectors, discussed below (see also Chapter 4).

Within the Cilicia Basin, there are small regions that are not covered by the existing seismic reflection profile data. Furthermore, previous studies showed that there are leakages of sediment across the Misis-Kyrenia horst block in the east (e.g. Aksu et al., 2005) as well as longitudinally into the Antalya Basin in the west (Işler et al., 2005; Fig. 6.1). The true amount of leakage is difficult to calculate; however, an estimate can be made. Kukal (1971) suggests that between 25 and 35% of the sediments carried by a river system is carried away into the deeper basinal areas by suspended sediment transport. Because the available seismic profiles extend beyond the delta lobe of the Göksu River (Figs. 6.2, 6.13), most of the fine-grained sediments must be already accounted for in the sediments imaged in the central portion of the Outer Cilicia Basin.

- **Assumption-2:** It is assumed that the sediment volume calculations based solely on the existing seismic reflection profile coverage underestimate the total volume of sediments by approximately 15%.

6.2.1 Chronostratigraphy of important markers

In order to carry out sedimentary budget calculations, the seismic reflection profile data must be divided into regionally correlatable packages. The seismic reflection

data include two prominent reflections within the Pliocene-Quaternary successions of Unit 1, which are readily traceable across the entire study area (Fig. 6.14). These marker horizons are referred to as the "A-reflector" and the "P-reflector" (see Chapter 4). A third marker, the "M-reflector", defines the base of Unit 1 (Fig. 6.14). The ages of the M- and A-reflectors have been firmly established using biostratigraphic data from two exploration wells in the Inner Cilicia Basin (Turkish Petroleum Corporation, unpublished data; Fig. 6.13). The age of the P-reflector is more speculative and should be used with caution (see Chapter 4 for more detail).

- **Assumption-3:** It is assumed that the P-, A- and M-reflectors represent marker horizons with ages of 1.9 Ma, 3.6 Ma and 5.3 Ma, respectively (see Chapter 4).

6.2.2 Time to Depth conversion

The seismic velocity of the sediments that comprise Unit 1 increases with depth from ~1500 m s^{-1} at the sediment-water interface to ~ 2200-2400+ m s^{-1} at the base of Unit 1, immediately above the M-reflector. This range in velocities is large enough that any realistic volume calculation in the Inner Cilicia Basin must be conducted using a series of velocity functions that permit accurate depth-conversion. The two-way-time – interval velocity functions used to convert the sections from time to depth domain are derived from the velocity analysis stage of the seismic reflection data processing (see various examples in Chapter 3). Velocity analysis locations were chosen at regions in the seismic reflection profiles where the reflections lie nearly horizontal and the semblance bulls-eyes are well-defined (also see Chapter 3). The velocity relationships were found to

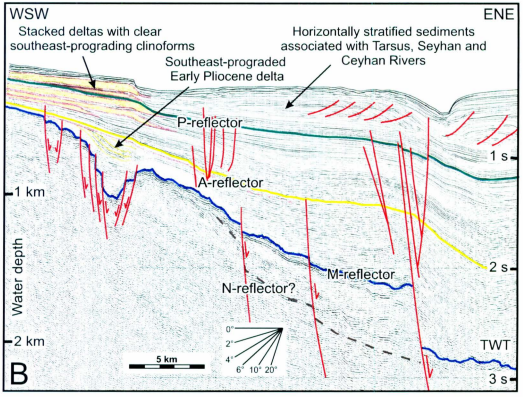

Figure 6.14 Seismic reflection profile B showing prominent southeast prograded clinoform packages in the northwestern margin of the basin, immediately seaward of the present day Göksu River (Fig. 6.13), that are clearly sourced by the Göksu River. Depths on the left assume a simple constant interval velocity of 1500 m/s.

vary slightly across the basin, so several locations were chosen to ensure the highest degree of accuracy. Seismic velocity rapidly changes from the lowermost Early Pliocene sediments of Unit 1 (V_{plio} = ~2400 m/s) to the Messinian evaporites of Unit 2, i.e. just beneath the M-reflector (V_{mio} = ~3500-4500 m/s). To avoid depth converting the seismic reflection profiles with anomalously high velocities, the interval velocity of the Early Pliocene interval (i.e. between A- and M-reflectors) is chosen as the average interval velocity between the A-reflector and the lowermost Pliocene sediments directly above the M-reflector. Depth conversions beneath the lowermost Pliocene sediments are conducted using a constant seismic velocity of ~2400 m/s due to difficulties estimating the interval velocities at these depths (see Chapter 3). A table was generated that includes the X- and Y-coordinates at each location as well as a series of two-way-time – interval velocity pairs (Table 6.1). This table was imported into the time-depth conversion application TDExpress of Halliburton's Landmark© suite, where the velocity information was used to generate a 3D velocity field, whereby the specified time-velocity function was interpolated between each location using the three picked marker horizons (discussed below) and the seabed to guide the function along the geological features of the subsurface. Figure 6.15 illustrates a depth-converted seismic reflection profile.

6.2.3 Isopach maps

Four isopach maps were drawn to illustrate the variation in sediment thickness of various stratigraphic intervals from the depth-converted seismic reflection profiles using the seismic interpretation software Petrosys: (i) a total isopach map of the Pliocene-

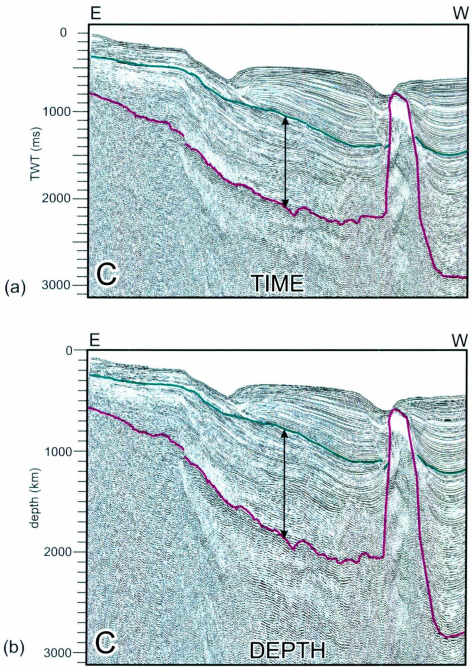

Figure 6.15 (a) Multi-channel seismic reflection profile C viewed in two-way-time and (b) depth converted multi-channel seismic reflection profile B showing the notable increase in sedimentary thicknesses in the lower portion of the profile. Technique described in text. Location is shown in Figure 6.13.

Quaternary successions of Unit 1, (ii) an isopach map of the sediments contained between the M- and A-reflectors, i.e. Unit 1c, (iii) an isopach map of the sediments contained between the A- and P-reflectors, i.e. Unit 1b, (iv) an isopach map of the sediments contained between the P-reflector and the seabed, i.e. Unit 1a. See Chapter 4 for descriptions of various stratigraphic units and subunits.

The total Pliocene-Quaternary isopach map of the Adana-Cilicia Basin complex shows the presence of a very prominent lobe resting in the southern Adana, Inner Cilicia and northern Outer Cilicia Basins (Fig. 6.16). The locus of this lobe sits north of the major north-dipping northwest-southeast trending basin bounding fault, which separates the Inner and Outer Cilicia Basins (Fig. 6.16; also see Chapter 5). The lobe is somewhat elongated in the northeast-southwest direction and shows central thicknesses exceeding 2400 m. It thins toward the northeast into the Adana Basin as well as toward the southwest into the Outer Cilicia Basin (Fig. 6.16). The total Pliocene-Quaternary also rapidly thins both toward the northwest onto the Turkish continental margin and toward the southeast onto the Misis-Kyrenia fold-thrust belt (Fig. 6.16). The sediment thickness lobe of Unit 1 also displays rapid thinning as the sediments abut on the salt structures (described in Chapter 5). A secondary, smaller lobe is developed in the Outer Cilicia Basin. This isopach map, compiled using depth-converted sections, gives realistic thicknesses, and reveals greater details than the isopach map published by Aksu et al. (2005). However, the broad basin-scale morphological elements of these two maps are similar.

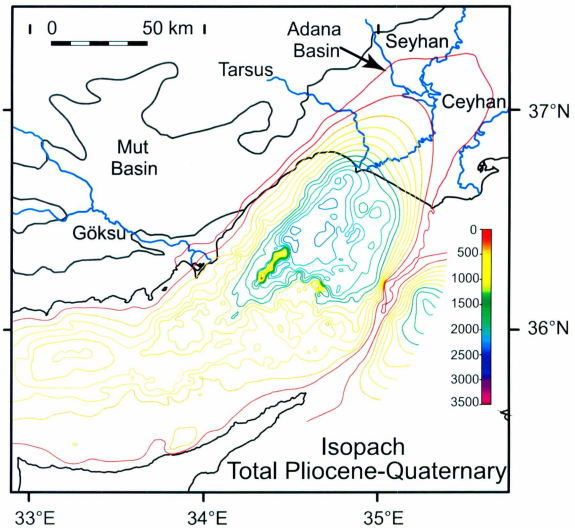

Figure 6.16 Isopach map of the total Pliocene-Quaternary successions (i.e. Unit 1). Contours are drawn every 200 m and have been calculated using depth-converted multi-channel seismic reflection profiles.

Detailed mapping and correlations of the M-, A- and P-reflectors across the entire Cilicia and Adana Basins allowed the examination of the internal architecture of the total Pliocene-Quaternary thickness map shown in Figure 6.16 in three time intervals: (i) an Early Pliocene interval between M- and A-reflectors, Unit 1c (Fig. 6.17), (ii) a Late Pliocene-Quaternary interval between A- and P-reflectors, Unit 1b (Fig. 6.18) and (iii) a Quaternary interval between P-reflector and the seafloor, Unit 1a (Fig. 6.19). These three isopach maps were subject to smoothing; therefore small-scale variations in thickness may not be apparent. Nonetheless, variations in thickness on a larger scale show that each of these three subunits displays rapid thinning toward the Turkish continental margin in the north and northwest and the Misis-Kyrenia fold-thrust belt in the south and southeast.

The isopach map of the Early Pliocene subunit (i.e. Unit 1c, M- and A-reflectors) displays an area of maximum thickness that is defined by a narrow, northeast-southwest and east-west elongated L-shape deposition with central thicknesses ranging from 1400-1600 m along the northwestern segment of the Inner Cilicia Basin (Fig. 6.17). Examination of seismic reflection profiles along the east-west trending portion of the L-shaped lobe shows that these profiles display east- and southeast-directed clinoform progradation at the shelf end. This geometry suggests that the east-west trending portion of the L-shaped lobe must have been sourced from the west by the Göksu River and is likely associated with the distal toe of this delta system. Using this logic, the north-south trending portion of the L-shaped lobe is likely sourced from the northern Seyhan and Tarsus Rivers and is related to the distal end of the deltas associated with these rivers.

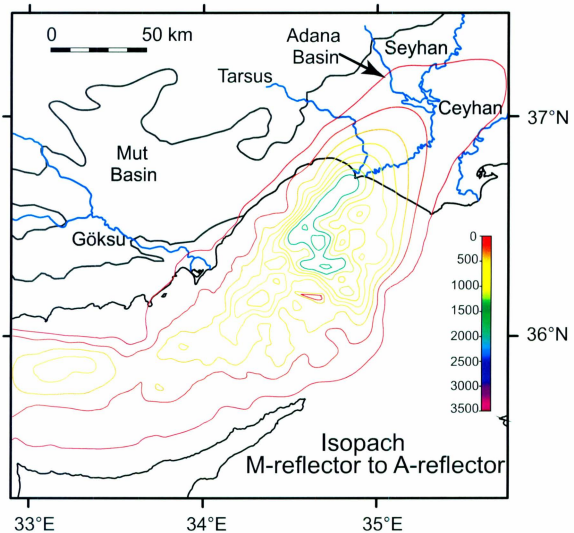

Figure 6.17 Isopach map of the lower Pliocene-Quaternary successions (i.e., M- to A-reflectors). Contours are drawn every 200 m and are calculated using depth-converted mutli-channel seismic reflection profiles.

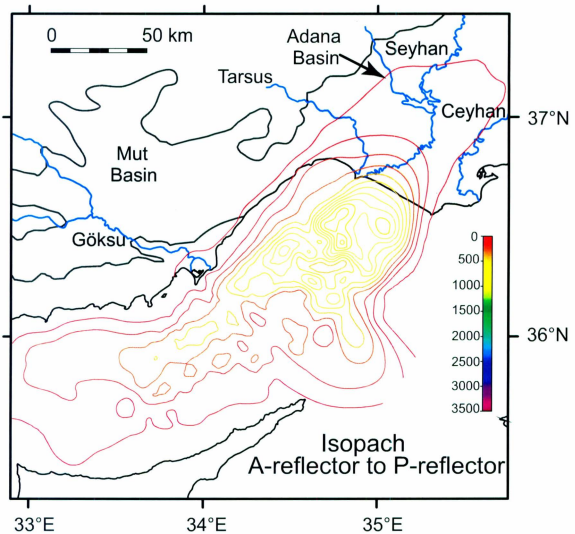

Figure 6.18 Isopach map of the Late Pliocene-Quaternary successions (i.e., A- to P-reflectors). Contours are drawn every 100 m and are calculated using depth-converted multi-channel seismic reflection profiles.

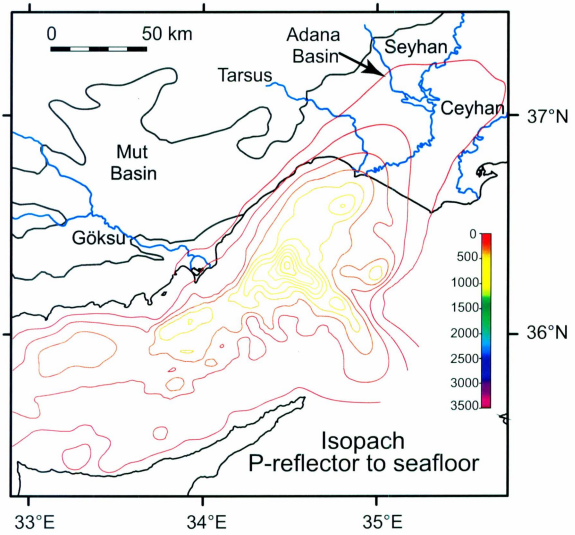

Figure 6.19 Isopach map of the Quaternary successions (i.e., P-reflector to the seabed). Contours are drawn every 100 m and are calculated using depth-converted multi-channel seismic reflection profiles.

While the existing seismic reflection profiles for this study do not image north-south prograded clinoforms in the region of the L-shaped lobe, the prograded packages associated with the Seyhan and Tarsus Rivers do exist in the former marine Adana Basin during this interval (Burton-Ferguson et al., 2005). The lower subunit is notably thin in the Outer Cilicia Basin, where a prominent east-west trending secondary lobe displays central thicknesses of ~600 m (Fig. 6.17). Another, somewhat thicker lobe, with central thicknesses of 900-1000 m, occurs near the transition from the Inner to Outer Cilicia Basin. Here, a narrow and broadly northwest-southeast trending zone of <200-400 m thick subunit separates this lobe from the prominent northeast-southwest trending segment of the L-shaped lobe seen in Inner Cilicia Basin (Fig. 6.17). Examination of seismic profiles across this region shows that this narrow zone corresponds with the northwest-southeast trending salt wall which separates the Inner and Outer Cilicia Basins (see Chapter 5).

The Late Pliocene-Quaternary subunit (i.e. Unit 1b, A- and P-reflectors) shows several prominent lobes, all located in the Inner Cilicia Basin (Fig. 6.18). Three of these lobes have central thicknesses between 900-1100 m and are situated in the innermost portion of the Inner Cilicia Basin. The 800 m thickness contour encircles these three lobes (Fig. 6.18). The proximity of these lobes to the Adana Basin and the present-day shoreline as well as clear southwest-directed prograded clinoforms in this region (i.e. Fig. 6.20; Burton-Ferguson et al., 2005) collectively suggest that they must have been sourced from the north by the Seyhan, Ceyhan and Tarsus Rivers. Another prominent lobe is situated to the west and south of the above-mentioned lobes and shows a central thickness

of ~800 m (Fig. 6.18). This lobe is clearly separated from the innermost lobes (Fig. 6.18), and its geographic position and the east- and southeast-directed prograded clinoforms seen in seismic reflection profiles (also see Chapter 5) collectively suggest that the lobe is sourced by the Göksu River from the west. In the Outer Cilicia Basin, the Late Pliocene-Quaternary subunit is thinner, but shows two to three broadly northeast-southwest oriented lobes situated along the present-day slope adjacent to the present-day Turkish continental margin (Fig. 6.18). Examination of the seismic reflection profiles across these lobes shows that they are developed as the result of overlapping stacked prograded delta successions, all of which show east- and southeast-directed clinoform progradation. Toward the westernmost Outer Cilicia Basin the Late Pliocene-Quaternary subunit is very thin (Fig. 6.18).

The Quaternary subunit (i.e. Unit 1a, P-reflector to the seafloor) shows a large broadly arcuate lobe delineated by the 400 m thickness contour (Fig. 6.19). The 800 m contour defines the locus of this lobe as an elliptical and mainly northwest-southeast trending feature, situated near the transition between Inner and Outer Cilicia Basins (Fig. 6.19). The central thickness in this lobe exceeds 1000 m. Correlations with seismic reflection profiles show that the locus of the Quaternary subunit is associated with the northwest-southeast trending and northeast-dipping listric normal fault that delineates the transition between Inner and Outer Cilicia Basins. Roll-over and thickening on the north side of the listric fault and salt withdrawal and growth associated with the depletion syncline on the south side of the listric fault are responsible for the thick northwest-southeast trending locus of the lobe (Fig. 6.20). Further examination of the seismic

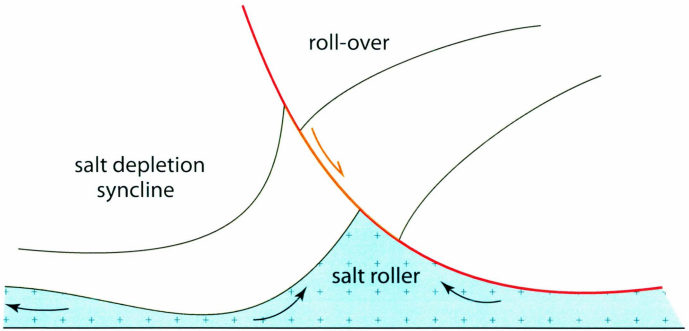

Figure 6.20 Schematic line drawing showing the sediment growth associated with the roll-over on the hanging wall of a listric normal fault, as well as sediment growth associated with salt depletion beneath the footwall of the same listric normal fault. See text for detail.

reflection profiles show that there are southwest-directed progradational clinoform units extending from the northeast toward the northwest-southeast trending segment of the present-day 100 m isobaths; these clinoform packages are clearly sourced from the northeast by the Seyhan, Ceyhan and Tarsus Rivers (Fig. 6.21). However, seismic reflection profiles also show prominent southeast-directed prograded clinoform packages in the northwestern margin of the basin, immediately seaward of the present-day Göksu River (Fig. 6.14). The geographic position and direction of progradation of these clinoform packages clearly show they must have been sourced by the Göksu River.

6.2.4 Volume estimates

The total volume of sediments contained within each isopach map was calculated using the seismic interpretation software Petrosys. Because the available well data lacked detailed descriptions of exact sediment type, densities, porosities etc., a number of assumptions and estimates had to be made to arrive at a dry, solid weight for each interval.

The calculated volume estimates are converted into solid sediment weights using the following method:

1. The porosity of the sedimentary packages was estimated using a seismic velocity-porosity relationship for water-saturated, siliciclastic and normally consolidated shales with siltstone and minor sandstone interbeds (Erickson, 1998). This porosity function was used to determine and subtract the volume

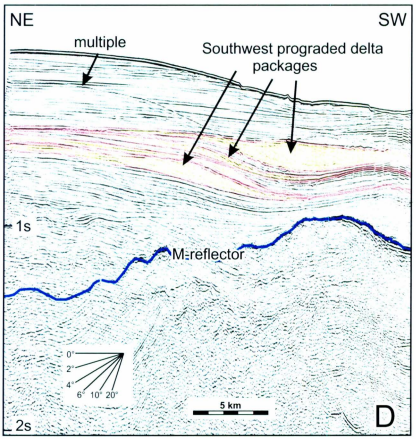

Figure 6.21 Seismic reflection profile D showing the clearly southwest-directed progradational clinoforms units extending from the northeast. These clinoforms packages must sourced from the northeast by the Seyhan, Ceyhan and Tarsus Rivers.

contained by pores from the total sediment volumes to arrive at a volume of solid material (see Table 6.2).

2. The average mineral density of the sediments in the Cilicia Basin is estimated using the assumption that the succession is composed of 75% shale + 25% sandstone in the shelf regions and 90% shale + 10% sandstone in the deeper basinal regions. Sclater and Christie (1980) report that the idealized mineral densities for 100% shale and 100% sandstone are 2720 kg m^{-3} and 2650 kg m^{-3}, respectively. Using the above assumption that the shelf region of the mouth of the Göksu River and the deeper water regions of the Cilicia Basin contains siliciclastic successions with 75% shale + 25% sandstone and 90% shale + 10% sandstone ratios respectively, average mineral densities of 2702.5 kg m^{-3} and 2713.0 kg m^{-3} are calculated based on the above idealized average mineral densities (Sclater and Christie, 1980). Because the shallow shelf regions constitute only ~10% of the total sediments contained in the Cilicia Basin, a basin-wide average mineral density of 2712 kg m^{-3} (0.9*2713 + 0.1*2702.5= 2711.95) is applied to convert the solid sediment volumes to solid sediment weights in tonnes. Table 6.2 shows the total weight of sediment contained within each package.

After arriving at a solid sediment weight using the above method, the next step is to relate the weight of sediment contained in the isopach maps to the discharge rates of the Göksu River. Here, the critical task is to determine the volume and weight of

sediment that is actually supplied into the Cilicia Basin from the west by the Göksu River versus the volume and weight of sediment supplied by the Seyhan, Ceyhan and Tarsus Rivers from the north. While little hard data exist on the proportions of river contributions into the Cilicia Basin it is possible to make some simplifying assumptions to calculate the volumes supplied by each of the other rivers, based on previous arguments.

In section 6.1.2, it is argued that during the Pliocene and most of the Early Quaternary, the ancestral Adana Bay was the repository for the deltaic successions supplied by the Seyhan, Ceyhan and Tarsus Rivers. This sedimentation progressively filled the former bay into what is known as the onland Adana Basin today. The shoreline reached its present position in the upper portion of the Quaternary (e.g. Aksu et al., 1992a,b). Thus, during most of the Pliocene-Quaternary only a small contribution of sediment is expected to arrive into the Cilicia Basin from the Seyhan, Ceyhan and Tarsus Rivers. The fact that the Early Pliocene deltas of the Seyhan, Ceyhan and Tarsus Rivers developed within the ancestral Adana Bay, and that the Early Pliocene delta of the Göksu River developed in the Inner Cilicia Basin, suggests that the majority of the sediments contained between the M- and the A-reflectors in the Inner Cilicia Basin and the eastern and northeastern portion of the Outer Cilicia Basin are supplied by the Göksu River. This notion is further supported by the seismic stratigraphic architecture of the large Early Pliocene delta succession, which shows prominent clinoform patterns prograding eastward into the Inner Cilicia Basin (Fig. 6.14).

- **Assumption-4:** 70% of the sediments contained between the M- and the A-reflectors in the Cilicia Basin are supplied by the Göksu River, with 30% being supplied from the Seyhan, Ceyhan and Tarsus Rivers. This statement assumes that only the suspended load of the Seyhan, Ceyhan and Tarsus Rivers by-passed the Adana Basin and was deposited in the Cilicia Basin, as also elaborated in Section 6.2.

As the ancestral Adana Bay filled with the deltaic sediments supplied by the Seyhan, Ceyhan and Tarsus Rivers, the shoreline progressively moved southward. Therefore, the contribution of sediments by the Seyhan, Ceyhan and Tarsus Rivers into the Inner and Outer Cilicia Basins must have increased during the Mid-Late Pliocene interval. Again, there is no concrete data that would quantify the proportions of sediments supplied from the north versus west. Nonetheless, detailed seismic stratigraphic evaluation of the successions contained between the A- and the P-reflectors clearly illustrates the presence of numerous stacked, east-prograded prominent delta successions along the western margin of the Inner Cilicia Basin. However, the seismic data also show an increasing amount of nearly horizontal reflections that intercalate with the east-prograded delta successions, often showing onlap reflection terminations over the delta sediments (Fig. 6.14). In the western and northwestern Cilicia Basin there is a NE-SW trending salt wall that sits along the eastern margin of the Kozan Fault zone (see Chapter 5). During the Late Pliocene–Quaternary the salt wall became mobilized following the progressive loading of the Early Pliocene successions on the Messinian evaporites of Unit 2. Thus, this salt wall must have created a partition in the basin,

broadly separating the sedimentary influx from the Göksu River in the west and the Seyhan, Ceyhan and Tarsus Rivers in the east. This architecture suggests that, although the considerable amounts of sediment are supplied from the west in the time interval between A- and P-reflectors, an increasing proportion is also supplied from the north.

- **Assumption-5:** 50% of the sediments contained between the A- and the P-reflectors in the Inner and Outer Cilicia Basins are supplied by the Göksu River, with 50% being supplied from the Seyhan, Ceyhan and Tarsus Rivers.

There is a dramatic change in the seismic stratigraphic architecture of the successions contained between the P-reflector and the seafloor. In this region, the seismic profiles show a thick wedge of sediments near the transition between the Inner and Outer Cilicia Basins (e.g. Fig. 6.19). Here, the large proportion of the sedimentary pile thins toward the west and onlaps and/or downlaps onto the P-reflector. This architecture suggests that progressively increasing portions of the sediments may be supplied from the north. However, considerable input is also suggested from the west. The respective sediment contributions from the three rivers from the north and the Göksu River from the west can be estimated based on the proportion of the present-day total sediment yield supplied by the Seyhan, Ceyhan and Tarsus Rivers versus the Göksu River into the Cilicia Basin. For example, the present day sediment yields of the Tarsus, Seyhan and Ceyhan Rivers are 129 x 10^3 t, 5,185 x 10^3 t and 5,462 x 10^3 t, respectively, with a total yield of 10,776 x 10^3 t (see Section 6.1.1). Only about half of the sediments from the combined sediment yields of the Tarsus, Seyhan and Ceyhan Rivers are

expected to arrive in the Cilicia Basin, with the remaining 50% assumed to be deposited in the Latakia Basin (see below). Taking 50% of the total sediment yield from the Tarsus, Seyhan and Ceyhan Rivers, it is expected that 5,388 x 10^3 t of sediments are deposited into the Cilicia Basin from these three rivers annually. The annual sediment yield of the Göksu River is 2,539 x 10^3 t, which is ~32% of the above total sedimentary input into the Cilicia Basin.

- **Assumption-6:** 30% of the sediments in the Cilicia Basin that are contained between the P-reflector and the seafloor are supplied by the Göksu River, with 70% being supplied from the Seyhan, Ceyhan and Tarsus Rivers.

Lastly, there are two lines of arguments which suggest that only 50% of the total sediment yield of the Tarsus, Seyhan and Ceyhan Rivers enters the Cilicia Basin, as explained below:

1. The present-day Seyhan and Tarsus Rivers drain the western portion of the central Taurus Mountains, entering the Adana Basin from the north. Whereas, the Ceyhan River drains the eastern segment of the central Taurus Mountains and enters the Adana Basin from the northeast. The total present-day sediment yields of the Seyhan + Tarsus Rivers are approximately equal to the present-day sediment yield of the Ceyhan River (also see section 6.1).

2. Regional mapping shows that the ancestral Miocene basin in the northeastern Mediterranean was much larger, and included the Cilicia, Iskenderun, Adana,

Latakia, Mesaoria Basins (Fig. 6.7; Aksu et al., 2005; Hall et al., 2005), but also included the former basins now occupied by mountains, such as the Mut Basin and the foredeep that resided over the present-day Misis Mountains and the Kyrenia Range (e.g. Calon et al., 2005a,b). The Pliocene-Quaternary changes in the prevailing tectonics resulted in the fragmentation of this large Miocene basin, leading to the individual quasi-isolated basins observed today. The development of the thrusts that cored the Misis Mountains and the Kyrenia Range and their marine extension, the Misis-Kyrenia belt, created the largest partition separating the Mesaoria, Latakia and Iskenderun Basins in the east from the Adana, Cilicia and the Mut Basin in the west. Isopach maps of the northeastern corner of the eastern Mediterranean show that there are two prominent Pliocene-Quaternary lobes that contain nearly identical volumes (Fig. 6.6).

- **Assumption-7:** 50% of the Pliocene-Quaternary sediments carried by the Seyhan and Ceyhan Rivers are deposited in the Iskenderun and Inner and Outer Latakia Basins with the remaining 50% being deposited within the Adana and Inner and Outer Cilicia Basins. The Göksu River in the west and the Asi River in the east are approximately similar in size and are assumed to provide roughly equal volumes of sediment into their respective drainage basins in the west (i.e. Cilicia Basin) and in the east (i.e. Latakia Basin). Because of its geographic position, the Tarsus River is assumed to drain entirely into the Cilicia Basin.

Tables 6.2-6.4 present the volumes estimated using the methods described in this chapter. In Table 6.2, total sediment volumes contained in the isopach maps presented in Figures 6.17-6.19 are presented. These volumes are then converted into solid weights by first subtracting the porosity estimates (derived from Erickson, 1998) and then multiplying the volumes by an average mineral density of 2712 kg m^{-3} (see above calculations; Sclater and Christie, 1980). In Table 6.3, solid sediment weights are revised to separate the total volumes into contributions from the Göksu River versus contributions from the combined Seyhan, Ceyhan and Tarsus Rivers using Assumptions 4 through 6. In Table 6.4, present-day annual sediment yields of the Göksu, Seyhan, Ceyhan and Tarsus Rivers are used together with Assumptions 2 and 7 to estimate the net annual sediment yields arriving into the Cilicia Basin from the Göksu River and the combined Seyhan, Ceyhan and Tarsus Rivers. These results are further discussed in Chapter 7.

Finally, Table 6.5 compares the present-day annual sediment yields of the Göksu River and the combined Seyhan, Ceyhan and Tarsus Rivers to the average annual sediment yields that are calculated for each isopach interval (i.e. M- and A-reflectors, A- and P-reflectors and P-reflector and seabed) by dividing the weight of sediments contained within each isopach map by the amount of time represented in each map. In the above calculation, the solid weights used are those that are attributed solely to the Göksu River and the combined Seyhan, Ceyhan and Tarsus Rivers (Table 6.5). These results are further discussed in Chapter 7.

6.3 Subsidence rate calculations

In Chapter 5 it is documented that there are several deltas in the Inner Cilicia Basin that show clear clinoform progradations. These prograded delta packages are presently located deep in seismic reflection profiles (Figs. 6.14, 6.22) The present-day depth of these deltas is, in general, a function of actual global sea-level variations through time, basin subsidence since the deposition of the deltas and accommodation space created by the dewatering and compaction of the sedimentary successions through time. So, if the variations in the global sea-level and the amount of compaction can be determined, the amount of basin subsidence can be calculated. In order to determine the rate of subsidence experienced at discrete points in the Cilicia Basin a few simplifying assumptions must be made.

- **Assumption-8:** It is argued in section 6.1.3 that there is a genetic linkage between the topset-to-foreset transition points in deltas and the sea-level in which delta progradation occurs. In the eastern Mediterranean Sea deltas, the average topset-to-foreset transition occurs at approximately 5-10 m water depth (also see Aksu et al., 1992a,b). In the following calculations, the sea-level offset due to topset-to foreset transition is conservatively assumed to be 10 m.

- **Assumption-9:** It is shown in section 6.1.2 that the global oxygen isotopic curve can be used to provide estimates of the global ice volume, thus paleosea-level (Fig. 6.9; Karner et al., 2002). In the subsidence calculations using OSXBackstrip (see below for further description), it is assumed that the sea-level was +25 m

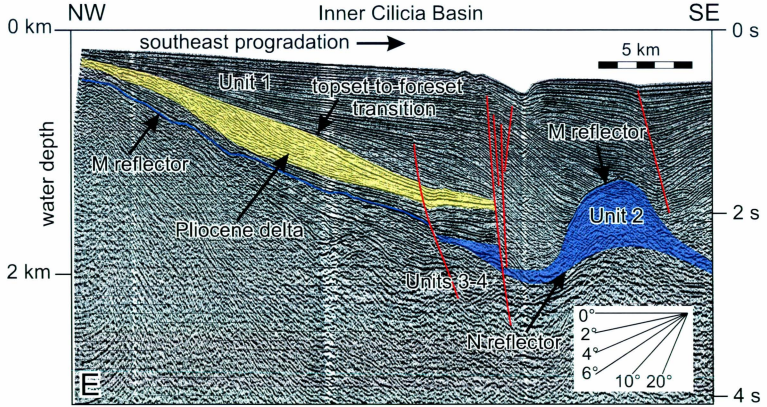

Figure 6.22 Seismic reflection profile E showing the clearly southeast-directed progradational clinoforms units extending from the west and. These clinoforms packages must sourced from the west by the Göksu River. Also note the deeply buried topset-to-foreset transition, indicating signifIcant subsidence since its deposition. The depth scale at the right simply assumes a constant velocity of 1500 m/s in all successions. Location is given in Fig. 6.13.

between the Early-Mid Pliocene (~5.3-3.6 Ma, i.e. the Zanclean Stage) and 0 m in the Early-Mid Quaternary at ~1.9 Ma. Because the Quaternary deltas developed during the rapid sea-level fluctuations associated with the glacial-interglacial cycles of the Quaternary could not be accurately dated using the global oxygen isotope curve, no attempt is made to provide an estimate for the depth of the topset-to-foreset transition in the Quaternary deltas, further increasing the uncertainty in the subsidence calculations for this interval.

- **Assumption-10:** As previously discussed, the global oxygen isotopic record suggests that the major marine transgression following the end-Messinian event must have raised the sea-level to ~+25 m. During this time, the Central Taurus Mountains as well as the Kyrenia and Misis Mountains were becoming emergent. So, the Cilicia Basin must have had an inherited bathymetry since the Pliocene. However, there exists no data to quantify the depth and shape of this paleobathymetry. In the absence of such knowledge, a conservative broad assumption is taken that the Cilicia Basin had a seafloor morphology similar to the morphology seen today.

Subsidence of a sedimentary basin can be attributed to three primary processes: (i) tectonic subsidence (ii) water and sediment loading and (iii) compaction of sediments (Allen and Allen, 1990; Watts, 2001). Tectonic subsidence refers to the subsidence of the basement and is controlled by regional tectonism that is associated with formation and evolution of the basin. Loading of the basement by water and sediments causes

further sinking of basement rocks into the mantle (Allen and Allen, 1990; Watts, 2001). Additional accommodation space can also be created in a basin by the dewatering and compaction of sedimentary succession under the load of the overburden with time. During the latter process, the volume of the basinal sediments is reduced as porosity decreases exponentially with burial depth.

A method is developed to systematically remove from successive layers in a basin the effects of sediment compaction and sediment and water loading so that the amount of tectonic subsidence can be determined. This process is known as "backstripping", which is developed based on the algorithms of Allen and Allen (1990) and Watts (2001). The technique presupposes that the way water and sediment loading deform the crust as well as the changes that take place during burial-related dewatering and sediment compaction are known (see Chapter 2). A MAC OS freeware program called OSXBackstrip which uses the procedure and algorithms developed by Allen and Allen (1990) and Watts (2001) is employed to determine regional tectonic subsidence rates in the Cilicia Basin.

The OSXBackstrip help text states that "*the simplest type of backstripping assumes that water and sediment loads are compensated locally by the displaced weight of a column of the weak mantle (the astenosphere), and that the porosity of the sediments decreases exponentially with depth. This type of backstripping is usually referred as to 1D Airy backstripping with exponential reduction of porosity*". OSXBackstrip uses 1D Airy backstripping, with exponential reduction of porosity, to extract the tectonic subsidence in sedimentary basins by progressively removing the effects of water and

sediment loading and compaction. The program consists of three modules: (i) an input module where the data are entered, (ii) a backstrip plot where the progressive decompaction of the sediments can be observed, and (iii) a tectonic subsidence plot where the total thickness curve, the decompacted curve, the curve corrected for sediment loading, and the "tectonic subsidence" curve are shown. The most critical of these three modules is the data entry module, which requires that the stratigraphy, water depths of deposition, paleosea-levels and changes of porosity with depth are known or estimated. In the following, the assumptions used in the OSXBackstrip are discussed. The program input requirements for each stratigraphic unit are:

- The unit base and top as depths in kilometres from a reference level
  - The present-day sea-level is taken as the reference surface datum.
- The age of the unit base and unit top in millions of years ago
  - The ages of the M-, A- and P-reflectors are taken as 5.3, 3.6 and 1.9 Ma, respectively.
- The sea-level at the time of deposition of the unit base and top in kilometres
  - As indicated in Assumption-9, the sea-level at 5.3 Ma (i.e. the first Pliocene sediments depositing over the M-reflector) and 3.6 Ma (i.e. the A-reflector) is assumed to be +25 m. It is assumed to be 0 m at 1.9 Ma. All data are relative to present-day sea-level.

- The water depth at the time of deposition of the unit base and top in kilometres

  o As discussed in Assumption-10 above, the seafloor morphology at the time of deposition of each stratigraphic unit is assumed to be of which is observed today.

- The mineral density in kg m^{-3}

  o The average mineral densities for the shelf and deep water sediments are calculated to be 2702.5 kg m^{-3} and 2713.0 kg m^{-3}, respectively.

- The porosity coefficient (C) in $kilometers^{-1}$

  o Based on the idealized porosity coefficient values (Sclater and Christie, 1980), the porosity coefficients for the shelf and deeper water sediments are estimated to be 0.410 km^{-1} and 0.486 km^{-1}, respectively.

- The surface porosity (Φ_0) as percent

  o The surface porosities for the shelf and deeper water for siliciclastic successions in the Cilicia Basin are assumed to be 52% and 62%, respectively (as discussed in Section 6.2.4).

- The type of setting of the basin (i.e. marine basin or continental)

  o The basin is assumed to have remained marine during the entire period between 5.3 Ma and the Present.

The subsidence rates calculated using the OSXBackstrip procedure are listed in Table 6.6. These results are further discussed in Chapter 7; Figure 6.23 gives the location of each subsidence calculation listed in Table 6.6.

In summary, the data presented in this chapter have allowed for a detailed sedimentological framework to be developed for the northeastern Mediterranean Sea, which in turn has allowed for the calculations of the sedimentation rates and basin subsidence rates in various time intervals. The implications of these results are analyzed in Chapter 7.

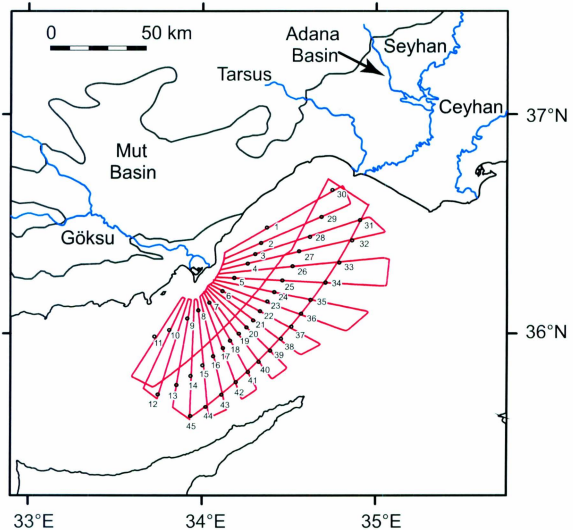

Figure 6.23 Station numbers for the locations in which subsidence calculations were taken (see Table 6.6).

Table 6.1 Matrix showing the X and Y coordinates with their corresponding two way times and interval velocities at locations that are used to determine the 3D velocity field. This table was later imported into TDExpress as an XYVT file where the seismic data were converted from the time to depth domain.

X-coordinate	Y-coordinate	Two-way time	Interval Velocity
559112.3	3974164.4	1350	1510
559112.3	3974164.4	1700	1650
559112.3	3974164.4	2060	1900
559112.3	3974164.4	2330	2400
609170	3958069.3	1025	1510
609170	3958069.3	1300	1675
609170	3958069.3	1400	1950
609170	3958069.3	1465	2450
640550.5	3990954.8	1015	1500
640550.5	3990954.8	1210	1680
640550.5	3990954.8	1505	1950
640550.5	3990954.8	1795	2400
613601.8	4016036	490	1495
613601.8	4016036	1025	1650
613601.8	4016036	1525	1900
613601.8	4016036	2030	2450
634801.3	4044181.8	233	1480
634801.3	4044181.8	600	1691
634801.3	4044181.8	1140	1945
634801.3	4044181.8	1550	2460

Table 6.2 Volume estimates calculated using the isopach maps presented in Figures 6.17-6.19. Intervals are described in Chapter 4. A= total sediment volume in cubic metres contained within noted intervals, B= porosity in percent of sediments (from Erickson, 1998), C= total volume of solids (i.e. A minus the volume of porosity), D= solid weight in kilograms (i.e. C * 2712 kg m^{-3}, average density from Schalter and Christie, 1980), E= solid weight in tonnes (i.e. D / 1000).

Interval	A	B	C	D	E
Seabed to P	4.98E+12	50	1.99E+12	5.40E+15	5.40E+12
P to A	5.72E+12	40	3.43E+12	9.31E+15	9.31E+12
A to M	8.45E+12	30	5.92E+12	1.60E+16	1.60E+13
M-Seabed	1.92E+13		1.13E+13	3.08E+16	3.08E+13

Table 6.3 Revised volume estimates calculated using Table 6.2 and the assumptions described in text. Intervals are described in Chapter 4. F= proportional contribution in percent by the Göksu River, G= proportional contribution in percent by the Seyhan, Ceyhan and Tarsus Rivers, H= solid weight in tonnes (E from Table 6.2), I= solid weight in tonnes contributed by the Göksu River, J= solid weight in tonnes contributed by the Seyhan, Ceyhan and Tarsus Rivers.

Interval	F	G	H	I	J
Seabed to P	30	70	5.40E+12	1.62E+12	3.78E+12
P to A	50	50	9.31E+12	4.65E+12	4.65E+12
A to M	70	30	1.60E+13	1.12E+13	4.81E+12
M-Seabed			3.08E+13	1.75E+13	1.32E+13

Table 6.4 K= Present-day sediment yields in tonnes per year (data from EIE 1982, 1984) for the Göksu Seyhan, Ceyhan and Tarsus Rivers, L= revised sediment yields in tonnes per year based on the assumption that 100% of the sediment yields of the Tarsus and Göksu Rivers and only 50% of the sediment yields of the Seyhan, and Ceyhan Rivers end up in the Cilicia Basin (see **Assumption-7**), M= revised sediment yields in tonnes per year based on the notion that 15% of the sediments contributed by these rivers are leaked out of the basin into the greater eastern Mediterranean Sea (see **Assumption-2**). SCT= Seyhan + Ceyhan + Tarsus.

	K	L	M
Göksu	2.54E+06	2.54E+06	2.16E+06
Seyhan	5.19E+06	2.60E+06	2.21E+06
Ceyhan	5.46E+06	2.73E+06	2.32E+06
Tarsus	1.29E+05	1.29E+05	1.10E+05
Total-SCT	1.08E+07	5.45E+06	4.64E+06

Table 6.5 K= Present-day sediment yields in tonnes per year (data from EIE 1982, 1984) for the Göksu Seyhan, Ceyhan and Tarsus Rivers, N= annual yields in tonnes per year of the Göksu River and the combined yields of the Seyhan, Ceyhan and Tarsus Rivers, O= the total volume of sediments in tonnes contained within the interval between P-reflector and the seabed, P= the total volume of sediments in tonnes contained within the interval between A- and P-reflectors, Q= the total volume of sediments in tonnes contained within the interval between M- and A-reflectors, R= the calculated annual sediment yield in tonnes per year for the sediments contained within the interval between P-reflector and the seabed, S= the calculated annual sediment yield in tonnes per year for the sediments contained within the interval between A- and P-reflectors, T= the calculated annual sediment yield in tonnes per year for the sediments contained within the interval between M- and A-reflectors, SCT= Seyhan + Ceyhan + Tarsus. Implications of the data presented in the table are discussed in Chapter 7.

	N	O	P	Q	R	S	T
Göksu	2.16E+06	1.62E+12	4.65E+12	1.12E+13	8.53E+05	2.74E+06	6.61E+06
SCT	4.64E+06	3.78E+12	4.65E+12	4.81E+12	1.99E+06	2.74E+06	7.79E+06

Table 6.6 Tectonic subsidence rate calculation results. U= station ID, V= the average tectonic subsidence rate for delta A in millimeters per year, W= the average tectonic subsidence rate for delta P in millimeters per year, X= the average tectonic subsidence rate for delta Q in millimeters per year, Y= the long-term average rate of subsidence calculated at each station in millimeters per year. Implications of the data presented in the table are discussed in Chapter 7.

U	V	W	X	Y
1	0.24	0.11	0.06	0.14
2	0.25	0.15	0.07	0.16
3	0.27	0.13	0.07	0.16
4	0.33	0.19	0.03	0.18
5	0.30	0.17	0.03	0.17
6	0.21	0.16	0.04	0.14
7	0.26	0.11	0.08	0.15
8	0.23	0.14	0.12	0.16
9	0.41	0.13	0.11	0.22
10	0.50	0.11	0.10	0.24
11	0.48	0.13	0.07	0.23
12	0.76	0.12	0.04	0.31
13	0.80	0.13	0.08	0.34
14	0.79	0.10	0.05	0.31
15	0.78	0.12	0.06	0.32
16	0.77	0.09	0.07	0.31
17	0.77	0.10	0.04	0.30
18	0.76	0.09	0.04	0.30
19	0.88	0.07	0.05	0.33
20	0.82	0.10	0.06	0.33
21	0.76	0.13	0.05	0.31
22	0.71	0.07	0.02	0.27
23	0.82	0.10	0.08	0.33
24	0.84	0.11	0.05	0.33
25	0.74	0.12	0.09	0.31
26	0.59	0.19	0.13	0.30
27	0.64	0.20	0.08	0.31
28	0.72	0.14	0.06	0.31
29	0.58	0.23	0.05	0.29
30	0.59	0.11	0.06	0.25
31	0.53	0.17	0.03	0.24
32	0.57	0.16	0.04	0.26
33	0.61	0.13	0.03	0.26
34	0.68	0.15	0.08	0.30

35	0.63	0.08	0.05	0.25
36	0.70	0.11	0.03	0.28
37	0.68	0.13	0.03	0.28
38	0.68	0.09	0.04	0.27
39	0.64	0.08	0.04	0.25
40	0.53	0.09	0.04	0.22
41	0.51	0.07	0.04	0.21
42	0.47	0.04	0.05	0.19
43	0.47	0.07	0.06	0.20
44	0.48	0.07	0.05	0.20
45	0.46	0.07	0.06	0.19

CHAPTER 7: DISCUSSION

The present-day tectonic framework of the northeastern Mediterranean is the result of the collision of the African, Eurasian and Arabian Plates in the Late Miocene, and the subsequent west-directed tectonic escape of the Aegean-Anatolian Microplate in the Pliocene-Quaternary (see Chapter 1; Şengör et al., 1985; Dewey et al., 1986). Today, the boundary between the African Plate and the Aegean-Anatolian Microplate is delineated by the Hellenic Arc and the Pliny-Strabo Trenches in the west and the Florence Rise, Cyprus Arc and the Tartus Ridge in the east. In the east, this zone of deformation is located south of the study area in a ~300-400 km wide zone around the arcuate SE-convex Cyprus Arc (Fig. 7.1; Robertson, 1998; Vidal et al. 2000a,b; Hall et al., 2005 a,b). This broad deformation zone extends further northwest as three well-defined SE-convex arcuate deformation fronts: (i) the Amanos-Larnaka fold-thrust belt, which extends from the Amanos Mountains of southern Turkey across the Latakia Basin into the Larnaka zone of eastern Cyprus, (ii) the Misis-Kyrenia fold-thrust belt, which extends from the Misis Mountains of southern Turkey to the Kyrenia Range of northern Cyprus, defining the boundary between the Latakia and Cilicia Basins and (iii) the Central Taurus Mountains of southern Turkey (Fig. 7.1). The study area is situated between two northern deformation fronts, namely the Misis-Kyrenia fold-thrust belt and the Central Taurus Mountains. Within this tectonic context, the Cilicia Basin can be viewed as an intramontane basin nestled on the backlimb of a huge thrust culmination that carries the Kyrenia Range and Misis Mountains.

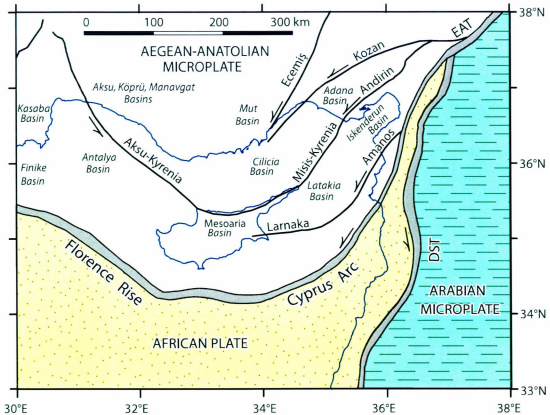

Figure 7.1 Schematic tectonic map showing the major tectonic elements of the northeastern Mediterranean Sea. DST = Dead Sea Transform Fault, EAT = East Anatolian Transform Fault (re-drawn from Aksu et al., 2005). Large arrows indicate sense of plate motion relative to a fixed Eurasian Plate; half arrows indicate half arrows indicate transform/strike-slip faults. The boundaries between the African, Arabian and Anatolian Plates are shown schematically.

The eastern Mediterranean Sea is the remnant of the Neo-Tethyan oceanic tract that once separated the Eurasian and African Plates (Şengör et al., 1985; Dewey et al., 1986). The convergence occurred by subduction of the intervening oceanic lithosphere and by squeezing of the microplates caught in between. During the Early-Middle Miocene there was a very large foredeep along this zone of convergence in front of the African Plate (Fig. 7.2; Yetiş et al., 1995; Robertson, 1998). This foredeep is the ancestral depocentre of all the isolated basins observed in the eastern Mediterranean today, including: the Adana, Cilicia, Cyprus, Iskenderun, Latakia, Mesaoria and Mut Basins (Fig. 7.2). Since the Miocene, the evolving regional tectonism caused the segmentation of this ancentral basin into a series of isolated depocentres, some of which were exhumed and incorporated into the orogens (e.g. the Mut Basin of southern Turkey).

During the Early-Mid Miocene the ancestral foredeep experienced a regional transgression that led to the deposition of a thick siliciclastic succession over the pre-Miocene basement rocks of the ancestral Taurides. In the Late Miocene, the region switched to a regional compression; this is the phase of deformation that resulted in the formation of the arcuate SE-convex fold–thrust belts described above, namely the Amanos-Larnaka and the Misis-Kyrenia fold-thrust belts (Fig. 7.1; Robertson and Woodcock, 1986; Robertson, 1998; Calon et al., 2005 a,b). This contractional phase led to the development of major culminations, which were located in central positions in these fold–thrust belts. The eastern segment of the southern deformation front evolved into the Amanos Mountains in the east and the Troodos Mountains in the west, with the Amanos-Larnaka zone in between. Similarly, the eastern segment of the central deformation front evolved into the Misis Mountains in the northeast and the Kyrenia

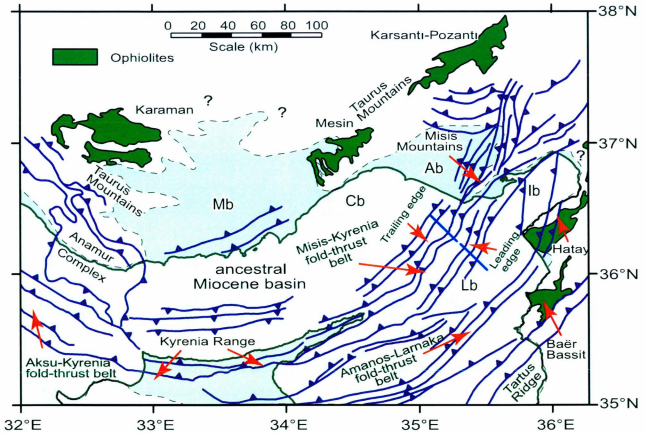

Figure 7.2 Map showing the approximate position of the ancestral basin which occupied the northeastern Mediterranean during the Early-Middle Miocene, compiled using published geological maps of Turkey (1:500,000 Adana Sheet, Ternek 1962) and Kouwenhoven and van der Zwaan (2006). The Miocene structures are from Aksu et al. (2005), and Aksu and Hall unpublished maps. Also shown are the major ophiolite successions. Ab = Adana Basin, Cb = Cilicia Basin, Ib = Iskenderun Basin, Lb = Latakia Basin, Mb = Mut Basin.

Range in the southwest, with the Misis-Kyrenia zone in between. The northernmost deformation front created the Central Taurus Mountains of southern Turkey (Fig. 7.1; Robertson, 1998). The Miocene structures that created the geology observed in the northeastern Mediterranean today are shown in Figure 7.2 from Aksu (2005) and Hall and Aksu (unpublished maps).

Within this large-scale tectonic framework, the following discussion is focused on two major themes: (i) the tectonic evolution of the Cilicia Basin and its onshore extension, the Adana Basin, and (ii) the assessment of the evolution of the Central Taurus Mountains, with special emphasis on the incorporation of the Mut Basin in the Tauride Orogen.

7.1 Tectonic evolution of the Cilicia Basin

Since the Miocene, the Cilicia Basin has developed as an arcuate and elongated depocentre that is situated between the Misis-Kyrenia range in the south and southeast and the Taurus Mountains in the north and northwest (Fig. 7.1). To the east, the Cilicia Basin merges with its onland extension, the Adana Basin (Burton-Ferguson et al., 2005), and to the west it is separated from the Antalya Basin by the north-south trending Anamur-Kormakiti Zone (Anastaskis and Kelling, 1991; Aksu et al., 2005).

The tectonic evolution of the Cilicia and Adana Basins is described within the framework of two main basin-bounding zones: the Ecemiş and Kozan Fault Zones to the north and northwest and the Misis-Kyrenia fold-thrust belt to the south and southeast (Aksu et al., 2005). The following subsections will briefly summarize previous works on these two fault zones, as well as present any new ideas derived from this study.

7.1.1 Bounding fault zones: Ecemiş and Kozan Fault Zones

The northwestern margin of the Adana-Cilicia Basins is bounded by a wide zone of deformation occupied by two major strike slip faults: the Ecemiş Fault Zone and the Kozan Fault Zone (Fig. 7.1). The Kozan Fault Zone is a splay of the Eastern Anatolian Transform Fault, whereas the Ecemiş Fault Zone is a splay of the North Anatolian Transform Fault (Perinçek and Çemen, 1990; Ergin et al., 2004; Aksu et al., 2005). The Kozan Fault Zone is one of a number of NE-SW- and broadly N-S-trending faults which splay from the East Anatolian Transform Fault (Fig. 7.1; Ergin et al., 2004). These splay faults all show variable strike-slip displacements. Among them are: the Yumurtalık Fault, which bounds the northern shores of the Iskenderun Basin; the Göksu Fault Zone, which defines the western margin of the Misis Mountains, and the Kozan Fault Zone, which delineates the northwestern edge of the Adana Basin (Fig. 7.1). Land studies show that a number of transtensional features have developed in the regions between these major fault zones, among which is the Adana Basin (Chorowicz et al., 1994; Burton-Ferguson et al., 2005).

Various previous studies documented the presence of significant left-lateral offsets along the Ecemiş Fault Zone associated with the Pliocene-Quaternary tectonic escape of the Aegean-Anatolian Microplate right-lateral North Anatolian Fault Zone and the left-lateral East Anatolian Fault Zone (Jaffey and Robertson, 2001; Umhoefer et al., 2007). These studies propose ~60 km of left-lateral offset from the Mid-Miocene – Quaternary on the Ecemiş Fault Zone. Literature is mute about the slip rates on the Kozan Fault Zone; however, the fault zone is clearly described as a left-lateral strike-slip structure (e.g. Ergin et al., 2004).

Field mapping and previous studies documented that the Kozan Fault Zone is a major structural element in the eastern Mediterranean, and it is an independent crustal feature located east and southeast of the Ecemiş Fault Zone (Şengör et al., 1985; Aksu et al., 2005). The data presented in this study (i.e. Chapters 4, 5 and 6) provide a unique opportunity to estimate the Pliocene-Quaternary slip rates for the Kozan Fault Zone, for the first time.

As detailed in Chapter 6, isopach maps were drawn to demonstrate the variation in thickness between the M- and A-reflectors, the A- and P-reflectors and the P-reflector and the seabed. Based on the arguments presented in Chapter 6 and through comparisons with seismic reflection profiles that show easterly-prograded delta packages, it was possible to delineate the extent of the Göksu River delta lobe during each time interval. The isopach map of the Early Pliocene interval (i.e. between M- and A-reflectors) shows a prominent, W-E-trending lobe that extends out from the NE-SW-trending shoreline of the Inner Cilicia Basin (Fig. 7.3). Comparison between the present-day mouth of the Göksu River and the locus of the Early Pliocene Göksu River delta lobe shows a surprising offset, with the lobe sitting significantly to the northeast (Fig. 7.3). An examination of the morphology of the adjacent landmass shows no evidence for a former river channel that would have explained this apparent offset and possible supply of sediments into the northwestern segment of the Inner Cilicia Basin (Fig. 7.4). The small rivulets that drain into the western Inner Cilicia Basin all have very small present-day drainage areas and water discharges and cannot account for the large sediment volume stored in the W-E-trending Early Pliocene lobe. Table 7.1 lists the drainage areas of the four largest rivulets that presently deposit sediments near the W-E-trending Early

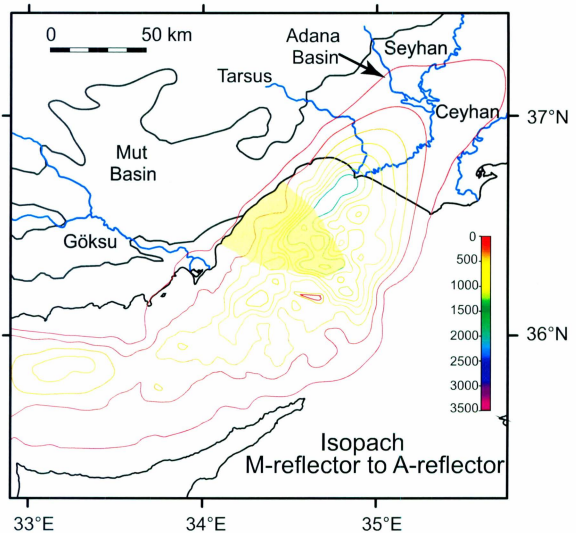

Figure 7.3 Isopach map of the Early Pliocene interval (i.e. Unit 1c, the sediments enclosed between the — and A-reflectors). Note that the postulated Göksu River delta lobe (highlighted in yellow) is notably offset from the present-day river mouth.

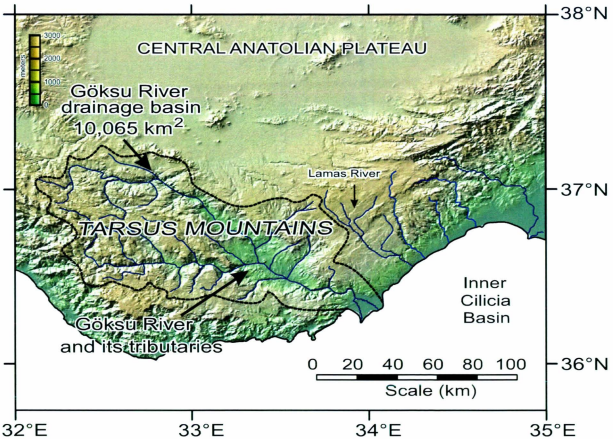

Figure 7.4 Morphology of the landmass surrounding the Inner Cilicia Basin. Note the prominent gorge cut into the Central Taurus Mountains by the Göksu River. Also note that there are several small rivulets northeast of the Göksu River, but they do not constitute major point source input into the Inner Cilicia Basin (also see Table 7.1). Digital seafloor topography from Smith and Sandwell (1997) and land elevation data from Global Multi-Resolution Topography (Ryan et al., 2009). Image from GeoMapApp (www.geomapapp.org).

Pliocene lobe. The largest of the four is the Lamas River, which has a drainage basin of 1026 km^2 (EIE, 1982, 1984). This drainage area is nearly 10 times less than the drainage area of the Göksu River at 10065 km^2 (see Chapter 6; EIE, 1982, 1984); thus it is not a major contributor to the sedimentary budget of the Inner Cilicia Basin. Apart from these small rivulets, there is no major river in this part of the study area other than the Göksu River, which can supply sediments to create the sedimentary architecture observed in the Pliocene-Quaternary isopach maps.

Comparisons between the Göksu River delta lobes associated with the three isopach maps of the Pliocene-Quaternary successions from oldest to youngest, (i.e. Fig. 7.3 = M- to A-reflectors, or "delta A"; Fig 7.5 = A- to P-reflectors, or "delta P"; and Fig. 7.6 = P-reflector to the seafloor, or "delta Q"), reveal that the locus of the progressively younger delta lobes are systematically located further toward the southwest, with the youngest lobe sitting immediately east-northeast of the present-day Göksu River mouth (also see Chapter 6). This displacement is best illustrated in Figure 7.7, where the topset-to-foreset transitions of the clearly east-prograded delta successions seen in the seismic reflection profiles are plotted on a map of the study area. The thicknesses are measured at each topset-to-foreset transition point. For example, a 580 m thickness is recorded in delta P, which represents the thickness of the delta successions between A- and P-reflectors as illustrated in Figure 7.8, at Fix position 1375. The thickest region of each delta package is marked by a "bulls-eye". Contours are drawn to contain the topset-to-foreset transitions, which when connected revealed a conservative estimate of the regional extent of the delta lobes associated with their respective deltas (Fig. 7.7). While the prodelta muds of each delta package must have extended much further into the Inner

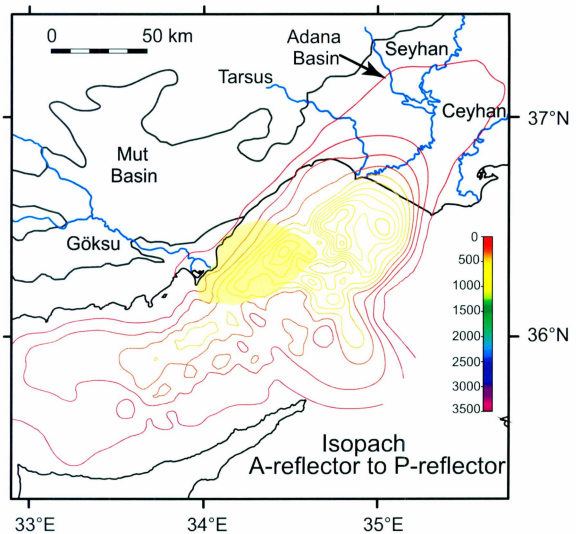

Figure 7.5 Isopach map of the Late Pliocene-Quaternary (i.e. Unit 1b, sediments enclosed between the A- and P-reflectors). The Göksu River delta lobe (highlighted in yellow) is shifted slightly toward the northeast from the present-day river mouth.

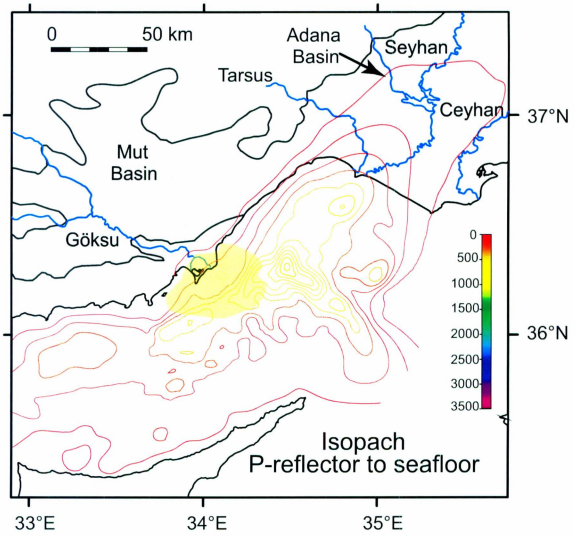

Figure 7.6 Isopach map of the Quaternary (i.e. Unit 1b, sediments enclosed between the P-reflector and the seafloor). Note that the youngest lobe is situated immediately seaward of the present-day Göksu River mouth.

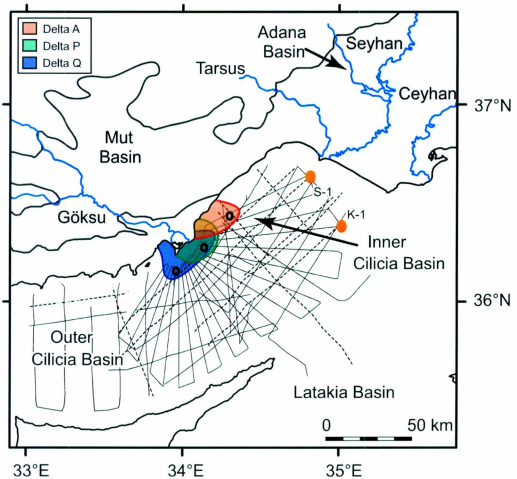

Figure 7.7 Map showing the regional extents of the topset-to-foreset transitions of deltas A, P and Q. The thickest regions in each delta lobe are marked with a "bulls-eye". Numbers adjacent to the contour lines represent the measured thicknesses in milliseconds of the delta successions beneath the topset-to-foreset transition of the uppermost prograded delta package associated with the time interval. For example, a 580 m thickness recorded in delta P represents the thickness of the delta successions between A- and P-reflectors in illustrated in Figure 7.8, at fix position 1375. See text for further detail.

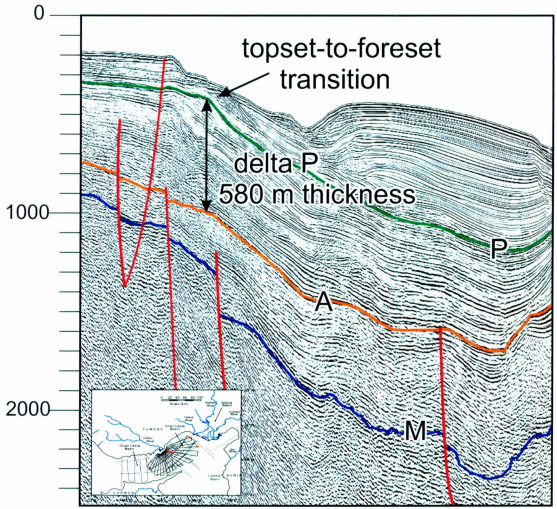

Figure 7.8 Multichannel seismic reflection profile illustrating the topset-to-foreset transition of the uppermost prograded delta package associated with the interval between the A- and P-reflectors. Location is shown as a red line in the inset.

Cilicia Basin, these conservative delta lobes provide the geometric relationships needed to determine the tectonic effects on delta sedimentation in the Cilicia Basin. Figure 7.7 clearly shows that the delta lobe and the thickest region of delta A (i.e. the lowermost delta, see Chapter 6) is situated in the Inner Cilicia Basin, whereas the delta lobes and their respective bulls-eye locations of the progressively younger deltas P and Q are systematically located further toward the southwest (Fig. 7.7).

The position and shape of the depositional lobes observed in the Pliocene-Quaternary isopach maps are a function of the interplay between supply from point sources (i.e. rivers) and the creation and/or destruction of accommodation space through geological times. Regional tectonic subsidence, dewatering and compaction, local tectonic events (i.e. roll-over and growth associated with the hanging wall of a listric normal fault, salt removal and progressive creation of a depletion syncline, various-sized graben formations, etc.) and a sustained rise in the sea-level can readily create geologically significant accommodation space. Conversely, regional tectonic uplift, local tectonic events (i.e. rotated and tilted footwall block of a fault, rise of salt and/or mud diapirs and walls, progressive development of fold/thrust belts, etc.) and a fall in global sea-level can destroy accommodation space. Channel avulsion and the associated lateral shifts in delta lobes is another important component that can lead to spatial changes in delta sedimentation. The spatial changes observed in the locus of the three Pliocene-Quaternary subunits must be evaluated within the context of the above factors.

The fact that there is a clear temporal shift of loci of the three Pliocene-Quaternary lobes suggest that either (i) the focus of deposition progressively shifted from the innermost northwestern portion of the Inner Cilicia Basin in the Early Pliocene

toward the southwest in the Mid-Late Pliocene and Quaternary or (ii) the point source of the lobes has not shifted, but the basin itself experienced tectonic movements, which rendered the observed morphology. The presence of marine Pliocene successions in the onland Adana Basin suggests that during the Pliocene, there must have been an ancestral bay in this region that was progressively filled by progradational delta sediments carried by the Seyhan, Ceyhan and Tarsus Rivers (Burton-Ferguson et al., 2005). However, the rugged shape of the coastline with the steep gradient of the Central Taurus Mountains and the very narrow strip of coastal plain between the Taurus Mountains and the Cilicia Basin continental shelf, collectively suggest that there was no major embayment in the course of the Göksu River that could have experienced a similar infill and progradation (Fig. 7.4). The deep gorge of the Göksu River and the absence of any similar gorges further to the north of the Göksu gorge strongly suggest that the Göksu River did not change its drainage pattern significantly during the entire Pliocene-Quaternary. These data can be used to confidently argue that any temporal shift in the loci of at least the two lowermost and firmly dated delta packages cannot be explained by the changes in accommodation space or channel avulsion through time, but must be explained by other factors. The only reasonable explanation remaining is the lateral shift of the Göksu delta lobes in time by tectonic movements, as further elaborated below.

Here, it is argued that the left lateral motions in the Kozan Fault Zone and possibly the Ecemiş Fault Zone are responsible for the progressive displacement of the Göksu delta lobes during the Pliocene-Quaternary (Fig. 7.7). The progressive displacement of the Göksu River delta lobes northeastward from the mouth of the Göksu River (Figs. 7.3, 7.5 and 7.6) allows for a conservative estimate of the amount of slip that

has taken place during the Pliocene-Quaternary. Assuming (i) that the lobes mapped in Figures 7.3, 7.5 and 7.6 can be confidently separated into contributions from the Göksu River (as also conservatively llustrated in Figure 7.7) versus contributions from the Seyhan, Ceyhan and Tarsus Rivers (see Chapter 6.2.3), (ii) that the Göksu River has not changed its course throughout the Pliocene-Quaternary and (iii) that there are no other rivers draining the Central Tauride Mountains of southern Turkey that can provide major contributions of sediment into the Inner Cilicia Basin (as described above), the amount of displacement along the Kozan Fault Zone can be determined. Sinistral strike-slip motions are required to systematically offset the lobes assigned to the Göksu delta during the Pliocene-Quaternary from where they were deposited at the mouth of the Göksu River (and gorge) to their present-day position.

The locus of delta Q is located immediately south of the present-day mouth of the Göksu River, suggesting that the river mainly prograded southward during the Quaternary. However, the topset-to-foreset transition map shows that the delta lobe extends quite considerably toward the northeast (Fig 7.7). The shelf around the present-day Göksu mouth progressively curves toward the northeast and the northeastern edge of the Göksu gorge is situated ~20 km northeast of the present day river mouth, suggesting that channel avulsion may have occurred during the Quaternary, spreading the delta sedimentation across a more broad area. The locus of delta P is situated seaward of the present-day mouth of the Göksu River, ~25 km northeast of the delta Q locus. The present-day position of the locus of delta P can be explained either by displacement along the Kozan Fault Zone and/or by natural shifts in the delta lobes associated with channel avulsion. This is because the Göksu gorge is in line with the locus of delta P, so it can be

argued that no displacement is needed along the Kozan Fault Zone. However, even if it is assumed that the position of delta P is only controlled by the channel position of the ancestral Göksu River, there still remains a notable offset of 20-30 km between the loci of deltas A and P, suggesting that the Kozan Fault must have offset the Göksu delta lobes from their point source at least by this amount in the Pliocene-Quaternary (Fig. 7.7).

If the above discussion is correct and that the locus of at least the lowermost Göksu River delta lobe has been progressively displaced by the Kozan Fault Zone during the Pliocene-Quaternary, an average slip rate can be calculated. Assuming that youngest sediments associated with delta A (i.e. the lowermost delta lobe which is demonstrably related to the ancestral Göksu River) were deposited at some 3.6 Ma and that the locus of this delta lobe during the time of deposition was located 20-35 km to the southwest, a conservative estimate of 0.6-1.0 cm/yr sinistral slip rate can be calculated for the Kozan Fault Zone in the Inner Cilicia Basin (Fig. 7.9). This rate is slightly higher than the 0.2 cm/yr slip rates calculated for the Ecemiş Fault Zone (e.g. Jaffey and Robertson, 2001), but the above rates for the Kozan Fault Zone are very comparable with the 1.0-2.4 cm/yr slip rates calculated for the North Anatolian Transform Fault Zone in northern Turkey (e.g. Polonia et al., 2004).

7.1.2 Bounding fault zones: Misis-Kyrenia Fault Zones

The southern and southeastern margin of the Cilicia-Adana Basin complex is bound by a broad zone of deformation known as the Misis-Kyrenia fold/trust belt (Aksu et al., 2005; Hall et al., 2005a). Examination of the seismic reflection profiles within the context of the structural and stratigraphic framework clearly shows that the evolution of

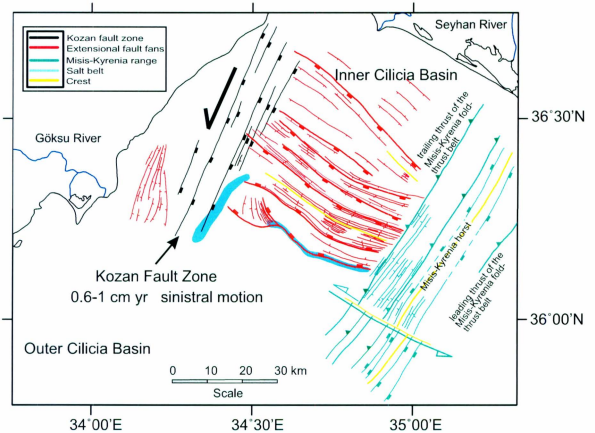

Figure 7.9 Tectonic map of the Inner Cilicia Basin showing the Pliocene-Quaternary faults mapped in this study. Note the postulated strike slip motion associated with the Kozan Fault Zone, as described in text (also see Figure 5.2 in Chapter 5).

the Misis-Kyrenia Zone is composed of two distinct sets of temporally separated structures: (i) a prominent E-verging fold-thrust belt that dominates the structure in the pre-Messinian successions; this is referred to as the Misis-Kyrenia fold-thrust belt (see Chapters 4, 5) and (ii) predominantly NE-SW-trending and respectively SE- and NW-dipping extensional faults that dominate the structural architecture of the Pliocene-Quaternary succession and are centered around a prominent horst block; this is referred to as the Misis-Kyrenia Fault Zone (see Chapters 4, 5).

The data in this region of the Inner Cilicia Basin is very sparse and the penetration of 2008 multichannel seismic reflection profiles is insufficient to clearly image the structures of the Misis-Kyrenia fold-thrust belt. A limited number of industry seismic reflection profiles show that the fold-thrust structures are truncated by the M-reflector (Chapter 5) and that these thrusts do not penetrate nor affect the Messinian successions (see also Aksu et al., 2005; Hall et al., 2005a; Calon et al., 2005b). Therefore, it is clear that during the pre-Messinian Miocene, an important E-verging fold-thrust belt evolved in this region and that the activity of this system ceased at the onset of the Messinian. The easterly vergence of the fold-thrust belt in the Miocene has been well documented by previous studies, including, Kelling et al. (1987) and Mulder et al., (1975).

The pre-Messinian tectonic evolution can still be determined by incorporating the existing industry multichannel seismic reflection profiles with the available literature. Previous studies have documented the presence of a narrow and deep foredeep in the eastern Mediterranean, immediately south of the Eurasian Plate margin (Robertson, 1998). This foredeep extended from the Antalya Basin in the west to the Bitlis Ocean in the east, the sediments of which now reside in the fold-thrust panels of the Bitlis-Zagros

suture (Fig. 7.1; Kempler and Ben-Avraham, 1987; Anastasakis and Kelling, 1991; Robertson, 1998). This foredeep was probably oriented in a more east-west direction in the Early Miocene, but assumed its present-day NE-SW orientation following the collision between the Eurasian Plate and the Arabian Microplate in the latest Miocene and Early Pliocene (Şengör et al., 1985).

The tectonic activity across the Misis Kyrenia fold-thrust belt was most pronounced during the Late Miocene, particularly in the Tortonian (Calon et al., 2005b; Hall et al., 2005a). It is noteworthy that the initial emergence of the fold-thrust panels in the Kyrenia Range of northern Cyprus as well as the Misis Mountains of southern Turkey took place in the Tortonian to Messinian interval (Calon, 2005a,b and the references herein). The collision between the Eurasian Plate and the Arabian Microplate in the latest Miocene is a significant milestone in the eastern Mediterranean geology (Şengör et al., 1985; Dewey et al., 1986; Robertson, 1998). Messinian is the short interval when the tectonic regime of the entire eastern Mediterranean Sea switched from predominantly southerly-verging folding and thrusting in the Miocene, into the regime dominated by partitioned strain with several crustal-scale transform faults controlling the west escape of the Aegean-Anatolian Microplate in front of the hard plate boundary of the African Plate in the south.

The development of the Misis-Kyrenia fold/thrust belt connecting the south-verging Kyrenia Range to the southeast-verging Misis Mountains partitioned the ancestral basin into the Cilicia, Adana and Mut Basins to the west and the Latakia, Iskenderun and Mesaoria Basins to the east (Fig. 7.1). During the Pliocene-Quaternary, the Misis-Kyrenia fold-thrust belt has been re-activated as a prominent strike-slip fault zone

accommodating components of the southern sector of the west escape of the Aegean-Anatolian Microplate (Aksu et al., 2005; Hall et al., 2005a,b). This prominent strike-slip fault zone is expressed as a major horst, which is centrally located over the Misis-Kyrenia fold-thrust belt, 10-20 km west of the leading thrust panel of the belt (Calon et al., 2005a).

7.1.3 Inner Cilicia Basin

The Inner Cilicia Basin and its onshore extension, the Adana Basin, reside on the backlimb of the Misis-Kyrenia fold-thrust belt (Williams et al., 1995). The history of the Inner Cilicia Basin can be traced back to its origination after the partitioning of the ancestral Miocene basin by the Misis-Kyrenia lineament. Following the sea-level low stand associated with the Messinian Salinity Crisis (Hsü et al., 1973, 1978), the Inner Cilicia Basin experienced a regional marine transgression in the Early Pliocene, leading to the deposition of mainly fine grained siliciclastic sediments. The transgression is evidenced by the progressive onlap of lowermost Pliocene successions onto the flanks of the basin (see Chapters 4-5; Williams et al., 1995; Aksu et al., 2005; Bridge et al., 2005; Burton-Ferguson et al., 2005). After the post-Messinian transgression, the region shifted its depositional style to the delta-dominated progradational system seen today (Aksu et al., 2005). The sediments that form the major deltaic wedge observed in the Inner Cilicia and Adana Basin complex are sourced from the Seyhan, Ceyhan and Tarsus Rivers to the northeast and the Göksu River to the northwest, all of which drain the evolving Taurus Mountains of southern Turkey (see Figure 7.1).

The Misis-Kyrenia paleohigh also developed during this period, partitioning the Cilicia and Latakia Basins. This barrier prevented significant sediment exchange between these two evolving basins, confining the sediments arriving from the north by the Tarsus and Seyhan (and probably periodically the Ceyhan), into the Cilicia Basin. During the Pliocene-Quaternary the deltaic successions of Unit 1 completely filled the Adana Basin, and are currently prograding into and largely filling the Inner Cilicia Basin in the west and the Inner Latakia Basin in the east (Aksu et al, 2005; Hall et al., 2005a; Burton-Ferguson et al., 2005). During the latter portion of Quaternary, the deltaic sediments overstepped the Misis-Kyrenia lineament (see Chapter 5).

Within the sedimentary delta wedge in the Inner Cilicia Basin, there exist several vertically stacked, seaward prograding delta packages that are separated from one another by shelf-crossing uncomformities (Aksu et al., 1992a,b and 2005), which were developed during the oscillating glacio-eustatic sea-level conditions of the Quaternary (Aksu et al., 1992a,b). At the southern Turkish margin the delta packages show clear east-progradation and must originate from the Göksu River (see Chapter 6), while at the southwestern Turkish margin the delta packages demonstrate southwest progradation and must originate from the Seyhan, Ceyhan or Tarsus Rivers (Chapter 6, Aksu et al., 2005). These delta packages coalesce in the central portion of the basin to reach a maximum thickness of well over 2 km (see Chapter 4). The infilling of the northern basin caused the locus of deposition to shift in a southwesterly direction during the Quaternary into the northernmost portion of the Outer Cilicia Basin (Aksu et al., 2005). In the Outer Cilicia Basin the Pliocene-Quaternary succession displays a sheet-like architecture with little to no observed deltaic packages sourcing from the northern margin (i.e. the Göksu River) or

the southern margin (i.e. the Kyrenia Range). This suggests that the Outer Cilicia Basin was filled by a long-distance transport of material from the toes of the larger prograded delta packages of the Seyhan, Ceyhan, Tarsus and Göksu Rivers to the northeast. Unlike the inner basin to the east and northeast which has been filling nearly to its brim, the outer basin is relatively starved of sediments with the thickness of Pliocene-Quaternary successions in the outer basin being drastically reduced to reach a maximum thickness of only ~1200 m (see Fig. 6.16, Chapter 6).

The observed architecture of tectonic elements in the Pliocene-Quaternary Cilicia Basin is mainly controlled by a linked thin-skinned extensional-contractional system detaching on Messinian salt and caused by the differential thickness of the overburden of sediments in the northern Inner Cilicia Basin compared to that of the southern Outer Cilicia Basin (Bridge et al., 2005). The region can be subdivided into two zones of deformation: (i) an extensional domain solely situated in the Inner Cilicia Basin, characterized by prominent listric fault fans and the associated salt rollers and (ii) a contractional domain situated within the Outer Cilicia Basin, characterized by active halokinetic tectonics, including diapirs and salt-cored growth folds, which are commonly associated with thrust faults (Aksu et al., 2005; Bridge et al., 2005). The boundary between these two domains lies at the transition between the inner and outer basins and is delineated by the presence of a very large salt wall (see Chapter 5). The Pliocene-Quaternary structures associated with this linked system are completely detached at a level that lies either within the salt or at its base, and pre-Messinian strata are not affected by the deformation linked to either the extensional or contractional regimes (Aksu et al., 2005; Bridge et al., 2005).

7.2 Subsidence rates in Inner Cilicia Basin

The subsidence rates calculated in Chapter 6 include long-term average rates for the entire Pliocene-Quaternary interval, as well as average subsidence rates for three stratigraphic units (sub-units 1A, 1B and 1C, correlating with the seismic interval of seabed to P-reflector, P- to A-reflectors, and A- to M-reflectors, respectively). It is important to recall that the calculated rates of subsidence removed the effects of the water and sediment loading as well as sediment compaction. Therefore, the rates of subsidence discussed in the following section are those solely attributed to the creation of accommodation space by tectonic subsidence and the infilling of this newly created space by the predominantly delta sedimentation.

7.2.1 Long term average rates of subsidence

Long-term subsidence rates calculated at 45 selected locations across the Cilicia Basin (Fig. 7.10) show that: (i) the rates of subsidence are highest along the central axis of the basin, decreasing toward the shallower shelves in the north/northwest and south/southeast and (ii) the rates of subsidence also show a progressive increase toward the centre of the Cilicia Basin from the west/southwest (i.e. Outer Cilicia Basin) and the east/northeast (i.e. Inner Cilicia Basin). These two trends parallel the increase in the total thickness of the Pliocene-Quaternary sediments across the Cilicia Basin (Fig. 7.10; see also Chapters 4 and 6). Seismic reflection profiles running nearly east-west across the western margin of the Inner Cilicia Basin (e.g. Lines 66, 68 and 70) show that morphologically the basin margin appears to have been downwarped, and that the deeper portion of the Cilicia Basin may have experienced higher rates of basin subsidence.

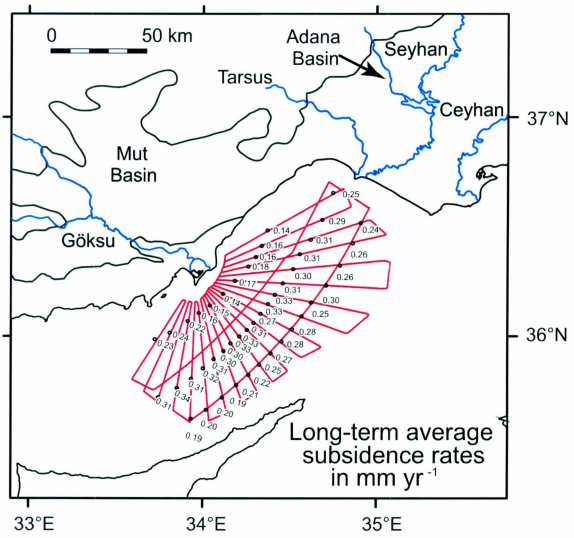

Figure 7.10 Variation in the long-term average subsidence rates for the entire Pliocene-Quaternary calculated using the backstripping method described in Chapter 6.

Indeed, the subsidence rates calculated using backstripping clearly documented that subsidence rates are noticeably higher in the deeper basinal setting than they are on the shallower regions of the northwestern Cilicia margin (Fig. 7.10; also see Chapter 6).

7.2.2 Temporal and spatial variations in the average rates of subsidence

Subsidence rates calculated for the specific stratigraphic intervals (Fig. 7.11 = sub-unit 1A correlating with the seismic interval of seabed to P-reflector, Fig. 7.12 = sub-unit 1B correlating with the seismic interval of P-reflector to A-reflector and Fig. 7.13 = sub-unit 1C correlating with the seismic interval of A-reflector to M-reflector) reveal the following salient features for the temporal tectonic evolution of the Cilicia Basin: (i) subsidence rates are notably high in the Early Pliocene and (ii) there is a dramatic decrease in the rate of basin subsidence from the Early Pliocene into the Late Pliocene where average rates fall by ~0.10-0.60 mm per year during the time interval, with further decrease in subsidence rate observed in the Quaternary.

Comparison between the isopach maps (i.e. Figs. 7.3, 7.5, 7.6) and the rate of subsidence maps (i.e. Figs. 7.11-7.13) clearly shows that the increase in the rate of subsidence from the peripheral edges of the basin toward the centre, as well as the notable increase in the rates of subsidence from the margin of the Cilicia Basin toward the deeper portion of the Cilicia Basin is associated with the increase in the thickness of the Pliocene-Quaternary deposits. However, as stated above, the calculated rates of subsidence removed the effects of the water and sediment loading as well as sediment compaction. Therefore, this notable correlation between the rate of subsidence and thickness of sediment is solely attributed to the creation of accommodation space by

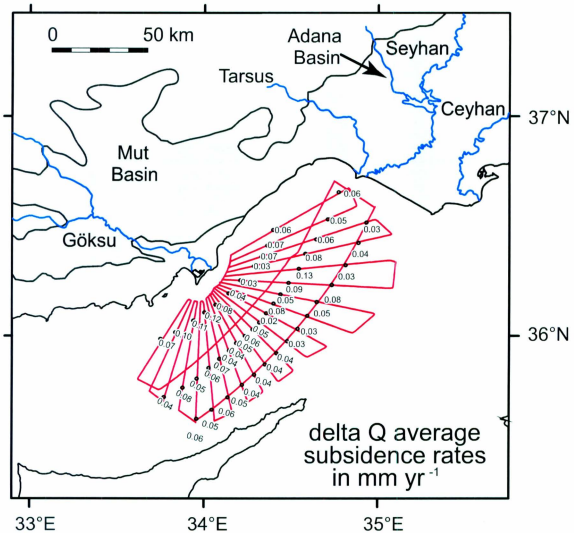

Figure 7.11 Average variation in the subsidence rates for the Quaternary interval (i.e. between the seabed and P-reflector) calculated using the backstripping method described in Chapter 6.

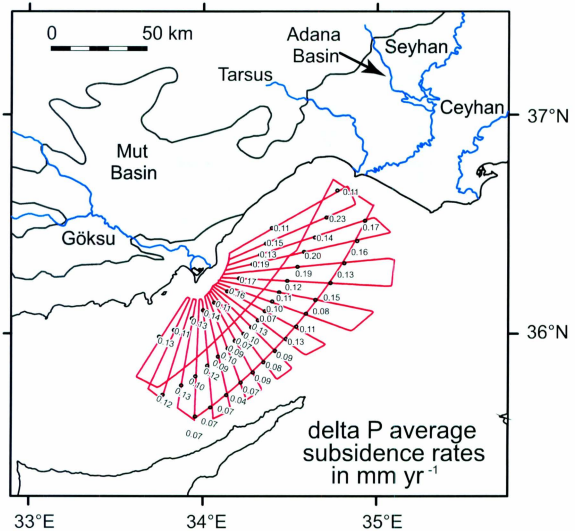

Figure 7.12 Average variation in the subsidence rates for the Mid-Late Pliocene-Quaternary interval (i.e. between the P- and A-reflectors) calculated using the backstripping method described in Chapter 6.

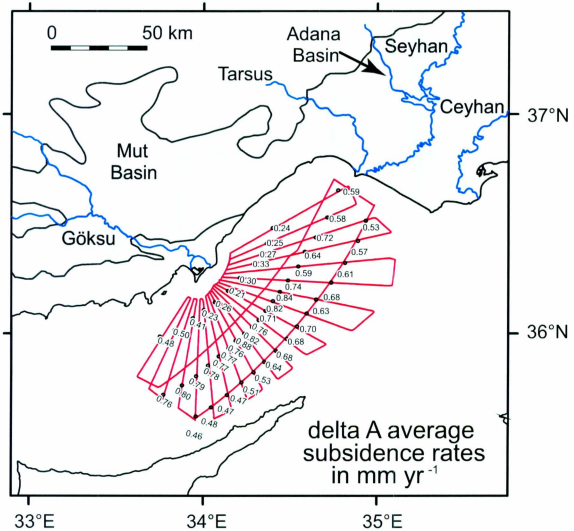

Figure 7.13 Average variation in the subsidence rates for the Early Pliocene interval (i.e. between the A- and M-reflectors) calculated using the backstripping method described in Chapter 6.

tectonic subsidence and the infilling of the newly created space by the delta sedimentation. This conclusion is very important, and highlights tectonic processes independent of sediment and water loading associated with the dramatic subsidence observed in the Cilicia Basin. The importance of this tectonic process becomes even more evident when viewed in relation to the dramatic uplift of the Central Taurus Mountains immediately north and northwest of the Cilicia Basin (see discussion below).

7.3 Analysis of sedimentary volumes

Three prominent seismic markers are identified and mapped across the entire Cilicia Basin, the M-reflector, the A-reflector and the P-reflector (see Chapter 4). Isopach maps of the successions bounded by these markers are compiled and their volumes are calculated; these calculations are presented in Chapter 6. In this chapter, the sediment mass estimates in the Cilicia Basin are evaluated using two approaches: (i) the solid sediment volume estimates contained in the isopach maps that are attributable to the Göksu River are compared with the sediment volume that would have been contained within the present-day Göksu gorge and (ii) the solid sediment weight estimates contained in the isopach maps are compared with the present-day sediment yields of the Seyhan, Ceyhan, Tarsus and Göksu Rivers to determine whether these solid sediment weights can be reconciled with the present-day annual sediment yields arriving into the Cilicia Basin. These results will then be used to evaluate the (i) rates of subsidence in the Cilicia Basin, (ii) rates of uplift of the adjacent land mass associated with the rise of the Taurus Mountains in the Pliocene-Quaternary, (iii) the transport of the erosional products into the Cilicia Basin, with emphasis on the age and rate of down-cutting of the Göksu

River and comparison between the erosional products originating from the excavation of the Göksu gorge and the deposition of sediments in the Cilicia Basin.

In Chapter 6, the total weight of the Pliocene-Quaternary sedimentary succession contained between the M-reflector and the present-day seafloor is calculated to be 3.00 x 10^{13} tonnes. Also in Chapter 6, a number of assumptions are discussed so as to account for the weight of the sediments contributed solely by the Göksu River. Based on these assumptions, the weight contributed by the Göksu River is estimated to be 1.71 x 10^{13} tonnes. The present-day total sediment yield of the Seyhan, Ceyhan, Tarsus and Göksu Rivers is 1.33 x 10^{7} t yr^{-1} with a total sediment expected to deposit in the Cilicia Basin of 6.79 x 10^{6} t yr^{-1} (i.e. 15% loss to suspended sediment transport, and only proportional supply by the Seyhan and Ceyhan Rivers – see Chapter 6). Assuming that this rate of yield is representative of the entire Pliocene-Quaternary, the total yield of sediments by these four rivers during the last ca 5 Ma would be 3.40 x 10^{13} t. The total weight of sediments contained within the total isopach map of the Pliocene-Quaternary (i.e. between M-reflector and seafloor) is 3.00 x 10^{13} t, which is remarkably similar to the amount of sediment yield by the four major rivers. Thus, it is comforting to see that the four major rivers appear to provide today sufficient sediment supply to account for the thick Pliocene-Quaternary deposition in the Inner Cilicia Basin.

7.3.1 Sediment volumes in isopach maps versus Göksu gorge

The total volume of the Göksu gorge was calculated and kindly provided by Dr. Cenk Yaltırak using Global Mapper (a GIS software) following the technique outlined: cross-sectional profiles are constructed every 50 m at elevation increments for

the Göksu gorge and their surface areas are calculated starting from the shoreline and ending at the highest elevation of the valley floor over the Central Taurus Mountains at ~1500 m. The areas of the incremental slices were multiplied by 50 m elevations to achieve volume slices. The 1500 m elevation is taken to be the most conservative elevation where the drainage divide occurs in the region. The volume of the area within the 1500 m elevation draining into the Göksu gorge is then calculated. The resultant volume of the Göksu gorge is 3506 km^3.

The assumptions discussed in Chapter 6 indicated that the total weight of solid sediment in the Cilicia Basin that can be attributed to transportation by the Göksu River in the last 5 Ma is 1.71 x 10^{13} t, or 6305 km^3. Recall that sedimentary weights are converted into volumes using the average mineral density of 2712 kg m^3 (Chapter 6). Assuming that the present-day Göksu gorge is created due to down-cutting by the Göksu River during the last ~5 Ma, the total volume of the sediments that would have been contained within the gorge would only account for ~32% of the total sediment volume calculated for the Cilicia Basin. The rocks contained within the gorge must also contain variable amounts of porosities. The geological map of the Göksu gorge shows that the rocks in this area consist of Paleozoic and Mesozoic carbonates and ophiolitic successions overlain by Oligo-Miocene sedimentary successions, with the older rocks being notably exposed in the deepest portion of the gorge (Fig. 6.9, Chapter 6). There is no field data available on the porosities of rocks within the Göksu gorge. However, considering the fact that the ophiolitic rocks have very low porosities, but carbonate and siliciclastic rocks have relatively higher porosities, an average 5% porosities can be taken for the rocks excavated from the Göksu gorge. The porosity-reduced new volume of the

Göksu gorge is 3330 km^3. The exercise of comparing porosity-reduced solid sediment volume contained within the Göksu gorge and the porosity-reduced solid sediment volume contained within the Cilicia Basin accounts for ~53% of the sediment yield that can be readily attributed to the Göksu River alone.

It is clear that the Göksu River must have supplied much more than the sediments contained within the Göksu gorge. During the last 5 Ma, the landmass containing the Göksu River must have also experienced denudation (i.e. deflation of the landmass by various weathering processes). The denudation rate is a function of: the type of climate and rainfall the rock succession resides, the amount of tectonic uplift (or subsidence) of the region, the type of rocks present, etc. The Cilicia Basin and the Central Tauride Mountains have been situated in a temperate Mediterranean-type climate since the Miocene; thus denudation is expected to be an important factor contributing to sediment supply. A quick review of the literature shows that in zones of temperate climate with medium rainfall, continental denudation rates range between 20 and 50 mm per ka for carbonate-dominated succession (Einsele, 1993). In mountainous regions dominated by higher rainfall in temperate climates the denudation rates can vary between 50 mm per ka and 150 mm per ka, again for carbonate-dominated sedimentary successions. Variable lithologies of rock associated with carbonate successions have also been reported to have denudation rates ranging from 18-37 mm ka (Einsele, 1993). A conservative estimate of denudation rate of 20 mm per ka would amount to an additional 100 m of deflation of the Mut Basin across the drainage area of the Göksu River. It is difficult to estimate the drainage area of the paleo-Göksu River. However, if we assume that the average drainage area of the Göksu River has been comparable to the present-day drainage area of

the river, an additional 985 km^3 of sediments must have been supplied to the Göksu River from the larger drainage area arising from denudation. This additional sediment weight would account for ~16% of total sediments in the Cilicia Basin, which can be attributed to the Göksu River. A similar calculation with a more realistic rate of denudation of 50 mm per ka reveals a volume of 2459 km^3, accounting for ~39% of the sediment volume that can be attributed to the Göksu River.

These back-of-the-envelope calculations can be used to validate the assumptions presented in Chapter 6, which are used to separate contributions of sediment into the Cilicia Basin from the Göksu River versus the Seyhan, Ceyhan and Tarsus Rivers. The above calculations clearly illustrate that the sediments contained in the isopachs can be accounted for by the Göksu River gorge plus its inferred denudation, accounting for ~92% (53% gorge + 39% denudation) of the sediments contained within this basin that have been attributed to the Göksu River. The remainder of sediments must have come from the north from the Seyhan, Ceyhan and Tarsus Rivers.

7.3.2 Sediment weights versus present-day sediment discharges

The solid sediment weight estimates contained in the isopach maps are compared with the present-day sediment yields of the Seyhan, Ceyhan, Tarsus and Göksu Rivers to determine whether these solid sediment weights can be reconciled with the present-day annual sediment yields arriving into the Cilicia Basin. The weight of sediments contained in each interval was converted into an average annual sediment yield by dividing the total weights contained in each interval by the time elapsed during this interval. These rates are then compared with the present-day annual sediment yield of the

Göksu River. For example, the weight of sediments contained within the interval bound by the seabed and the P-reflector is 1.58 x 10^{12} tonnes, with the total time elapsed being 1.9 Ma (i.e. P-reflector is dated as 1.9 Ma, see Chapter 4). This corresponds to an average annual sediment yield of 8.33 x 10^{5} tonnes/yr. Similarly, the weight of sediments contained within the interval bound by the A-reflector and the P-reflector is 4.55 x 10^{12} tonnes, with the total time elapsed being 1.7 Ma (i.e. the A-reflector age of 3.6 Ma minus the P-reflector age of 1.9 Ma, Chapter 4). This corresponds to an average annual sediment yield of 2.67 x 10^{6} tonnes/yr. Finally, the weight of sediments contained within the interval bound by the M-reflector and the A-reflector is 1.10 x 10^{13} tonnes, with the total time elapsed being 1.7 Ma (i.e. the M-reflector age of 5.3 Ma minus the A-reflector age of 3.6 Ma). This corresponds to an average annual sediment yield of 6.45 x 10^{6} tonnes/yr.

Recall that the present-day rate of sedimentation by the Göksu River is reported to be 2.16 x 10^{6} tonnes/yr (see Chapter 6). These results show that average annual sediment yields by the Göksu River in the Early Pliocene were triple what is observed today. There are several factors that might have caused the observed high annual sediment yields in the Early Pliocene and much reduced yields in the Late Pliocene-Quaternary-Recent: (i) the extent of the source area drainage basin was much greater in the Early Pliocene, but it became progressively smaller toward Recent, and/or (ii) the water and sediment discharge rates of the former Göksu River were significantly larger in the Early Pliocene but decreased toward Recent, and/or (iii) rate of uplift was greater in the Early Pliocene and notably decreased toward the Recent.

There are no data available in the literature on the size and extent of the Pliocene drainage area of the Göksu River. The complicating factor here is that the present-day Central Taurus Mountains did not exist, but were evolving during the Early Pliocene. Thus, the drainage basin was also developing and changing as the Taurus Mountains were forming. There is no previous study on the timing of development of the ancestral Göksu River. The high-resolution seismic reflection data show no evidence for an east-prograded package within Messinian successions of Unit 2, immediately below the M-reflector. If there was an ancestral Göksu River during the pre-Messinian, this river channel would have been deeply excavated during the Messinian salinity crisis, when the sea-level in the Mediterranean fell below 2000 m. The absence of a deeply incised channel also corroborates that the drainage area of the ancestral Göksu River was smaller in the Early Pliocene. Therefore, it is not likely that the former drainage basin was significantly larger to account for the 3 times higher average annual sediment yield given above (also see Chapter 6). There is also no evidence in the literature to suggest the evolving Central Taurus Mountains were significantly more pluvial in the Early Pliocene than they are today. However, the rise of the Central Taurus Mountains invariably must have created rain-shadows which would have created aridity in the evolving Central Anatolian Plateau but increased precipitation along the southern margin of the mountains. Thus, some increase in river discharge may have occurred through Pliocene to Recent as the Taurus Mountains evolved. The fact that the average annual sediment yield estimates in the three key intervals show a progressive decrease with time suggest that there must have been a stronger underlying process responsible for the observed trends.

The only remaining explanation for the observed trend of a ~3 times greater annual average sediment yield in the Early Pliocene compared to the present-day is the rapid rise of the Central Taurus Mountains during the Early Pliocene. The chronostratigraphic data from the Mut Basin shows that the region was a shallow water marine environment during the Late Miocene (i.e. Tortonian Chapter 4), but became emergent in the latest Tortonian to Messinian (Cosentino et al., 2012). From the Messinian to the Recent, the former marine Mut Basin rose ~2000 m, becoming nestled in the Taurus Mountains (Bassant et al., 2005; Cosentino et al., 2012; Schildgen et al., 2012). This rapid rise would have changed the equilibrium profile of the developing Göksu River, forcing the river to rapidly down-cut its channel and carry the erosional products into the Cilicia Basin. It is interesting to note that during this period the Cilicia Basin itself experienced a protracted subsidence which created the necessary accommodation space for the incoming sedimentary supply.

7.4 Uplift rates along the Taurus Mountains and the Mut Basin

On the basis of biostratigraphic and paleomagnetic data, Cosentino et al. (2012) have assigned ages of 8.35 – 8.108 Ma for the upper part of the undeformed marine deposits that cap the southern margin of the Central Anatolian Plateau (i.e. the Mut Formation of the Central Taurus Mountains). This age is notably younger than previously reported by Bassant et al. (2005), who estimated that the sediments of the Mut Basin were of Langhian age (15.97 – 13.65) or by Tanar and Gökçen (1990), who identified these sediments as Serravallian (13.65–11.61 Ma). Cosentino et al. (2012) further indicated that these earlier age estimates are not incorrect, but represent ages from the lower portion of the stratigraphy created by variably cut erosion across the southern flanks of

the Central Taurus Mountains.

The timing of the initiation of the rise of the Taurus Mountains is controversial. In the Ecemiş, Karsantı and Aktoprak Basins of the Central Anatolian Plateau, the onset of the exhumation of the Central Taurus Mountains occurred between the Late Oligocene and Early Miocene (Jaffey and Robertson, 2005). In the Mut Basin, the cessation of the marine sedimentation and onset of exhumation is dated as ~8 Ma age (Cosentino et al., 2012). Furthermore, the highest subsidence in the Adana Basin occurred at ~5.45-5.33 Ma (Cosentino et al., 2010) and was associated with the sedimentation of >1000 m of fluvial conglomerates and marls of the Handere Formation (i.e. the late Lago Mare episode of the Mediterranean Basin). This interval is also coeval with the rapid subsidence in the Cilicia Basin, and was probably connected with the onset of the rise of the Central Taurus Mountains, as also suggested by Cosentino et al. (2012) and Schildgen et al. (2012).

Recent studies by the Vertical Anatolian Movements Project (VAMP) showed that the former Mut Basin experienced a regionally variable uplift, with the highest former marine sediments capping the southern margin of the Central Anatolian Plateau, at ~2 km elevation (Cosentino et al., 2012; Schildgen et al., 2012). While these regions were exhumed and uplifting and eroding, data showed that the southern margin of the orogen was still receiving marine sedimentation (Yıldız et al. 2003). In a multidisciplinary study of biostratigraphic and isotope geochemistry, Schildgen et al. (2012) showed that the youngest and highest marine sediments in the Mut Basin signal the onset of the surface uplift starting sometime between 8 and 5.45 Ma. Cosentino et al. (2012) reported a biostratigraphic age of ca. 8 Ma for marine sediments that cap the southern plateau

margin at ca. 2 km elevation. Based on this elevation, these authors suggested that the region experienced an average long-term uplift rate of 0.25 and 0.37 mm/yr. Southeast of the town of Mut, in the southeastern Göksu gorge, the younger marine sediments of Pliocene to Pleistocene age onlap the Middle to Late Miocene marine succession of the Mut and Köselerli formations. These deposits are now situated at ~1.2 km elevations (Yıldız et al., 2003). Data from the younger marine successions suggested that on the backdrop of the average long-term uplift rates, the average post-Early Pleistocene surface uplift rates were much higher at ~0.7 mm/yr (Schildgen et al., 2012). Furthermore, cosmogenic ^{10}Be, ^{26}Al and ^{21}Ne exposure ages on a series of fluvial strath terraces from ca. 150 to 30 m above the thalweg of the Göksu River showed that the incision rates within the Göksu gorge ranged from 0.6 to 0.7 mm/yr in the last ca. 200 ka to 30 ka (Schildgen et al., 2011; 2012). These authors further suggested that there is good agreement between the terrace-derived incision rates and the post-early Pleistocene uplift rates.

Recent work comparing this record of surface uplift to the subsidence and uplift history of the Adana Basin, located south of the southern margin of the plateau (Radeff et al., 2011, EGU General Assembly), gives clues to spatial patterns of uplift. Initial uplift of the southern margin after 7 to 8 Ma was associated with subsidence of the Adana and Cilicia Basins, while later margin uplift was coupled with uplift of the Adana Basin.

7.5 Source to Sink: uplift of Mut Basin and subsidence of Adana – Cilicia Basins

In the central segment of the Cilicia Basin, the long-term average tectonic subsidence rate is ~0.31 mm/yr. In the onland Mut Basin, the average long-term uplift

rates range from 0.25 mm/yr to 0.37 mm/yr. These data clearly show that while the Central Taurus Mountains were rising, there was concomitant subsidence in the Cilicia Basin. The 0.31 mm/yr average long-term subsidence would translate to ~1.6 km of tectonic subsidence since the Messinian. Indeed, the prominent Messinian M-reflector in this sector of the Cilicia Basin is situated between 2 and 3 km below the present-day sea-level. While the basin had an inferred morphology during this time, the remaining excess depth of the top Messinian strata beyond what is predicted by the subsidence calculations is the result of additional subsidence due to sediment loading and the associated compaction. It is clear that there was a sharp tectonic boundary between the rising Taurus Mountains in the north/northwest and the sinking Cilicia Basin in the south/southeast.

The rate of incision calculated for the last Göksu gorge ranged from 0.6 to 0.7 mm/yr during the last ca. 200 ka to 30 ka (Schildgen et al., 2011; 2012). If these rates were to be taken as representative for the Pliocene-Quaternary, the time needed for the excavation of the ~1500 m height of the Göksu gorge can be calculated as ~2.1-2.5 x 10^6 years. This calculation shows that either the Göksu River started its excavation sometime in the Late Pliocene, some 2.5 Ma, or that these rates are underestimated to explain the excavation of the Göksu gorge. The fact that the oldest delta progradation that can be unequivocally related to the ancestral Göksu River sits above the M-reflector, with its latest topset-to-foreset successions occurring immediately below the A-reflector (Fig. 7.14) negates the late initiation of the Göksu River, leaving us with the only possible explanation that the incision rates must have been higher in the Early Pliocene.

The basin morphology is controlled by an intimate interplay between the rate of sediment supply to the basin and the rate of creation of accommodation space. The rate

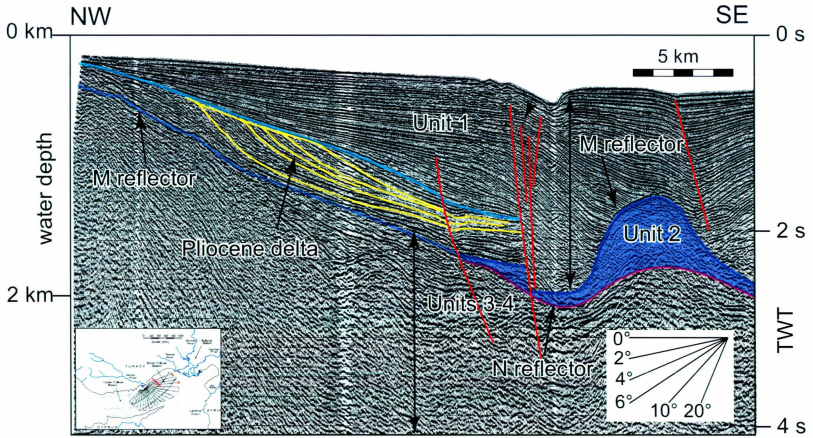

Figure 7.14 Industry multi-channel seismic reflection profile showing the easterly-prograded thick delta succession sitting immediately above the M-reflection in the Inner Cilicia Basin. Location is shown in inset in red.

of sediment supply is in turn a function of the rate of uplift, thus in turn the rate of incision by the rivers. If the rate of subsidence was less than the rate of uplift, then the basin would have been quickly filled with the incoming sediments to its brim and the marine Cilicia Basin would have been lost. If the rate of uplift was much less than the rate of basin subsidence, then the basin would have starved and there would not have been enough sediment to fill the basin. The data presented in this thesis clearly show that a substantial amount of sediment has been eroded from the rising Central Taurus Mountains and was transported by the Göksu River into the Cilicia Basin. It is also clear that the Cilicia Basin was subsiding by a sufficient amount to accommodate this great load of incoming sediment. In the Inner Cilicia Basin, the sedimentation has nearly completely filled the pre-existing and subsiding basin; however, in the Outer Cilicia Basin, the absence of sufficient sedimentary input has rendered the basin to be starved; the basin occurs in ~1000 m water depth with only ~500 m of Pliocene-Quaternary sediments.

7.5.1 M-reflector to A-reflector

Following the termination of the Messinian Salinity Crisis ca. 5.3 Ma, the marine sedimentation in the Mut Basin had already ceased and the region became emergent; this phase is associated with the early rise of the Central Taurus Mountains. The ancestral Göksu River developed during this time and started to drain the emerging landmass, transporting its loosely consolidated material into the adjacent Cilicia Basin. With time, a prominent delta lobe developed in the Cilicia Basin; this lobe is clearly identified and mapped in seismic reflection profiles. The sustained delta progradation observed in this Early Pliocene delta lobe suggests that the delta sedimentation is associated with the

substantial rise of the Central Taurus Mountains and incision/denudation of the landmass. Indeed, studies on the onland Mut Basin confirm that during the Miocene (~8 - 5.45 Ma) there was a rapid rate of uplift of the Mut Basin and the evolving Central Taurus Mountains.

7.5.2 A- to P-reflectors

Seismic reflection profiles suggest that delta sedimentation continued during the Mid-Late Pliocene. However, the tectonic subsidence rates calculated by the backstripping method show that the rate of subsidence decreased significantly since the Early Pliocene delta development. Sediment volume calculations based on isopach maps show that there was a noticeable decrease in the rate of sediment supply into the basin during this time. This dramatic reduction of sediment input could be attributed to the fact that the loose, easily erodible material consisting of Miocene sediments was already stripped from the Göksu River gorge and its tributaries, and that the river was now cutting into consolidated Eocene sedimentary and crystalline Mesozoic and Paleozoic successions as well as ophiolitic successions; therefore the supply into the Cilicia Basin is considerably diminished (see geological map, Fig. 6.9). The most recent onland studies on the Mut Basin are mute regarding the temporal changes in rate of uplift during this interval.

7.5.3 P-reflector to seabed

This interval is characterized by a series of east-directed stacked, seaward prograded clinoform packages, suggesting significant delta progradation from the Göksu River during this time. But, the volume calculations based on the isopach maps suggest

there is even less sediment coming in to the basin than during the previous interval. This pattern mimics the results of the subsidence rate calculations, as tectonic subsidence is even further reduced during this interval. This reduction in the sedimentation rate can be explained in a similar manner in that the river is encountering difficult-to-erode rock successions (also see Fig. 6.9). Schildgen et al. (2011, 2012) suggested that between 1.66 Ma to 1.62 Ma there was a notable increase in the rate of uplift to about 0.72-0.74 mm/yr when compared to the average long-term uplift rate of 0.25-0.37 mm/yr. The marine data from the Cilicia Basin does not have the chronological detail needed to evaluate the response of sedimentation to this uplift.

There are several questions that naturally arise from the observations presented in this chapter:

- Is there a linkage between the uplift of the Mut Basin and the subsidence of the Cilicia Basin?
- Is the flexural loading of the crust associated with the rise of the Central Tauride sufficient to account for the observed tectonic subsidence in the Cilicia Basin?
- Are the differential slip rates between the North Anatolian Transform Fault, East Anatolian Transform Fault and the Dead Sea Transform Fault the fundamental cause of the rapid subsidence in the Cilicia Basin?

These questions are beyond the scope of this thesis, and may be the foci of future studies involving geodynamic modelling.

7.6 Comparisons between the evolutions of the Cilicia Basin and Rhodes, Finike, Aksu, Köprü and Manavgat Basins

The latest Miocene evolution of the ancestral basin that occupied the present-day Adana-Mut-Cilicia Basins and the Pliocene-Quaternary partitioning of this ancestral basin can be readily compared with the evolution of several basins similarly situated along the Taurus Mountains of southern Turkey. Two main comparisons are worth making: (i) the onland Kasaba Basin and the marine Finike Basin and Rhodes Basin to the west, and (ii) the onland Aksu, Köprü and Manavgat Basins and the offshore Antalya Basin (Fig. 7.15).

In two comprehensive companion studies, east of the study area, the mechanism of very rapid Pliocene-Quaternary subsidence in the Rhodes and Finike Basins is explained by the flexural loading of the crust associated with the major thrusts that carry the western Taurus Mountains (Aksu et al., 2009; Hall et al., 2009). These studies suggested that progressive thrusting associated with the southwest migration of the Anatolian block accelerated basin development. They pointed out that the compression resulting in southward thrusting of the Taurus Mountains could account for the uplift of the Serravallian-Langhian marine sediments in the Kasaba Basin and complementary subsidence in the adjacent Rhodes and Finike Basins (Hall et al., 2009; Aksu et al., 2009). Until the end of Serravallian-Langhian the Kasaba Basin was a marine depocentre in front of the evolving Taurus Mountains (Hayward, 1984; Şenel, 1997a,b; Şenel and Bölükbaşı, 1997). During the late Miocene the progressive uplift of the region associated with the rise of the Taurus Mountains caused the former marine depocentre to become nestled on the foothills of the present-day Taurus Mountains. Aksu et al. (2009) and Hall

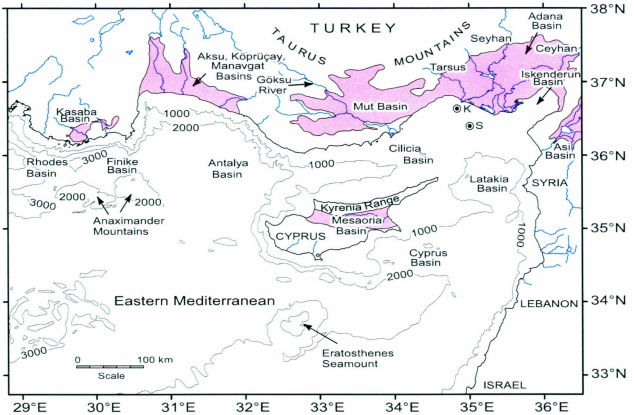

Figure 7.15 Index map of the eastern Mediterranean highlighting the locations of linked onland marine Miocene basins and their conjugate marine basins in the eastern Mediterranean Sea. These basins were once a shared depocentre but became partitioned with the rising regional orogens.

et al. (2009) carried out simple calculations of thrust loading with the assumption of a simple isostatic response of a lithosphere with high flexural rigidity to suggest that approximately 6 km of crustal thickening caused by thrusting in southwestern Turkey would result in ~1 km of uplift above the thrusts: they further showed the now uplifted Kasaba Basin as an example for the uplift and the 5 km of subsidence in the Rhodes and Finike Basins.

Similarly, there are three large depocentres which are nestled on the southern fringes of the central Taurus Mountains: the Aksu, Köprü, Manavgat Basins. During the Miocene, these depocentres were part of the larger ancestral marine Antalya Basin. In the Aksu, Köprü, Manavgat Basins, marine deposition continued all the way to the Tortonian, represented by the siliciclastic Karpuzçay Formation (Akay and Uysal, 1985). These Miocene marine basins progressively become terrestrially exposed during the latest Miocene as indicated by the shoaling upward succession of the Gebiz Formation, which is characterized by the anhydrite- and selenitic gypsum-bearing siliciclastic deposits (Akay and Uysal, 1985). It is only in the latest Messinian that the Aksu, Köprü, Manavgat Basins became terrestrial (Akay and Uysal, 1985; Akay et al., 1985; Turkish Petroleum Corporation, unpublished data). Thus, the partitioning of the ancentral marine depocentre into now onland Aksu, Köprü, Manavgat Basins and the present-day marine Antalya Basin took place during the latest Miocene and early Pliocene. This fragmentation of the ancestral basin is associated with the rise of the Central Taurus Mountains. In fact, large thrusts have been imaged in recent seismic reflection profiles in the Antalya Basin (Işler et al., 2005; King, in progress; Gogacz in progress), further corroborating the notion that the large separation between the subsided successions in the

present-day marine setting and the uplifted former marine successions can be explained by loading associated with these major thrusts, as described in the Finike and Rhodes Basins (Aksu et al., 2009; Hall et al., 2009).

The above scenarios (i.e. the partitioning of the Kasaba and Finike Basins in the west and the Aksu, Köprü, Manavgat Basins and the Antalya Basin) bear strong resemblances to the subsidence of the Cilicia Basin and the concomitant uplift of the Mut Basin during the Pliocene-Quaternary. For example, the uplift of the once marine Kasaba Basin took place sometime between the Tortonian and Messinian, and was associated with the rise of the western Taurus Mountains, which was followed by the dramatic subsidence of the Finike Basin (and the Rhodes Basin to the west) during the Pliocene-Quaternary. Similarly, uplift of the once marine Aksu, Köprü, Manavgat Basins took place in the latest Miocene (?Messinian), again associated with the rise of the central Taurus Mountains, while subsidence continued in the Antalya Basin during the Pliocene Quaternary. These similarities in the geohistories of these regions strongly indicate that there must be similarities in the processes that partitioned these marine depocentres from their now-onland counterparts. The common process is orogenesis: while the Taurus Mountains of southern Turkey were rising, a number of basins which were located along the southern fringes of the orogen became incorporated into the mountain belt, and now several such basins rest over the Taurides (Fig. 7.15). This study suggests that the coupled subsidence in the present-day marine basins and uplift in the former Miocene marine basins may be a common process in this region of the eastern Mediterranean.

Table 7.1 Drainage areas of the small rivulets that are presently draining into the Inner Cilicia Basin (EIE, 1982, 1984).

Rivulet	Drainage area (km^2)
Efrenk	110
Alata	380
Sorgun	268.8
Lamas	1026

CHAPTER 8: CONCLUSIONS

The interpretation and mapping of ~3000 km of high-resolution seismic reflection profiles, supplemented by ~750 km of industry seismic reflection profiles and the lithological and chronostratigraphic data from two exploration wells from the Cilicia Basin revealed the following salient conclusions:

- On the basis of acoustic character and lateral continuity four seismic stratigraphic units are identified in the Cilicia Basin, i.e. Units 1-4. Unit 1 is a regularly reflective package which shows large variations in thickness from <100 m over the structural highs such as the Misis-Kyrenia horst block to >2500 m thick across the deepest portion of the Inner Cilicia Basin. Unit 1 is correlated with the Pliocene-Quaternary deltaic successions originating from the Seyhan, Ceyhan, Tarsus and Göksu Rivers. Unit 2 is characterized by an acoustically homogeneous package with chaotic and often discontinuous reflections. It is correlated with the Messinian evaporite succession. Unit 2 is found to be mobilized and moved into the footwall and hanging wall of faults in the Inner Cilicia Basin forming distinctive salt rollers. Across the boundary between the Inner and Outer Cilicia Basins, as well as along the western Cilicia margin, Unit 2 developed two prominent salt walls. Unit 3 is a package consisting mainly of reverberatory reflectors that show considerable lateral continuity. It is correlated with the predominantly siliciclastic successions of pre-Messinian Miocene age. Unit 4 is composed of pre-Miocene successions of various lithologies and ages.

- In the seismic reflection profiles there are two prominent markers, which allow a reliable seismic stratigraphy to be established. The M-reflector is a high amplitude marker reflection which shows remarkable lateral continuity. The M-reflector is a regional unconformity as indicated by the onlap and/or downlap of the overlying Unit 1 reflections or the erosional truncation of the underlying Unit 2 and/or Unit 3 reflections. It separates Unit 1 from Unit 2 where Unit 2 is present, and Unit 1 from Units 3 or 4 where Unit 2 is absent. The N-reflector is another prominent marker, which is characterized by lower amplitude and less continuous reflections. It is also an unconformity as indicated by the erosional truncation of the underlying Units 3 and/or 4 reflectors. The N-reflector separates Unit 2 from the underlying Units 3 and 4 successions. Correlations with the exploration wells show that the M-reflector is 5.3 Ma. The well data are mute regarding the age of the N-reflector, but it is estimated that it marks the base of the Messinian at ~7.2 Ma.

- The Pliocene-Quaternary succession of Unit 1 is further divided into three subunits (1a, 1b and 1c), separated from one another by two prominent and regionally continuous marker reflections: the A-reflector and the P-reflector. Seismic correlations with the exploration wells indicated that the A-reflector marks the Early Pliocene – Late Pliocene boundary at 3.6 Ma. Linear interpolations between a dated Quaternary marker and the P-reflector at multiple locations in the Pliocene-Quaternary succession revealed that the P-reflector is ~1.9 Ma.

- The Pliocene-Quaternary structural architecture of the Inner Cilicia Basin is characterized by two large basin-bounding fault zones: the Kozan Fault Zone in the northwest and the Misis-Kyrenia Fault Zone in the southeast. These basin bounding faults confine two large listric extensional fault fans located within the Inner Cilicia Basin: the northern and southern fans. Each listric extensional fault fan is composed of several northwest-southeast trending and southwest dipping northern fault panels and several northwest-southeast trending and northeast dipping southern panels. A central collapse graben is situated between the northern and southern fault panels in each fault fan. These two listric extensional fault fans are detached at their base at the M-reflector and the underlying evaporitic Unit 2.

- The Kozan Fault Zone is composed of several northeast-southwest trending and predominantly southeast dipping faults which on two-dimensional seismic reflection profiles show normal-sense dip/slip separations. This fault zone is confined to the western and northwestern portion of the Inner Cilicia Basin. Comparison of isopach maps revealed that there are temporal offsets of the locus of progressively younger delta lobes known to be sourced by the Göksu River. This observation suggested that there is a sinistral strike-slip associated with the faults of the Kozan Fault Zone, and that the displacement of the loci of the depocentres allowed for a conservative estimate of 0.6-1.0 cm/yr slip rate.

- The Miocene structural architecture of the Inner Cilicia Basin is characterized by a northeast-southwest trending and southeast verging fold-thrust belt. This

belt constitutes the trailing thrust panels of the Misis-Kyrenia Fault Zone. This zone of deformation created a partition in the ancestral Miocene basin that occupied large portions of the northeastern Mediterranean, creating the present-day quasi-isolated Cilicia Basin to the northwest and the Latakia Basin to the southeast.

- The volumetrics of sediments contained between the M- and A-reflectors, A- and P-reflectors and P-reflector and the seabed showed that the total volume of sediment arriving into the Cilicia Basin during the Pliocene and Quaternary from the Göksu River was ~ 6305 km^3. The total volume of sediments eroded from the Göksu gorge is calculated to be ~ 5789 km^3, i.e. 92% of sediments are accounted for. The sedimentation rates are calculated to be: 6.45 x 10^6 tonnes/yr for the interval bound by the M- and A-reflectors, 2.67 x 10^6 tonnes/yr for the interval bound by the A- and P-reflectors, and 8.33 x 10^5 tonnes/yr for the interval bound by the P-reflector and the seabed. These results show that sedimentation in the Early Pliocene interval was significantly greater than it is today, suggesting a more rapid period of uplift along the adjacent landmass, with uplift likely slowing in the Late-Pliocene-Quaternary as sedimentation rates fell.

- The buried topset-to-foreset transitions of the dated deltas allowed for estimates of subsidence along the western shelf-edge of the Inner Cilicia Basin. Subsidence rates in this region were found to decrease from ~0.6-0.8 mm yr^{-1} in the Early Pliocene interval to ~0.10-0.20 mm yr^{-1} in the Late Pliocene-Quaternary interval. The subsidence contrasts with the uplift of the

plateau and Taurus Mountains and it is suggested that the subsidence results from the thrust load of the adjacent and thickened Taurus Mountains. The suggestion of others that the plateau uplift is caused by the collision of seamounts with the subduction zone south of Cyprus is incompatible with the observed subsidence of the Cilicia Basin in the Pliocene and Quaternary.

- Similar scenarios were discovered in the uplift of former marine depocentres and concomitant subsidence of present-day marine basins in the Finike, Rhodes and Antalya Basins. It is suggested that this pattern of basin subsidence in response to loading of the crust supplied by the Taurus Mountains is a common process in the eastern Mediterranean.

REFERENCES

Akay, E. and Uysal, S., 1985. Orta Torosların batısındaki (Antalya) Neojen çökellerinin stratigrafisi, sedimantolojisi ve yapısal jeolojisi. Mineral Research Exploration Institute (MTA), unpublished report, 276 pp.

Akay, E., Uysal, S., Poisson, A., Cravette, J., Müller, C., 1985. Antalya Neojen havzasının stratigrafisi. Bulletin of the Geological Society of Turkey, 28: 105-119.

Aksu, A.E., Uluğ, A., Piper, D.J.W., Konuk Y.T. and Turgut, S., 1992a. Quaternary sedimentary history of the Adana, Cilicia and Iskenderun Basins, northeastern Mediterranean Sea. Marine Geology, 104: 55-71.

Aksu, A.E., Calon, T., Piper, D.J.W, Turgut, S, and Izdar, E. 1992b. Architecture of late orogenic basins in the eastern Mediterranean Sea. Tectonophysics, 210: 191-213.

Aksu, A.E., Calon, T.J., Hall, J., Mansfield, S. and Yaşar, D., 2005a. The Cilicia - Adana Basin complex, Eastern Mediterranean: Neogene evolution of an active fore-arc basin in an obliquely convergent margin. Marine Geology 221: 121-159.

Aksu, A.E., Calon, T.J., Hall, J., and Yaşar, D., 2005b. Origin and evolution of the Neogene Iskenderun Basin, northeastern Mediterranean Sea. Marine Geology 221: 161-187.

Aksu A.E., J. Hall, and Yaltırak, C., 2009. Neogene evolution of the Anaximander Mountains and Finike Basin at the Junction of Hellenic and Cyprus Arcs, Eastern Mediterranean. Marine Geology, 258: 24-47.

Allen, P.A. and Allen, J.R., 2005. Basin Analysis: Principles and Applications., Second Edition. pp. 549. Blackwell Publishing.

Anastasakis, G., Kelling, G., 1991. Tectonic connection of the Hellenic and Cyprus arcs and related geotectonic elements. Marine Geololgy, 97, 261–277.

Bassant, P., van Buchem, F.S.P., Strasser, A. and Görür, N., 2005. The stratigraphic architecture and evolution of the Burdigalian carbonate—siliciclastic sedimentary systems of the Mut Basin, Turkey. Sedimentary Geology, 173: 187–232.

Ben Avraham, Z., Tibor, G., Limanov, A.F., Leybov, M.B., Ivanov, M.K., Tokarev, M.Yu., Woodside, J.M., 1995. Structural and tectonics of the eastern Cyprus Arc. Marine and Petroleum Geology, 12: 263–271.

Biju-Duval, B., Letouzey, J., Montadert, L., 1978. Structure and evolution of the Mediterranean Basins. In: Hsü, K., Montadert, L., et al., (Eds.), Initial Reports of the Deep Sea Drilling Project, vol. 42 (1). US Government Printing Office, Washington, pp. 951–984.

Bridge, C., Calon, T.J., Hall, J. and Aksu, A.E., 2005. Salt tectonics in two convergent margin basins of the Cyprus Arc, northeastern Mediterranean. Marine Geology 221: 223-259.

Burton-Ferguson, R., Aksu, A.E., Calon, T.J., and Hall, J., 2005. Seismic stratigraphy and structural evolution of the Adana Basin, Eastern Mediterranean. Marine Geology 221: 189-222.

Calon, T.J., Hall, J. and Aksu, A.E., 2005a. The Oligocene-Recent evolution of the Mesaoria Basin (Cyprus) and its western marine extension, Eastern Mediterranean. Marine Geology 221: 95-120.

Calon, T.J., Aksu, A.E. and Hall, J., 2005b. The Neogene evolution of the Outer Latakia Basin and its extension into the Eastern Mesaoria Basin (Cyprus), Eastern Mediterranean. Marine Geology 221: 61-94.

Carver, R.E., 1971. Procedures in Sedimentary Petrology, 653 pp. John Wiley & Sons Incorporated, New York, New York.

Chorowicz, J., P. Luxey, N. Lyberis, J. Carvalho, J. F. Parrot, T. Yürür, and N. Gündoğdu (1994). The Maras triple junction (southern Turkey) based on digital elevation model and satellite imaginary interpretation, J. Geophys. Res. 99, 20,225–20,242.

Cleintaur, M.R., Knox, G.J., Ealey, P.J., 1977. The geology of Cyprus and its place in the eastern Mediterranean framework. Geol. Mijnb. 56 (1): 66– 82.

Cranshaw, J., 2010. Miocene to Recent tectonic and sedimentary evolution of the Anaximander Seamounts; eastern Mediterranean Sea. Unpublished MSc thesis, Memorial University of Newfoundland, 256 pp.

Cosentino, D., Radeff, G., Darbaş, G., Dudas, F., Gürbüz, K., and Schildgen, T., 2010, Late Miocene geohistory of the Mut and Adana Basins (southern Turkey): Insight for the uplift of the southern margin of the Central Anatolia Plateau, in Tectonic Crossroads: Evolving Orogens of Eurasia-Africa-Arabia: GSA Global Meeting, Ankara, Turkey, 2–4 October 2010: Boulder, Colorado, Geological Society of America, abstract number 12–2, p. 34–35.

Cosentino, D., Schildgen, T., Cipollari, P., Faranda, C., Gliozzi, E., Hudáčková,, N., Lucifora, S. and Strecker, M., 2012. Late Miocene surface uplift of the southern margin of the Central Anatolian Plateau, Central Taurides, Turkey. Geological Society of America Bulletin; January/February 2012; v. 124; no. 1/2; p. 133–145.

Dewey, J.F., Hempton, M.R., Kidd, W.S.F., Şaroğlu, F., Şengör, A.M.C., 1986. Shortening of continental lithosphere: the neotectonics of eastern Anatolia — a young collision zone. In: Coward, M.P., Ries, A.C. (Eds.), Collision Tectonics. Geological Society Special Publication, 19: 3–36.

Deynoux, M., Çiner, A., Monod, O., Karabıyıkoğlu, M., Manatschal, G. and Tuzcu, S., 2005. Facies architecture and depositional evolution of alluvial fan to fan-delta complexes in the tectonically active Miocene Köprüçay Basin, Isparta Angle, Turkey. Sedimentary Geology, 173: 315-343.

Dwyer, G.S. and Chandler, M.A., 2009. Mid-Pliocene sea level and continental ice volume based on coupled benthic Mg/Ca palaeotemperatures and oxygen isotopes. Philosophical Transactions of the Royal Society A, 367: 157–168, doi:10.1098/rsta.2008.0222

EIE, 1982. Elektrik İşleri Etüd İdaresi Genel Müdürlüğü (General Directorate of Electrical Power Resources Survey and Development Administration). Sediment data and sediment transport amount for surface water in Turkey. Publication 82-22, 283 pp.

EIE, 1984. Elektrik İşleri Etüd İdaresi Genel Müdürlüğü (General Directorate of Electrical Power Resources Survey and Development Administration). 1981 water year discharges. 304 pp.

Einsele, G., 1993. Sedimentary Basins: Evolution, Facies and Sediment Budget. Springer-Verlag, Berlin, New York. 628 pp.

Elboth, T., Reif, B.A.P. and Andeassen, Ø., 2009. Flow and swell noise in marine seismic data. Geophysics, 74: Q17-Q25. doi: 10.1190/1.3078403

Erentöz, C. and Ternek, Z., 1962. Geological Maps of Turkey, 1:500,000 Adana Sheet, Prepared and published by the Institute of Mineral Research and Exploration (MTA), Ankara. Printed by the Turkish Geodetical Survey.

Erickson, S. and Jarrard, R., 1998. Velocity-porosity relationships for water-saturated siliciclastic sediments. Journal of Geophysical Research, 103, No. B12: 30,385-30,406.

Eriş, K.K., Bassant, P. and Ülgen, U.B., 2005. Tectono-stratigraphic evolution of an Early Miocene incised valley-fill (Derinçay Formation) in the Mut Basin, southern Turkey. Sedimentary Geology, 173: 151–185.

Ergin, M., Aktar, M. and Eyidoğan, H., 2004. Present-Day Seismicity and Seismotectonics of the Cilician Basin: Eastern Mediterranean Region of Turkey. Bulletin of the Seismological Society of America, 94: 930–939.

Evans, G., Morgan, P., Evans, W.E., Evans, T.R. and Woodside, J.M., 1978. Faulting and halokinetics in the northeastern Mediterranean between Cyprus and Turkey. Geology, 6: 392-396.

Gadallah, M.R. and Fisher, R.L., 2005. Applied Seismology: A Comprehensive Guide To Seismic Theory And Application. PennWell Books, Tulsa, Oklahoma. 473 pp.

Gilbert, G. K., 1885. The topographic features of lake shores. U.S. Geological Survey 5th Annual Report, p. 104-108.

Gillis, G. "Diffraction". Schlumberger Oilfield Glossary. 2012. Schlumberger Oilfield Glossary Online. 5 May, 2012.

Gogacz, A., (in progress). Miocene to Recent sedimentary and structural evolution of the western Antalya Basin, Eastern Mediterranean Sea. In progress MSc thesis, Memorial University of Newfoundland.

Gökçen, S.L., Kelling, G., Gökçen, N., Floyd, P.A., 1988. Sedimentology of a late Cenozoic collisional sequence: the Misis Complex, Adana, southern Turkey. Sedimentary Geolology, 59: 205– 235.

Govers, R. and Wortel, M.J.R., 2005. Lithosphere tearing at STEP faults: Response to edges of subduction zones. Earth and Planetary Science Letters 236: 505– 523.

Hall, J., Aksu, A.E., Calon, T.J. and Yaşar, D., 2005a. Varying tectonic control on basin development at an active microplate margin: the Iskenderun - Latakia Basin complex, Eastern Mediterranean. Marine Geology, 221: 15-60.

Hall, J., Calon, T.J., Aksu, A.E., and Meade, S.R., 2005b. Structural evolution of the Latakia Ridge and Cyprus Basin at the front of the Cyprus Arc, Eastern Mediterranean Sea. Marine Geology, 221: 261-297.

Hall, J., Aksu, A.E., Yaltirak, C., and Windsor, J. D., 2009. Structural architecture of the Rhodes Basin: a deep depocentre that evolved since the Pliocene at the junction of the Hellenic and Cyprus Arcs, eastern Mediterranean. Marine Geology, 258: 1-23.

Hayward, A.B., 1984. Sedimentation and basin formation related to ophiolite nappe emplacement; Miocene, SW Turkey. Sedimentary Geology 40: 105–129.

Hsü, K.J., Cita, M.B. and Ryan, W.B.F., 1973. The origin of the Mediterranean evaporites. *In*: W.B.F. Ryan, K. Hsü et al. (Eds.), Initial Reports of the Deep Sea Drilling Project, 13(1): 1203-1231, US Government Printing Office, Washington.

Hsü, K.J. Montadert, L., Bernoulli, D., Cita, M.B., Erickson, A., Garrison, R.E., Kidd, R.B., Mélières, F., Müller, C. and Wright, R., 1978. History of the Mediterranean salinity crisis. *In*: K. Hsü, L. Montadert et al., Initial Reports of the Deep Sea Drilling Project XLII, Part I, p. 1053-1078. U.S. Government Printing Office, Washington.

İlgar, A. and Nemec, W., 2005. Early Miocene lacustrine deposits and sequence stratigraphy of the Ermenek Basin, central Taurides, Turkey. Sedimentary Geology, 173: 233-275.

Imbrie, J., Hays, J.D., Martinson, D.G., Mclntyre, A., Mix, A.C., Morley, J.J., Pisias, N.G., Prell, W.L. and Shackleton, N.J., 1984. The orbital theory of Pleistocene climate: support from a revised chronology of the marine $\delta^{18}O$ record. *In*: A. Berger, J. Imbrie, J. Hays, G. Kukla and B. Saltzman (Editors), Milankovitch and Climate. Reidel, Dordrecht, Part I, pp. 269-305.

Intergovernmental Oceanographic Commission (IOC), 1981. International Bathymetric Chart of the Mediterranean. Published by the Head Department of Navigation and Oceanography, Russia, under the authority of IOC, 10 sheets.

Işler, E.B., 2005. Late quaternary stratigraphic and tectonic evolution of the northeastern Aegean Sea, 244 pp.

Işler, F.I., 2003. Miocene to recent stratigraphy, structural architecture and tectonic evolution of the Antalya Basin, eastern Mediterranean Sea. Unpublished MSc thesis, Memorial University of Newfoundland, 243 pp.

Işler, F.I., Aksu, A.E., Hall, J., Calon, T.J. and Yaşar, D., 2005. Neogene development of the Antalya Basin, Eastern Mediterranean: an active fore-arc basin adjacent to an arc junction. Marine Geology 221: 299-330.

Jaffey, N. and Robertson, A.H.F., 2001. New sedimentological and structural data from the Ecemis Fault Zone, southern Turkey: implications for its timing and offset and

the Cenozoic tectonic escape of Anatolia. Journal of the Geological Society, 158, 367–378.

Karabıyıkoğlu, M., Çiner, A., Monod, O., Deynoux, M., Tuzcu, S. and Örçen, S., 2000. Tectonosedimentary evolution of the Miocene Manavgat Basin, western Taurides, Turkey. *In*: E. Bozkurt, J.A. Winchester, J.A.D., Piper (Eds.), Tectonics and Magmatism in Turkey and the Surrounding Area. Geological Society, London, Special Publications, 173: 475-498.

Karner, D.B., Levine, J., Medeiros, B.P., and Muller, R.A., 2002. Constructing a stacked benthic delta O-18 record. Paleoceanography, 17, 3, doi:10.1029/2001PA000667, 2002.

Kelling, G., Gökçen, S.L., Floyd, P.A., Gökçen, N., 1987. Neogene tectonics and plate convergence in the eastern Mediterranean: new data from southern Turkey. Geology, 15: 425-429.

Kempler, D., and Ben-Avraham, Z., 1987. The tectonic evolution of the Cyprean Arc. Ann. Tecton., 1, 58-71.

Kempler, D., Garfunkel, Z., 1994. Structure and kinematics in the northeastern Mediterranean: a study of an irregular plate boundary. Tectonophysics, 234: 19-32.

Kenyon, P. M. and Turcotte, D. L., 1985. Morphology of a delta prograding by bulk sediment transport. Geological Society of America Bulletin, 96: 1457-1465,

King, H. (in progress). Structural and stratigraphic evolution of the western Antalya Basin, Eastern Mediterranean Sea. In progress MSc thesis, Memorial University of Newfoundland.

Kouwenhoven, T.J. and van der Zwaan, G.J., 2006. A reconstruction of late Miocene Mediterranean circulation patterns using benthic foraminifera. Palaeogeography, Palaeoclimatology, Palaeoecology 238: 373–385.

Kozlu, H., 1987. Structural development and stratigraphy of Misis-Andirin region. In: Proceedings of the 7th Petroleum Congress of Turkey, Turkish Association of Petroleum Geologists, p. 104-116.

Kurtboğan, B., (in progress). Structural and sedimentary evolution of the central Cilicia Basin, eastern Mediterranean Sea. In progress MSc thesis, Memorial University of Newfoundland.

Lisiecki, L.E. and Raymo, M.E., 2005. A Pliocene-Pleistocene stack of 57 globally distributed benthic d18O records. Paleoceanography, 20, PA1003, doi:10.1029/2004PA001071.

McClusky, S., Balassanian, S., Barka, A., et al. 2000. Global positioning system constraints on plate kinematics and dynamics in the eastern Mediterranean and Caucasus. Journal of Geophysical Research, 105: 5695-5719.

Mitchum, M.R., Jr., Vail, P.R. and Sangree, J.B., 1977. Seismic stratigraphy and global changes of sea level, part 6: stratigraphic interpretation of seismic reflection patterns in depositional sequences. In: C.E. Payton (Editor), Seismic Stratigraphy

Applications to Hydrocarbon Exploration. Mem., American Association of Petroleum Geol., 26: 117-135.

Monod, O., Kuzucuoğlu, C. and Okay, A.İ., 2006. A Miocene paleovalley network in the western Taurus (Turkey). Turkish Journal of Earth Sciences, 15: 1-23.

Moores, E.M. and Twiss, R.J., 1995. Tectonics. W.H. Freeman and Company, New York, 415 pp.

Mulder, C.J., 1973. Tectonic framework and distribution of Miocene evaporites in the Mediterranean. In: Drooger, C.W. (Ed.), Messinian Events in the Mediterranean. Koninklijke Nederlandse Akademic von Weterschappen. North-Holland Publishing Company, Amsterdam, pp. 44–59.

Mulder, C.J., Lehner, P. and Allen D.C.K., 1975. Structural evolution of the Neogene salt basins in the eastern Mediterranean and the Red Sea. Geologie en Mijnbouw, 54: 208-221.

Ocakoğlu, F., 2002. Paleoenvironmental analysis of a Miocene basin in the high Taurus (southern Turkey) and its paleogeographical and structural significance. Geological Magazine, 139: 473-487.

Perinçek, D. Günay, Y., and Kozlu, H., 1987. New observations on strike-slip faults in east and southeast Anatolia. In: Proceedings of the 7th Petroleum Congress of Turkey, Turkish Association of Petroleum Geologists, p. 89-103.

Piercey, T., 2011. A seismic reflection study of the Neogene sedimentary history of the outer Cilicia Basin, eastern Mediterranean. Unpublished MSc thesis, Memorial University of Newfoundland, 183 pp.

Polonia, A., Gasperini, L., Amorosi, A., Bonatti, E, Bortoluzzi, G., Çağatay, N., Capotondi, L., Cormier, M.-H., Görür, N., McHugh, C., Seeber, L., 2004. Earth and Planetary Science Letters, 227: 411– 426.

Radeff, G., Cosentino, D., Schildgen, T.F., Güldemin Darbaş, G., and Gürbüz, K., 2011. Differences and similarities in the Late Miocene geohistory of the Mut and Adana basins (southern Turkey): a record of surface uplift of the southeast margin of the Central Anatolian plateau. Geophysical Research Abstracts, Vol. 13, EGU2011-1691, 2011, EGU General Assembly 2011.

Raymo, M.E., Mitrovica, J.X., O'Leary, M.J., DeConto, R.M., and Hearty, P.J., 2011. Departures from eustasy in Pliocene sealevel records. Nature Geoscience, 4: 328–332, doi:10.1038/ngeo1118.

Robertson, A.H.F., Woodcock, N.H., 1986. The role of Kyrenia Range lineament, Cyprus, in the geological evolution of the eastern Mediterranean area. Royal Society of London Philosophical Transactions Series A 317: 141–177.

Robertson, A.H.F., Eaton, S., Follows, E.J., Payne, A.S., 1995. Depositional processes and basin analysis of Messinian evaporates in Cyprus. Terra Nova 7: 233– 253.

Robertson, A.H.F., 1998. Mesozoic–Tertiary tectonic evolution of the easternmost Mediterranean area: Integration of marine and land evidence. In: Robertson,

A.H.F, Emeis, K.C., Richter, C., Camerlenghi, A. (Eds.), Proceeding of the Ocean Drilling Program, Scientific Results, 160: 723–782.

Ryan, W.B.F., 1969. The floor of the Mediterranean Sea. PhD Thesis, Columbia University, New York, 236 pp.

Ryan, W.B.F. et al., 2009. Global Multi-Resolution Topography synthesis. Geophys. Geosyst., 10, Q03010.

Şafak, Ü. Kelling, G. Gökçen, N.S., and Gürbüz, K., 2005. The mid-Cenozoic succession and evolution of the Mut basin, southern Turkey, and its regional significance. Sedimentary Geology, 173: 121–150.

Satur, N., Kelling, G., Cronin, B.T., Hurst, A., and Gürbüz, K., 2005. Sedimentary architecture of a canyon-style fairway feeding a deep-water clastic system, the Miocene Cingöz Formation, southern Turkey: significance for reservoir characterisation and modelling. Sedimentary Geology, 173: 91-119.

Şenel, M., 1997 a. Geological Map of Fethiye, L8 quadrangle, No: 2, 1:100,000 General Directorate of Mineral Research and Exploration, Ankara, Turkey, 22 pp.

Şenel, M., 1997 b. Geological Map of Fethiye, M8 quadrangle, No: 4, 1:100,000 General Directorate of Mineral Research and Exploration, Ankara, Turkey, 15 pp.

Şenel, M. and Bölükbaşı, A.S., 1997. Geological Map of Fethiye, M9 quadrangle, No: 5, 1:100,000 General Directorate of Mineral Research and Exploration, Ankara, Turkey, 11 pp.

Şengör, A.M.C., Yılmaz, Y., 1981. Tethyan evolution of Turkey: a plate tectonic approach. Tectonophysics 75: 181–241.

Şengör, A.M.C., Görür, N., Şaroğlu, F., 1985. Strike-slip faulting and related basin formation in zones of tectonic escape: Turkey as a case study. Special Publication of the Society of Economic Paleontologists and Mineralogists, 37: 227– 264.

Şengör, A.M.C., Tüysüz, O., İmren, C., Sakınç, M., Eyidoğan, H., Görür, N., Le Pichon, X., and Rangin, C., 2005, The North Anatolian fault: A new look: Annual Review of Earth and Planetary Sciences, 33: 37–112,

Schildgen, T.F., Cosentino, D., Bookhagen, B., Dudas, D., Echtler, H., Niedermann, S., Radeff, G, Strecker, M., Yıldırım, C., Hudáčková, N. and the VAMP Team, 2011. Changing rates and patterns of surface uplift at the southern margin of the Central Anatolian plateau (Turkey): New data from marine stratigraphy and cosmogenic nuclide dating of river terraces. Geophysical Research Abstracts, Vol. 13, EGU2011-4113-1, 2011, EGU General Assembly 2011.

Sclater, J. G., and P. A. F. Christie, 1980. Continental stretching: an explanation of the post-mid-Cretaceous subsidence of the central North Sea basin: Journal of Geophysical Research, 85: 3711-3739.

Sheriff, R.E. and Geldart, L.P., 1995. Exploration Seismology. Cambridge University Press, Ed. 2, 592 pp.

Smith, W.H.F. and Sandwell, D.T., 1997. Global seafloor topography from satellite altimetry and ship depth soundings, Science, 277: 1957-1962.

Tanar and Gökçen, 1990, Mut-Ermenek Tersiyer istifi nin stratigrafi si ve mikropaleontolojisi: Ankara, Turkey, Maden Tetkik ve Arama Genel Müdürlüğü (MTA): Dergisi, 110: 175–180.

Ternek, Z., 1962, (Compiler). Geological Map of Turkey, Adana Sheet, 1:500,000, Institute of Mineral Resources and Exploration (MTA), Ankara, Turkey. Printed by the Turkish Geodetical Survey.

ten Veen, J.H.,Woodside, M., Zitter, T.A.C., Dumont, J.F., Mascle, J., Volkonskaia, A., 2004. Neotectonic evolution of the Anaximander Mountains at the junction of the Hellenic and Cyprus Arcs. Tectonophysics 391: 35–65.

Uffenorde, H., Lund, J.J. and Georgi, K.H., 1990. Biostratigraphy of the Neogene in the Iskenderun Basin. Turkish Association of Petroleum Geologists, Proceedings of the 8th Petroleum Congress of Turkey, 363-370.

Umhoefer, P.J., Whitney, D.L., Teyssier, C., Fayon, A.K., Casale G., and Heizler, M.T., 2007. Yo-yo tectonics in a wrench zone, Central Anatolian fault zone, Turkey. Geological Society of America Special Papers 2007, 434: 35-57.

van Eysinga, F.W.B., 1975, Geological time table (3rd ed.). Elsevier Publishing Company, Amsterdam.

Vidal, N., Klaeschen, D., Kopf, A., Docherty, C., Von Huene, R., Krasheninnikov, V.A., 2000a. Seismic images at the convergence zone from south of Cyprus to the Syrian coast, eastern Mediterranean. Tectonophysics 329: 157–170.

Vidal, N., Alvarez-Marro´n, Klaeschen, D., 2000b. The structure of the Africa–Anatolia plate boundary in the eastern Mediterranean. Tectonics 19: 723–739.

Watts, A.B., 2001. Isostasy and Flexure of the Lithosphere. 458 pp. Cambridge, New York, Melbourne: Cambridge University Press.

Weiler, Y., 1969. The Miocene Kythrea flysch basin in Cyprus. G. Geol. 35, 213– 229.

Williams, G.D., Ünlügenç, U.C., Kelling, G. and Demirkol, C., 1995. Tectonic controls on stratigraphic evolution of the Adana Basin, Turkey. Journal of Geological Society of London, 152: 873-882.

Woodside, J.M., Mascle, J., Zitter, T.A.C., Limonov, A.F., Ergün, M. The Florence Rise, the Western Bend of the Cyprus Arc, Marine Geology, 185, Issues 3–4: 177-194.

Yalçın, N.M. and Görür, N., 1984. Sedimentological evolution of the Adana Basin. *In*: Tekeli, O. and Göncüoğlu, M.C. (Eds.), Proceedings of the International Symposium on the Geology of the Taurus Belt, Ankara, 165-172.

Yetiş, C., Kelling, G., Gökçen, S.I., Baroz, F., 1995. A revised stratigraphic framework for Late Cenozoic sequences in the northeastern Mediterranean region. Geol. Rundsch. 84: 794–812.

Yılmaz, Y., Gürpınar, O., Yiğitbaş, E., 1988. Tectonic evolution of the Miocene basins at the Amanos Mountains and the Maraş region. Bulletin of the Turkish Association of Petroleum Geologists 1/1, 52– 72.

Yılmaz, Y., 1993. New evidence and model on the evolution of the southeast Anatolian orogen. Geological Society of America Bulletin, 105: 251– 271.

Yılmaz, O., 2000. Seismic Data Analysis: Processing, Inversion and Interpretation of Seismic Data, Rev. Ed. Society of Exploration Geophysicists, pp. 2027.